An investigation of equine hoof shapes using physical descriptors from μ-computed tomography

Sophie Taylor, BVMed Sci.

Thesis submitted to the university of Nottingham for the degree of Master of Research

July 2017

Abstract

Reasons for performing the study:

As the most common cause of equine euthanasia, equine foot lameness is highly prevalent thus having high economic and welfare impacts. Those of particular concern are foot pathologies associated with the lamellae, more commonly known as ‘laminitis’. To investigate the full extent of the equine foot in order to gain a sufficient understanding of its anatomical structures in a normal state and the pathological adaptations associated with laminitis, a novel technique was employed with the utilization of micro-computed tomography.

Aims and objectives:

The aim of this study was to investigate the anatomical components of the equine foot with the use of a laboratory µ-CT scanner. The fundamental objective underpinning this study was to mathematically model the different physical descriptors of the equine foot and their morphological state.

Methods:

44 cadaveric equine feet µ-CT image stacks were used to assess their anatomical components with the use of Fiji ImageJ software. 44 equine feet were used to calculate the dorsal hoof wall curvature and dorsal hoof wall thickness at the quarters and 43 at the toe region. The third phalanx (P3) was analysed by calculating its dorsal curvature (n=43), cortical bone thickness (n=44) and trabecular bone anisotropy (n=44). Analysis of the vasculature network was calculated in 28 equine feet, recording the total branch lengths, mean lumen diameter and the percentage of stretched to bundled vessels. In addition, the corium volume was calculated for a total of 44 equine feet. The data was mapped as a function of dorsal hoof wall curvature, bone curvature and categorised using both variables. The percentage of stretched to

bundled vessels and vasculature volume was also plotted as a function of corium volume.

Results:

Hoof capsule and P3 curvature measurements differed between feet, calculated using a modified version of the differential calculus equation. From these measurements four different morphological categories were established for comparison against other physical descriptors. Dorsal hoof wall thickness was measured and found to be thicker at the quarters than at the toe region irrespective of dorsal hoof curvature. Changes in P3 curvature, trabecular bone anisotropy at the toe tip and cortical bone thickness occurred more frequently in feet with a convex dorsal hoof wall. No significant changes to the blood vessels were identified. However vasculature volume and corium volume increased almost linearly with respect to one another ($P<0.001$). A greater percentage of bundled vessels were shown in feet with a convex dorsal hoof wall and dorsal P3 surface.

Conclusions:

This study demonstrates how the novel application of μ-CT scanning can be used to investigate the anatomical components of the equine foot. Furthermore measurements and data can be extracted from these images enabling the physical descriptors to be mathematically modelled for analysis.

Potential relevance:

Despite extensive research, the pathogenesis and pathomorphology of laminitis has not been explained. With the application of μ-CT the identification of anatomical adaptations in equine feet with foot pathologies could assist in this understanding.

Abbreviations

X	Absorber thickness
Z	Atomic number
BM	Basement Membrane
BMP	Bone morphogenic proteins
CaR	Calcium sensing receptors
CV	Coefficient of variation
CL	Collateral ligament
CDEM	Common digital extensor muscle
CDET	Common digital extensor tendon
CT	Computed tomography
DDFM	Deep digital flexor muscle
DDFT	Deep digital flexor tendon
DA	Degree of anisotropy
DIP	Digital interphalangeal joint
EGF	Epidermal growth factor
FGF	Fibroblast growth factor
P1	First phalanx
GM-CSF	Granulocyte macrophage colony stimulating factor
IGF	Insulin like growth factors
LEM	Lateral extensor muscle
LET	Lateral extensor tendon
μ	Linear attenuation coefficient
MIL	Mean intercept lengths
M-CT/μ-CT	Micro-computed tomography
PFA	Paraformaldehyde
PTH	Parathyroid hormone
PBS	Phosphate buffer solution
E	Photon energy
I	Photon intensity
PDGF	Platelet derived growth factor
PIP	Proximal interphalangeal joint

ROI	Region of interest
SF	Scaling factor
P2	Second phalanx
SDFM	Superficial digital flexor muscle
SDFT	Superficial digital flexor tendon
P3	Third phalanx
TGF	Transforming growth factor
TNF	Tumour necrosis factor
VEGF	Vascular endothelial growth factor
VDR	Vitamin D receptors

Contents

An investigation of equine hoof shapes using physical descriptors from µ-computed tomography i

Abstract i

Abbreviations iii

Contents v

1 Literature Review 1

1.1 Gross Anatomy of the Equine Foot 1

1.2. Bones of the Equine Foot 8

1.2.1 Bone Physiology 8

1.2.2 Anatomy of the Third Phalanx 14

1.3 Vasculature of the Equine Foot 15

1.3.1 Vascular Physiology 15

1.3.2 Vascular Anatomy of the Equine Foot 16

1.4 Lamellae, Papillae and Equine Hoof Growth 18

1.6 Lameness & Laminitis 20

1.7 X-ray µ-Computed Tomography 23

1.8 Aims and Objectives 25

2 Materials and Method 26

2.1 Foot collection and preparation 26

2.1.1 Abattoir collection and preparation 26

2.2 CT scanning 27

2.2.1 Laboratory Micro-Tomography 27

2.3 CT image processing 28

2.3.1 Hoof Orientation and Planar Adjustments 28

2.3.2 Bone Segregation 28

2.4 Physical descriptors 29

2.4.1 Dorsal curvature 29

2.4.2 Dorsal wall thickness 31

2.5 Bone Analysis 33

2.5.1 Bone curvature 33

2.5.2 Cortical bone thickness 33
2.5.3 Bone Anisotropy 34
2.6 Vasculature Analysis 37
2.6.1 Mean lumen diameter 37
2.6.2 Total branch length 38
2.6.2.1 Stretched and bundled vasculature 38
2.6.3 Volume of corium 40
2.7 Anatomical Image Rendering 42
3 Results 43
3.2 Physical Descriptors 43
3.2.1 Categorising Data 43
3.2.2 Dorsal wall curvature and thickness 45
3.2.3 Corium Volume 46
3.3 Bone 47
3.3.1 Bone Rendered μ-CT Images 47
3.3.2 Bone Curvature 52
3.3.3 Cortical Bone Thickness 53
3.3.4 Trabecular Bone Anisotropy 63
3.4 Vasculature 64
3.4.1 Vasculature rendered μ-CT scan images 64
3.4.2 Vasculature Branches 65
3.4.3 Lumen Diameter 69
3.4.4 Software Development For Vasculature Isolation 71
4 Discussion 72
4.2 Pathomorphological Features 72
4.2.1 External Features 72
4.2.2 Internal Features 73
4.3 Bone Remodelling 74
4.4 Vascular remodelling 79
4.5 Methodology 82
4.6 Future Research 84
4.6.1 Laboratory μ-CT 84
4.6.1.2 Microvasculature Analysis 85
4.6.1.2 Dynamic Imaging in Living Tissue 85
4.6.2 Conformation and Weight Bearing 86

5 Conclusions 87

References 90

1 Literature Review

In order to investigate equine hoof growth, papillae and lamellae in association with foot lameness, it is necessary to first understand the known anatomy, histology and vasculature of the normal hoof. In this introduction a literary dissection of the hoof and the techniques required for this investigation will be examined.

1.1 Gross Anatomy of the Equine Foot

Horses belong to the group perissodactyls or odd-toed ungulates due to their anatomical adaptation to stand on the tips of the third phalanx. In order to protect this single digit the hoof is composed of a strong outer capsule (Steiner and Ryder, 2011). This hoof capsule consists of three layers: the epidermis, dermis and subcutis. The skin modification of these is similar to a fingernail, the proliferation and growth is continuous and therefore requires trimming (Budras *et al.*, 2009). The epidermis is highly keratinised forming the strong viscoelastic structural element to provide the main load support system in the equine hoof (Pollitt, 2004a; O'Grady, 2013). The hoof wall is a visible part of the hoof capsule and is composed of three different layers: the *stratum externum* (periople), *stratum medium* (the coronary horn) and the *stratum internum* (epidermal lamellae) all of which contribute to the epidermis (Pollitt, 2004a). The *stratum externum* is a thin layer starting from the coronet band finishing at the ground. The *stratum medium* contains the pigmented and un-pigmented hoof wall, providing a strong and thick protective barrier. The *stratum internum* is the innermost layer of the hoof wall and bars, it surrounds the distal phalanx (P3) and contains the laminae and vasculature supply (Kraus, 2014). The epidermis folds inwards at the rear quarters forming the bars which are an additional support to the heel bulbs at the palmar/plantar surface (Floyd and Mansmann, 2007). These structures are shown in Figure 1.1.

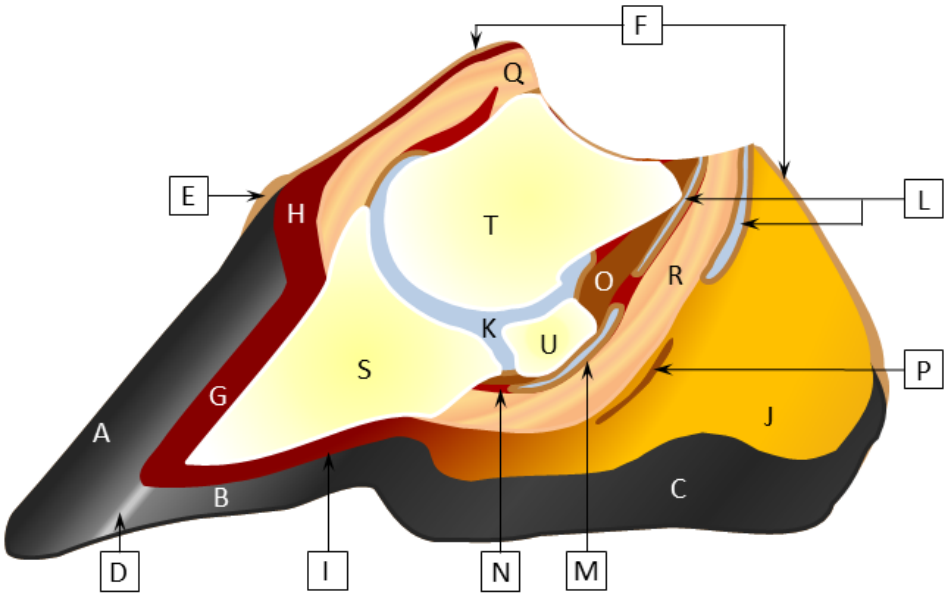


Figure 1.1: Anatomy of the equine foot. The diagram displays a mid-sagittal view of the equine foot, showing both the external and internal anatomical structures. The letters indicate the following anatomical features:

A. Hoof wall
B. Sole
C. Frog
D. White line
E. Periople
F. Skin
G. Lamellar Corium
H. Coronary Corium
I. Solar Corium
J. Digital Cushion
K. Distal Interphalangeal Joint
L. Distal Synovial Sheaths
M. Navicular Synovial Bursa
N. Distal Navicular Ligament
O. Navicular Suspensory Ligament
P. Distal Digital Annular Ligament
Q. Common Digital Extensor Tendon
R. Deep Digital Flexor Tendon
S. Third Phalanx
T. Second Phalanx
U. Navicular Bone

(Diagram courtesy of Emily Katy Paul)

The skin and hoof capsule join at the coronet band, which is covered in a visible waxy substance called the periople. The periople is secreted from cells that lie just above the coronet band, this is known as the

perioplic ring. The periople extends beyond the coronet band to provide a protective waterproof layer to aid and maintain the moisture content and prevent moisture loss reducing the possibility of cracking (Landers, 2006). On the underside of the hoof capsule is a concave crescent shaped layer of horn also known as the sole. The sole is present between the hoof wall and the frog/bars (Budras *et al.*, 2009). The sole in combination with the frog and the digital cushion acts as a load support system and aids the distribution of pressure. The frog is keratinised tissue that is highly elasticated and poorly vascularised, it forms a triangular wedge shaped mass on the underside of the hoof providing shock absorption, slip prevention and helps with blood circulation in the appendages (McClure, 1993) (Figures 1.1-1.3). The presence of the distal digital annular ligament, segregates the digital cushion from the deep digital flexor tendon (DDFT) (Spurgeon, Kainer and McCracken, 2013; Stashak, 2013).

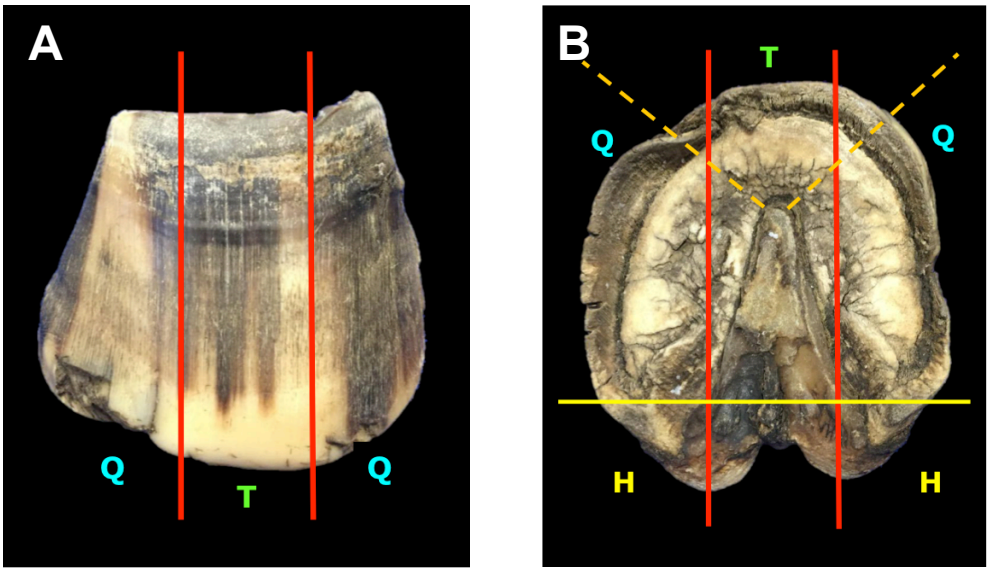


Figure 1.2: Anatomy of the hoof capsule. Images of the hoof capsule showing both the dorsal surface (A) and the sole (B). The images are annotated showing the different regions of the equine hoof. **(Q)** Quarters **(T)** Toe **(H)** Heel. Image copyright to the author.

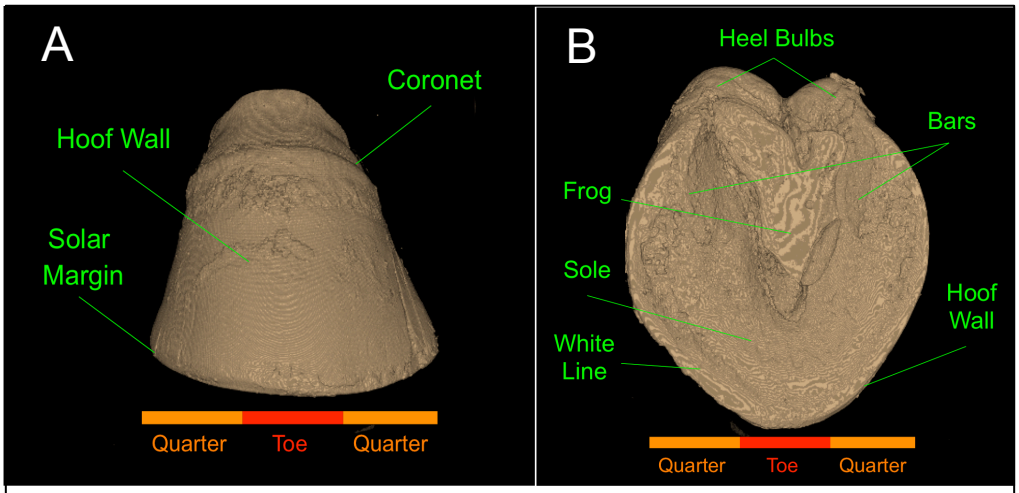


Figure 1.3: CT 3D reconstruction of the equine hoof. (A) Dorsal surface **(B)** Sole (Source information from Floyd & Mansmann 2007). Images copyright to the author.

Within the hoof capsule are the bones of the equine foot; this includes the second phalanx (P2) the third phalanx (P3) and the navicular bone (Parks, 2003; Stashak, 2013) (Figures 1.1 and 1.4). The third phalanx, also know as the pedal bone or coffin bone, is a fundamental bone within the equine foot. P3 occupies the most distal portion of the foot, unlike other long bones P3 has 3 surfaces: the articular, parietal and solar surface. The articular surface of P3 articulates with P2; palmarly there is a flattened surface where P3 also articulates with the navicular bone (Parks, 2003). The foraminous parietal surface of P3 is in contact with the dorsal surface of the hoof capsule. Multiple foramina enable blood vessels to pass through and for the surrounding subcutaneous tissue to attach. The solar surface is not foraminous except at the palmar wings of P3 (Parks, 2003; Morris, 2015). P2, or short pastern, has 2 articular surfaces that form the proximal interphalangeal joint (pastern joint (PIP)) with P1 and the distal interphalangeal joint (coffin joint (DIP)) with P3. It is approximately half the length of P1 and almost cuboidal in shape, making it resilient to a number of mechanical stresses (Floyd and Mansmann, 2007). The navicular bone, also known as the distal sesamoid bone, is small and shaped like a boat. It is located on the palmar surface of the DIP between P2 and P3. The palmar flexor surface is covered by fibrocartilage to allow the DDFT to

glide over its surface smoothly, similar to a pulley system. The articular surfaces are covered with hyaline cartilage to provide lubrication during flexion and extension of the limb (Bentley *et al.*, 2007; Waguespack and Hanson, 2010; Komosa, 2013). Three ligaments support and stabilise the navicular bone. The distal sesamoidean impar ligament originates from the distal border of the navicular bone and inserts deep on the flexor surface of P3. The collateral sesamoidean ligaments originate from both sides of the distal surface of P1 and extend palmar dorsally to the proximal margin of the navicular bone (Waguespack and Hanson, 2010).

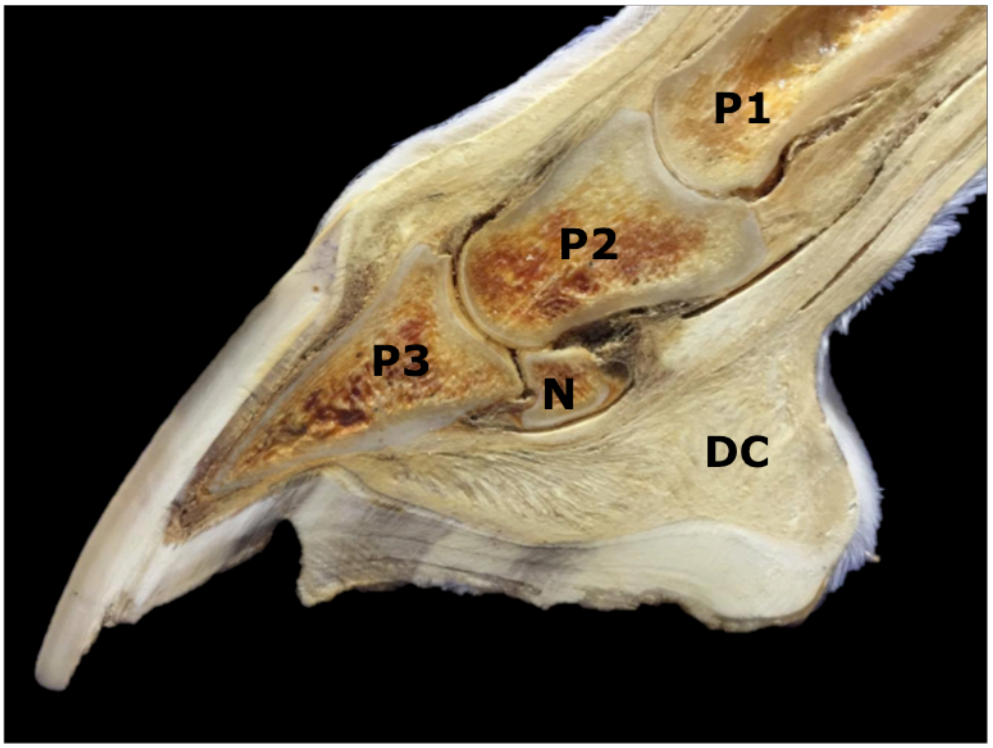


Figure 1.4: A mid-sagittal section of the equine foot. A photograph of a preserved equine hoof, showing the anatomical features and skeletal components. **(P1)** Proximal Phalanx **(P2)** Middle Phalanx **(P3)** Distal Phalanx **(N)** Navicular Bone **(DC)** Digital Cushion. Image copyright to the author.

The musculature of the equine limb is located proximally, reducing the weight distally in order to achieve efficient high-speed locomotion (Hinchcliff, Kaneps and Geor, 2008). Located in the distal portions are tendons and ligaments, allowing flexion and extension of the lower limb.

Flexion of the interphalangeal joints is due to the superficial and deep digital flexor tendons (SDFT and DDFT), which are situated caudally. Originating from the deep digital flexor muscle (DDFM) is the DDFT. The DDFT passes distally and inserts on the flexor surface of P3, allowing flexion of the DIP (Budras *et al.*, 2009; Schramme, 2011). Alongside the DDFT is the SDFT, which originates from the superficial digital flexor muscle (SDFM) and allows flexion of the interphalangeal joints. Passing distally the SDFT sits more caudal than the DDFT, inserting on the proximal surfaces of P1 and P2 (Budras *et al.*, 2009; Colville and Bassert, 2009). The extension of the interphalangeal joints arises from the common digital extensor tendon (CDET), which originates from the common digital extensor muscle (CDEM). The CDET lies laterally, passing through the lateral groove of the distal radius extending distally over the metacarpus, inserting on the extensor process of P3 along with a broad tendon (König, Liebich and Bragulla, 2007). The lateral extensor tendon (LET) is also responsible for the extension of the equine forelimb, originating from the lateral extensor muscle (LEM), descending laterally to the CDET and inserting on P1 (Dyce, Sack and Wensing, 2010).

Abduction and adduction of the equine interphalangeal joints is limited with respect to the lateral and medial collateral ligaments (CLs), providing the equine foot with support and stability (Denoix, 1999; Lawson *et al.*, 2006). The CLs of the PIP originate on the latero-distal edges of P1 and insert on the latero-proximal edges of P2. Likewise the CLs of the DIP originate on the latero-distal edges of P2 and insert on the latero-proximal edges of P3 (König, Liebich and Bragulla, 2007). While the collateral ligaments support the interphalangeal joints, the chondral ligaments and collateral cartilages support and stabilise P3. As well as providing support and stabilisation, the collateral cartilages are thought to reduce concussion and support blood flow to the structures within the hoof (Dyson and Nagy, 2011). The supporting cartilages are described as having a “C” or “L” configuration and are attached to the surrounding tissues such as the digital cushion, the

navicular bone and the phalanges by the chondral ligaments. These include the chondroungular, chondrocoronal, chondrocompedal and chondrosesamoidean ligaments (Bowker, 2003; Dyson and Nagy, 2011).

Underlying the hoof wall is the highly vascularised and innervated coria or dermis. The corium consists of a network of sensory and vasomotor nerves, arteries, veins and capillaries in a dense matrix of strong connective tissue (Pollitt, 1998, 2004a). The strong connective tissue attaches the basement membrane (BM) of the derma-epidermal junction to the surface of P3, suspending P3 within the hoof capsule. The rich vasculature of the corium provides the surrounding tissues with nourishment for growth and proliferation (Pollitt, 2010). The surface of the corium is covered with dermal papillae in the perioplic, coronary, solar and cuneate integument regions. The dermal papillae interdigitates with the epidermal tissue where each papilla interlocks with the opposing socket (Parks, 2003). The inner hoof wall and bar integument lamellae of the lamellar corium, also known as the dermal lamellae, interlocks with the surrounding epidermis. Distal to the lamellae are the terminal papillae, forming the elastic white line on the solar surface (Pollitt, 1998, 2004a).

The stratum internum (epidermal lamellae) forms 550 to 600 parallel macroscopic projections from its surface, interlocking with the surrounding dermal tissue (Pollitt, 1999, 2004a). This provides a large surface area between the epidermis and dermis for the suspension and support of P3 (Pollitt, 1999, 2004a). Each primary lamellae has microscopic projections on its surface bearing 100-200 secondary lamellae, providing a stronger interlocking system to withstand the relatively high mechanical stress (Kochová *et al.*, 2013). Between the dermis and epidermis lies the BM, a thin continuous uninterrupted sheet of extracellular matrix. The BM forms an important structural scaffold for the proliferation, orientation and maturation of epidermal

cells that form the hoof wall (Pollitt, 1994). Basal cells line the epidermal surface of the BM, providing a strong attachment to the surrounding epidermal tissue (epidermal lamellae). On the dermal surface a collagen rich, tendonous like connective tissue, projects from the dorsal surface of P3 and weaves tightly with the BM lattice (Pollitt, 2004a).

1.2. Bones of the Equine Foot

1.2.1 Bone Physiology

As foundations of the skeleton, bones are fundamentally important in vertebrate species, providing structural support, protection of vital organs, locomotive functions and act as a mineral reservoir (Walsh, 2015). Bone is a complex and dynamic tissue that has the ability to grow, maintain and repair itself by a process of modelling and remodelling. The process of remodelling is equally complex and is regulated by exogenous and endogenous factors (Clarke, 2008; Bayliss, Mahoney and Monk, 2012). The remodelling of bone is of principal importance to this study, in particular its response to mechanical strain. Understanding the effects of mechanical strain in the equine foot and the osteogenic changes in response to this could provide post-mortem clarification of the physical imbalances and their location. This will provide support for the principals of this study that interlink laminitis, hoof growth and mechanical forces. However it may also challenge some of the current concepts in the pathophysiology of laminitis, in particular the implication of the lamellae being the causative factor.

The multicellular bone has four layers to its structure, the periosteum, porous mineralised osseous tissue, endosteum and bone marrow (Liao *et al.*, 2011). Lamellar bone is the parallel alignment of collagen fibres within osseous tissue, cortical and cancellous bone are examples of this. The outermost hard layer is known as cortical bone, it is dense, solid and surrounds the marrow cavity (Bayliss, Mahoney and Monk,

2012). Cancellous bone is a porous structure, predominantly found at the end of long bones and is a more active site for bone remodelling, responding to metabolic demands quickly due to its large surface area (Hadjidakis and Androulakis, 2006; Bayliss, Mahoney and Monk, 2012). The lamellar bone on a nanoscale is composed of mineral and organic components; 60% hydroxyapatite, 30% collagen proteins and 10% water (Liao *et al.*, 2011). The organic matrix is predominantly type 1 collagen (~95%), giving bone its tensile strength (Bayliss, Mahoney and Monk, 2012; Rosenburg, Rosenburg and Soudry, 2012; Nyary and Scammell, 2015). Proteoglycans and non-collagenous proteins make up the remainder of the parallel collagenous network. The mineral matrix is composed of hydroxyapatite crystals [$Ca_{10}(PO_4)_6(OH)_2$], a calcium and phosphate ion compound and other mineral ions such as sodium and potassium. Under compressive forces the mineral matrix provides the bone with strength and resilience (Bayliss, Mahoney and Monk, 2012; Walsh, 2015).

On a microscale the complex architecture of cortical bone consists of repeated units known as osteons (Figure 1.5). Each osteon is cylindrical in shape with a central channel known as the Haversian canal. Surrounding the Haversian canal are concentric rings known as lamellae giving a condense, strong and complex structure (Zuo *et al.*, 2012). A neurovascular bundle inhabits the Haversian canal to provide a blood and nervous supply. A number of other cavities are present in the osteon in the form of canaliculi and lacunae, inhabited by cells for repair and maintenance (Clarke, 2008). In lamellar bone the collagen fibres are in parallel alignment giving strength to the architecture, woven bone on the other hand is remodelled bone where the collagen fibres have been laid down haphazardly. Woven bone usually occurs as a result of a fracture or crack in the bone tissue and is mechanically weaker (Bayliss, Mahoney and Monk, 2012; Walsh, 2015).

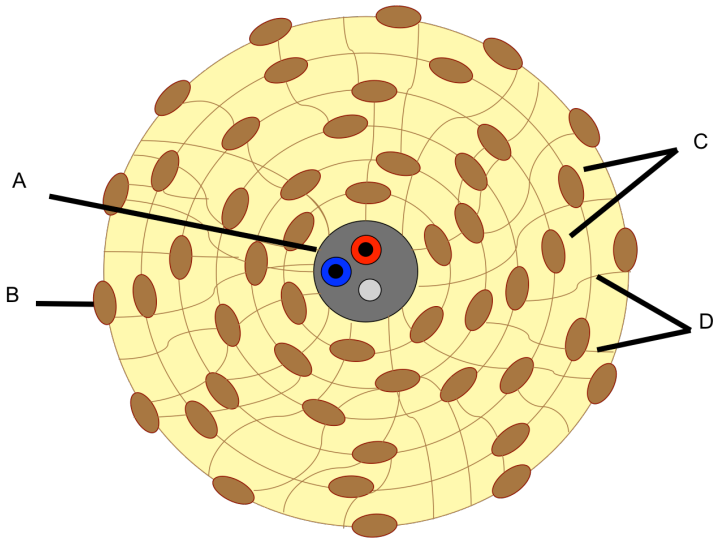


Figure 1.5: A diagram of a cortical osteon. (A) Haversian canal containing the neurovascular bundle **(B)** A lacuna containing an osteocyte **(C)** Lamellae **(D)** Canaliculi. (Source information from Ascenzi et al. 2008). Image copyright to the author.

In the human skeleton 80% of osseous tissue is cortical bone and the remaining 20% is trabecular bone (Figure 1.6). Centred in the bone marrow cavity, trabecular bone forms a honeycomb like structure, composed of plates and rods. Like compact bone trabecular bone is composed of osteons called packets that are semi-lunar in shape. Locomotion of the skeleton is aided by trabecular bone due to is low density and the reduction in its mass (Hadjidakis and Androulakis, 2006; Clarke, 2008).

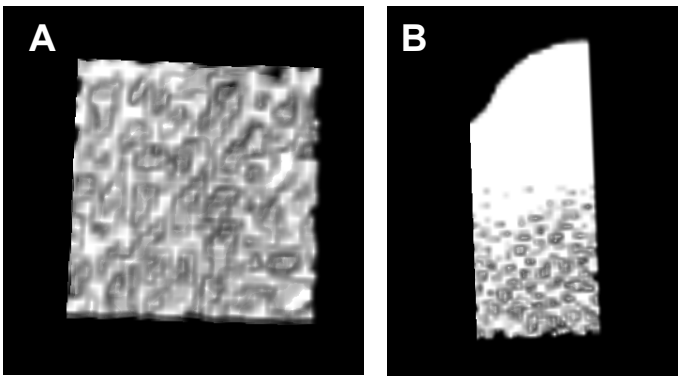


Figure 1.6: A µ-CT 3D reconstruction of bone. (A) A section of trabecular bone (B) A cross section of bone showing radiopaque cortical tissue and a region of both radiopaque and radiolucent trabecular bone. Images copyright to the author.

The renewal and remodelling of bone tissue is mediated by three different cell types; osteoblasts, osteocytes and osteoclasts (Bonewald, 2007; Nakahama, 2010). Osteoblasts are bone forming, mononuclear, polarised cells derived from mesenchymal progenitors. Their fundamental function is synthesis and mineralisation of osteoid producing the collagenous organic matrix (Bayliss, Mahoney and Monk, 2012; Rosenburg, Rosenburg and Soudry, 2012). Osteoblasts reside primarily in the endosteum – the vascularised cellular lining of the internal bone, separating the bone matrix from the marrow. They are also situated in the cambium layer of the periosteum alongside fibroblasts, adult mesenchymal progenitors, differentiated osteogenic progenitor cells, micro-vessels and nerves. Quiescent osteoblasts are mature and form a cell lining on bone surfaces, the immature osteoblasts are cuboidal and active, forming a single layer on the surface of newly formed osteoid (Allen, Hock and Burr, 2004; Walsh, 2015). Osteocytes are derived from osteoblast progenitors cells and reside in the lacunae. The osteoblasts become entrapped in the bone matrix they produced and differentiate into osteocytes (Bonewald, 2007; Bayliss, Mahoney and Monk, 2012). Osteocytes have multiple cytoplasmic processes that extend into the surrounding canaliculi aiding the metabolism and support of bone via syncytial networks. The fundamental role of the osteocyte-osteoblast cellular lining is mechanosensation, communicating via gap junctions at the distal ends of the cytoplasmic processes, as well as providing a key role in bone synthesis and resorption (Clarke, 2008). Osteoclasts are giant multinucleated cells of mononuclear-macrophage lineage, responsible for the resorption of bone (Nakamura *et al.*, 2012; Walsh, 2015). They are derived from the mononuclear phagocytes situated in the hematopoietic marrow. Once activated the osteoclasts adhere to the bone surface releasing proteolytic enzymes and reducing the pH for osteoid resorption (Pearson and Lieberman, 2004).

Bone remodelling is thought to occur as a result of changes in environmental mechanical forces, commonly referred to as Wolff's law

(Chen *et al.*, 2010). Osteocytes are strain-sensitive cells, functioning as mechanosensors, stimulating the resorption or formation of osteoid tissue by stimulating osteoclasts or osteoblasts lining the trabeculae (Tsubota and Adachi, 2005; Mercuri *et al.*, 2016). Consequently bone mechanobiology plays a role in cortical bone thickening/thinning and trabecular bone distortion thus enabling the bone to meet the environmental mechanical demands (Tsubota and Adachi, 2005; Chen *et al.*, 2010).

Besides bone growth, remodelling and maintenance, pH balance and mineral homeostasis is also maintained by the synthesis/resorption cycle (Bayliss, Mahoney and Monk, 2012). Under normal physiological conditions the lungs and kidneys maintain the narrow pH margin of blood and extracellular fluid, by the removal and excretion of H+ ions. A pH disturbance from adverse physiological conditions can lead to acidosis (Arnett, 2003). In systemic acidosis, hydroxyapatite crystals can provide the body with an emergency base reservoir via osteoclastic resorption. Osteoclasts are unusual in the way that they are stimulated by low pH conditions and as a result begin to resorb osteoid tissue, producing basic ions, “mopping” up any excess H+ ions. Concurrently osteoblastic activity is inhibited (Green and Kleeman, 1991; Arnett, 2003, 2010). Bone similarly acts as a mineral reservoir for phosphorus and calcium, enabling mineral homeostasis (Lieben and Caemeliet, 2013). Calcium and phosphorous are both fundamental physiological minerals and have a plethora of biological roles. The regulation of these minerals is controlled endocrinologically via the thyroid gland, parathyroid glands and the kidneys (Peacock, 2010). The primary hormones involved are calcitonin, calcitriol (1,25-dihydroxyvitamin D, a derivative of vitamin D), fibroblast growth factor-23 (FGF-23) and parathyroid hormone (PTH), which respectively regulate the mechanisms responsible for intestinal absorption, renal absorption and the resorption/synthesis of osteoid (Kurbel *et al.*, 2003; Atkins and Findlay, 2012; Lieben and Caemeliet, 2013). A decrease in circulating calcium concentration inactivates the calcium sensing receptors (CaR)

in the parathyroid gland, resulting in PTH secretion. PTH acts on the kidneys and increases the tubular reabsorption of calcium and an increase in net resorption of bone. PTH also stimulates the secretion of calcitriol. Calcitriol activates the vitamin D receptors (VDR) in the intestines, increasing calcium reabsorption. Concurrently PTH secretion decreases and the resorption of bone increases. In phosphorous homeostasis an increase in serum PTH acts on the kidneys to decrease renal absorption of phosphorous and as a result reduces serum phosphorous concentrations. FGF-23 also plays a part in phosphorous homeostasis, when serum concentrations of phosphorous increase there is an increase in the secretion of FGF-23 from osteocytes. FGF-23 acts on the kidneys to reduce phosphorous reabsorption, simultaneously there is a decrease in the renal secretion of calcitriol, resulting in reduced intestinal phosphate absorption (Kurbel *et al.*, 2003; Peacock, 2010).

Similarly to the secretion of FGF-23, bone acts as a reservoir for other growth factors and cytokines that assist in the regulation of bone remodelling (Canalis, McCarthy and Centrella, 1991). The cytokines and growth factors secreted play an important role in the formation and resorption of osteoid as well as effecting other cell tissue types systemically or locally, such as vasculature endothelial cells (Korf-Klingebiel *et al.*, 2008). Growth factors promoting osteogenesis include insulin-like growth factors (IGFs), bone morphogenic proteins (BMPs) and transforming growth factors (TGFs). Tumour necrosis factor (TNF), epidermal growth factor (EGF), macrophage-colony stimulating factor and granulocyte macrophage-colony stimulating factor (GM-CSF) are growth factors that trigger osteolytic resorption. Platelet derived growth factor (PDGF) and fibroblastic growth factors FGFs have the ability to promote the synthesis or resorption of bone. Similarly cytokines belonging to the interleukin family can directly or indirectly promote bone synthesis/resorption. Other cytokines such as prostaglandins and

leukotrienes stimulate the resorption of bone (Canalis, McCarthy and Centrella, 1991; Hadjidakis and Androulakis, 2006).

Bone is a dynamic and living tissue therefore it requires a substantial blood supply to provide oxygen, nutrients and to remove carbon dioxide, metabolic wastes and acid (Marenzana and Arnett, 2013). The abundant nerve and vasculature presence in the periosteum penetrates the nutrient foramina to provide a neurovascular bundle to the canals of each Haversian system. The longitudinal Haversian canals have ascending and descending capillaries that extend to the medullary cavity via the transverse Volkmann's canals. Blood supply and bone are mutually reliant to one another, as the cells of osteoid tissue require oxygen and nutrients, the bone marrow is required for haematopoiesis (Kim et al. 2015).

1.2.2 Anatomy of the Third Phalanx

The third phalanx (P3) is of particular importance to this study due to its fundamental role in the equine foot. P3 is the most distal bone in the equine limb and has numerous anatomical and distinct regions that are attached to various tissue types (Figure 1.7).

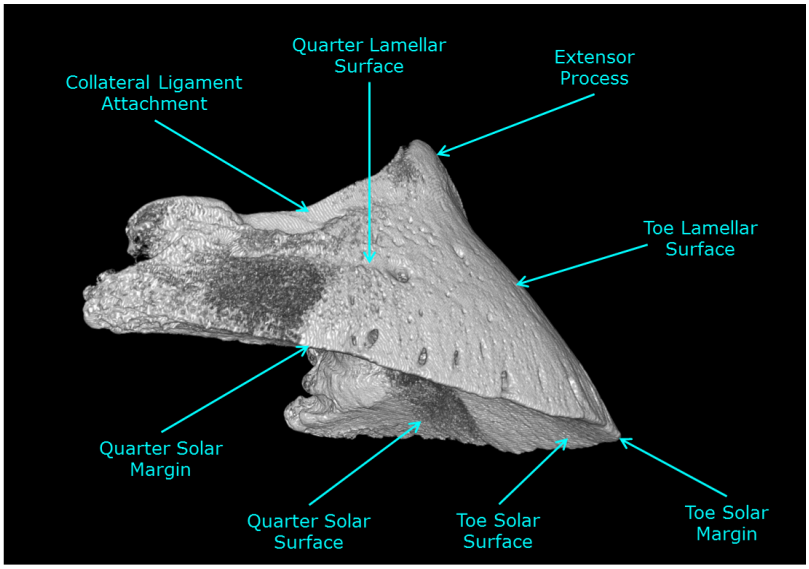


Figure 1.7: µ-CT 3D reconstruction of the distal phalanx. A reconstruction of the third phalanx showing the parietal surface, solar surface, solar margin, extensor process and collateral ligament attachment site (Source information from Floyd & Mansmann 2007). Image copyright to the author.

P3 has three main surfaces; the parietal, articular and solar surface, each of which have additional anatomical landmarks and attachment sites. The articular surface is a smooth facet located on the palmar/plantar surface, articulating with P2 and the navicular bone (Parks, 2003). Located dorsally to the articular surface is the extensor process and ventrally bordering the solar margin is the flexor surface, where the CDET and DDFT attach respectively. Collateral ligaments aid the suspension of P3 in the hoof capsule and attach on both the lateral and medial notches on the proximal edge (Floyd and Mansmann, 2007). The parietal (lamellar) surface of P3 lies underneath the hoof wall where it is attached via the dermal and epidermal lamellae (lamellar corium). The solar corium attaches in a similar manner to the solar surface of P3 providing a solar attachment for suspension and stability (Pollitt, 2004a). The solar margin is a narrow ridge border, encapsulated between the lamellar and solar corium, providing anchorage for the terminal papillae (Floyd and Mansmann, 2007).

1.3 Vasculature of the Equine Foot

1.3.1 Vascular Physiology

The development and adaptability of vasculature enables the transportation of dissolved gases, nutrients, signalling molecules such as hormones, immune cells and waste, to and from the numerous organs and tissues, making it the fundamental physiological transport system in the body (Stapor *et al.*, 2014). The closely intertwined relationship between blood vessels and other anatomical systems makes their coexistence synergistic. An example of the synergistic relationship is the growth and development of bone, enabled by the vascularisation and innervation of osteoid tissue and the process of haematopoiesis in the bone marrow (Kim et al. 2015). Another example is the ability for bone to act as a reservoir for growth factors, such as vascular endothelial growth factor (VEGF) which is the major cytokine for angiogenesis (Marenzana and Arnett, 2013). High metabolic

tissues require an increased demand for oxygen, such as the dynamic tissues of the equine hoof (Floyd and Mansmann, 2007; Stocum, 2012). Vasculature abnormalities such as extreme vasodilation and vasoconstriction, arteriovenous anastomoses, coagulatory disorders, mechanical damage, reperfusion and oedema are some of the suggested abnormal circulatory causes of laminitis, highlighting the importance in exploring and investigating the vasculature of the equine feet in this study (Heymering, 2010).

Angiogenesis is an example of vasculature adaptability and is important in the development and repair of tissues. It is the process by which capillary networks are remodelled, forming new capillaries, arteries and veins (Folkman and Shing, 1992). Cells that are metabolically stressed/hypoxic activate the endothelial cells lining local blood vessels, initiating angiogenesis and providing the tissue with a sufficient vascular supply (Folkman and Shing, 1992; Stapor *et al.*, 2014). Endothelial cells construct new blood vessels in four sequential steps; the first being the dissolution of the BM by proteases followed by the migration and proliferation of cells in the direction of the angiogenic stimulus, until new capillary tubes are formed (Fan, Jagger and Bicknell, 1995; Taylor, 2008).

1.3.2 Vascular Anatomy of the Equine Foot

The vasculature network of the equine foot provides many components to sustain the anatomical features and maintain metabolic function. Passing into the hoof capsule are the medial and lateral digital arteries, both are branches of the common digital artery. The digital arteries run alongside the medial and lateral surfaces of the P1 where further branches extend, connecting with those on the opposing side, forming an arterial circle, encapsulating the bone (Pollitt, 2004a). The digital arteries descend the limb to the level of the PIP, extending into the heel where they supply the digital cushion, frog, palmar perioplic coria,

coronary coria and lamellar corium of the heel and bars (Pollitt, 2010). Arterial circles are also formed around the mid-section of P2 and at the level of the coronary band where it supplies the digital extensor tendon, coronary corium, proximal lamellae and DIP (Pollitt, 2004a). Before descending to and penetrating P3 the major exiting branches stem at the level of the navicular bone, running in the parietal groove on P3 dorsal surface, where the lamellar coria at the heel and quarters regions are supplied and anastomose with the solar circumflex artery (Parks, 2003; Pollitt, 2010).

Along the solar grooves of P3 is where the terminal section of the digital artery penetrates P3 via the solar foramina, entering the solar canal where the opposing arteries amalgamate, forming the terminal arch (Parks, 2003). Branches from the terminal radiate giving rise to four or five arteries that enter the foramina, exiting on the dorsal surface of P3 and eight to ten arterial branches that exit from the foramina along the solar margin. These branches supply the lamellar corium and then the solar corium after they have anastomosed with the circumflex artery (Pollitt, 2010; Rucker, 2010b).

Blood flow exits via the digital medial and lateral veins where it re-enters the systemic circulation, running parallel to the arteries. All of the veins run in parallel to their arterial equivalent, supplying venous drainage at the differing anatomical regions such as the coronary, sublamellar and solar plexuses, terminally exiting via the pairing medial and lateral veins (Mishra and Leach, 1983; Baldwin, 2010). A difference between arterial and venous supply is the three venous plexuses: the sublamellar, coronary and solar venous, where the terminal venous arch joins the veins draining these plexuses. The two parallel abaxial and axial veins enter the semilunar canal of P3, which then merge to form the terminal venous arch where each vein has both dorsal and ventral tributaries. Where the plexuses and terminal vein adjoin they unite with the venous drainage from the deep bulbar and caudal veins (Mishra and Leach, 1983; Parks, 2003) (Figure 1.8).

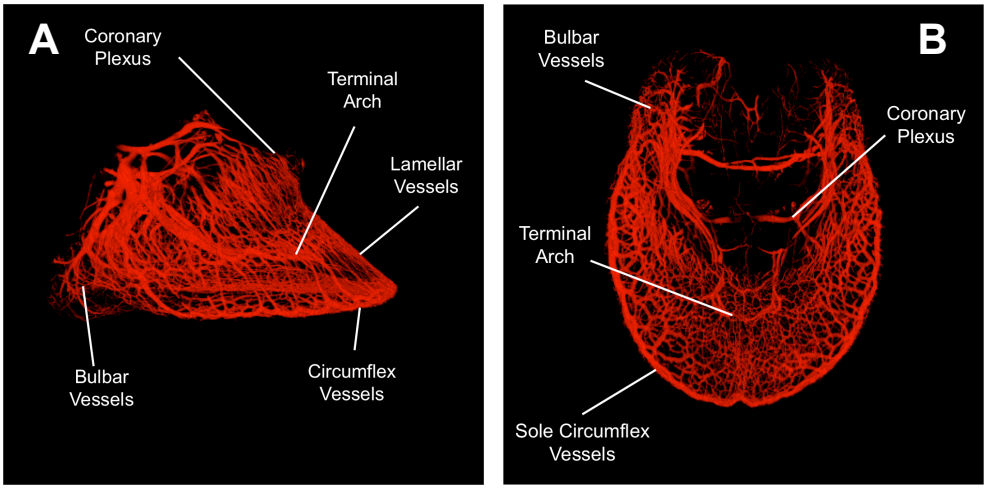


Figure 1.8: µ-CT rendered images of the vascularisation of the equine foot. (A) A slightly oblique medio-lateral view (B) dorso-palmar/plantar view showing the circumflex, bulbar, coronary, terminal arch and lamellar vessels. Source information from (Parks, 2003; Pollitt, 2004a). Images copyright to the author.

1.4 Lamellae, Papillae and Equine Hoof Growth

Keratin is a fundamental structural biological molecule, secondary to that of collagen, forming the principal building block of integument in vertebrates. Skin, hair, fur, wool, horn, claws and nails are all composed of the structural protein keratin, showing a variety of morphologies depending on their purpose. Mechanically keratin is resistant to tension and compression, enabling the integument to be structurally robust and consequentially protective (Mckittrick *et al.*, 2012). The different keratin integumentary appendages all grow from cells surrounding the dermal papillary body. The papillary body provides a greater contact surface for the dermal-epidermal tissues, resulting in a greater surface area for the diffusion of nutritional components supplied to the avascular epidermal cells. Additionally a greater contact surface also increases the integuments' resilience to tensile and compressive forces, which is of primary importance in the equine hoof with respect to the sufficient weight baring ungulates have to withstand (Bragulla, Ernsberger and Budras, 2001). Each dermal papilla has a central arterial supply and venous drainage, extending to

the papillae tip where they are interconnected; the rest of the dermal papilla is composed of connective tissue containing nerve cells for innervation (Lawlor and Kaur, 2015).

The morphological incomplete and truncated cone hoof wall is highly keratinised and comprises of 3 layers; the *stratum internum*, *stratum medium* and *stratum externum*, which is equivalent to the layers of the human nail plate (Kobayashi *et al.*, 1999; Pleasant and McKinlay, 2012). The *stratum internum* is the innermost layer consisting of dermal lamellae that interdigitates with the lamella corium. The largest layer is the *stratum medium*, composed of rigid intertubular and tubular horn (Pleasant and McKinlay, 2012; Goulet *et al.*, 2015). The most superficial layer is the *stratum externum* (or stratum tectorium) which gives rise to the protective waxy substance known as the periople (Kraus, 2014; Goulet *et al.*, 2015). The layer of epidermal cells at the dermal-epidermal junction form a basal cell layer, where each *stratum* are maintained by their own set of papillae (Bragulla, Ernsberger and Budras, 2001; Pollitt, 2010).

The *stratum basale* or basal layer accommodates keratinocyte progenitor cells, which via hemidesmosomes are attached to the BM (Pollitt, 2004a; Bragulla and Homberger, 2009). The proliferation of these cells gives rise to numerous daughter keratinocytes, producing the *stratum spinosum*. As the differentiated keratinocytes migrate away from the dermis, they maturate, forming corneocytes of the *stratum corneum*, alongside denuclearisation and keratinisation of these cells (Bragulla and Homberger, 2009; Pollitt, 2010). The newly formed corneocytes are continually added to the dense matrix of the intertubular and tubular horn thus forming the hoof capsule. All of which contributes to the continual replacement of the inevitable losses of the hoof capsule, as a result of wear and tear from an equids nomadic lifestyle (Pollitt, 2010).

Hoof growth occurs throughout a horse's life, thus the adaptation of lamellae allows the smooth passage of the elongating hoof capsule to slide along the parietal surface of P3 despite their strong attachment. It was once thought that this was a result of the continuous proliferation of epidermal cells lining the epidermal lamellae, enabling the continuous flow of lamellae thus allowing the hoof capsule to elongate distally, however this has since been discredited. It is now believed that it is a consequence of hemidesmosomes destruction and formation, mediated by matrix metalloproteinase proteolytic enzymes and their inhibitors, adjusting the attachments of the basal epidermal cells to the basement membrane concurrently with hoof growth (Daradka and Pollitt, 2004).

1.6 Lameness & Laminitis

Lameness is a common disorder among ungulate species and could be considered pandemic, affecting around 20% of horse's, 36.8% of the dairy population and 5% of the sheep population in the UK at any one time (Barker et al. 2010; Menzies-Gow et al. 2010; Slater 2016; Smith et al. 2017). Consequently the high incidence of lameness and its multifactorial nature makes it difficult to implement curative treatments thus comprising the animal's welfare and having substantial impact on the economy (Ranjbar *et al.*, 2016). Regarding horses, lameness and laminitis are the most frequently reported disorders and the most common basis for equine euthanasia (Menzies-Gow, 2006). Annually it is estimated that the average bovine case of lameness costs around £178 with on average a financial loss of £100 per cow (Bell, 2015). In sheep the financial losses in the UK per year are estimated at £10m, with the implementation of treatment and/or performance/livestock loss (Winter, 2008).

Pathomorphological changes of keratinised integumentary digital appendages are not only observed in ungulate species, clawed and nailed animals are also affected by the pathological afflictions.

Examples of this in the human nail are disorders such as ingrown nail, pincer nail and spoon-shaped nail, all a repercussion of pathological changes, causing deformities and pain (Rauch and Cherkaoui-Rbati, 2014). Onchopathy in canines is relatively rare, however claw deformation and abnormal curvature does occur as response to changes in growth rate or as a ramification of other pathological abnormalities, such as a bacterial infection (Mueller, 1999; Warren, 2013). Lamellae separation and therefore sloughing of the claw distally, are symptoms observed in canine claws, similarly to that of a laminitic hoof (Parks and O'Grady, 2003; Hunt and Wharton, 2010). Onycholysis is particularly comparable to the observations made in chronic laminitis, which is the separation of the claw from the claw bed comparable to the sloughing of the hoof capsule along the parietal surface of P3 (Mueller, 1999; Pollitt, 1999).

The suffix "-itis" is indicative of inflammation, thus the hoof capsular affliction commonly referred to as laminitis implies that the disease is a subsequent cause of lamellae inflammation (Menzies-Gow *et al.*, 2010; Porter and Kaplan, 2013). However with varying definitions of this pathomorphological condition, the one mostly accepted today is the concept of the failure of lamellar attachments between the inner hoof capsule and the parietal surface of P3 (Pollitt, 1999). Therefore the suffix "-itis" is not fitting to the current hypothesis, so perhaps a new term such as "lamella-associated foot lameness" would be a better description of the condition (Paul, 2016). Laminitis is the current accepted term, so consequently will be employed throughout this study.

Laminitis is more commonly presented in the forelimbs than in the hindlimbs, however it can affect all four feet simultaneously, the two hindlimbs or just a single foot as seen in supporting limb laminitics (Baxter, 2011). The increased prevalence observed in forefeet is perhaps a consequence of increased weight bearing in the cranial region in contrast to the weight borne caudally (Floyd and Mansmann, 2007). The severity and progression of laminitis is categorised into

three or four phases, the first being the developmental/prodromal phase (Hood, 1999; Menzies-Gow, 2006). This phase predates the onset of affliction, and can last anywhere between 8 to 40 hours (Hood, 1999; Pollitt, 2004b). Succeeding this is the acute phase where symptoms of pain arise, thus clinical signs such as lameness, the “rocked back stance”, increased digital pulse amplitude and an increase in lower limb temperature can be observed (Hood, 1999). This phase usually lasts between 24 and 72 hours, resolution of the disease will cease its progression or it can advance into the subacute or chronic phase (Hunt and Wharton, 2010). The subacute phase is seen beyond the 72 hour period of the acute phase, showing laminitic clinical signs however P3 displacement/sinking does not ensue. Lastly is the chronic phase, which can last indefinitely, with radiographic investigation morphological changes of the lamellae along the parietal surface of a displaced or sunken P3 can be seen (Hunt and Wharton, 2010; O’Grady, 2010). The extremity of the lameness can be graded using physical signs, there are four categories to the grading system:

Grade 1: Lameness is not observed in walk but a shortened gait is observed in trot and there is frequent lifting of alternate feet intermittently at rest.

Grade 2: The horse is willing to walk but the gait is stilted and subsequently tracking up is reduced. The picking up of a foot off of the ground can be done but with some resistance from the horse.

Grade 3: The horse is reluctant to move at all and an attempt to pick up a foot is proves great difficulty.

Grade 4: The horse will not much unless forced to do so (Stashak, 2013).

1.7 X-ray μ-Computed Tomography

Within veterinary medicine, the use of computed tomographic (CT) imaging is becoming increasingly common as a diagnostic imaging modality, although its use in the detection and management of laminitis is not a routine procedure, it elicits the need for further investigation, particularly with the increase in utilisation for the assessment of complex foot lameness (Puchalski, 2012). The technological advances in imaging techniques has enabled the investigation of the physiology of soft and biomineralised tissues to be assessed on a micrometre scale, without the requirement for an invasive/destructive technique, such as dissection (Neues *et al.*, 2007).

CT imaging is an imaging modality that uses x-rays to create detailed images around the principle of attenuation. Attenuation is the reduction or loss of intensity, in this circumstance the reduction photon-electron interactions due to the matter, which they are trying to penetrate, hence this matter is known as the absorber. The linear attenuation coefficient, μ, is defined as the proportion of incident photon intensity absorbed or scattered per unit thickness of the absorber, measured in cm^{-1}. Photon energy (E) and atomic number (Z) both influence the linear attenuation coefficient. In uniform absorbers, photon intensity (I) decreases exponentially as a function of absorber thickness (x) (equation 1.1) (Kinahan, Hasegawa and Thomas, 2003; Wyant, Capasso and Wolbarst, 2013).

$$I = I_0 e^{-\mu x} \qquad (1.1.)$$

where I_0 is radiation intensity when no attenuating material is in its line.

Total attenuation is influenced by two variables, the photoelectric effect and Compton scattering (Kinahan, Hasegawa and Thomas, 2003). Compton scattering is the process where energy of the photon is transferred to an electron, giving rise to secondary photons with lower

energies and/or deviation from the direction of the primary path (Carlsson, 1999). On the other hand photoelectric absorption is the complete transfer of photon energy as it is absorbed. Photoelectric absorption is strongly dependent on Z and E where Compton scattering is determined fundamentally by Z, while E has minimal impact (Kinahan, Hasegawa and Thomas, 2003). With reference to the attenuation of biological soft tissues, their contrasts are low as a result of low Z, high E and uniform density (Carlsson, 1999; Mizutani and Suzuki, 2012). For soft tissues and bone, photon energies below 30keV and 50keV results in the total attenuation being dominated by the photoelectric effect and at higher photon energies in the range of 200-1000keV it is dominated by Compton scattering. In x-ray radiographic imaging E ranges from 30 to 130keV, therefore attenuation of CT images is a consequence of both photoelectric absorption and Compton scattering (Kinahan, Hasegawa and Thomas, 2003). As CT detectors purely detect I, images showing greater contrast are an outcome of superior photoelectric absorption, where E levels are lower (Mizutani and Suzuki, 2012). X-ray laboratory CT scanners usually consist of characteristic sharp peaks and white x-rays with a broad profile; hence voxel values do not represent the linear attenuation coefficient, μ. However the opposite is true in a synchrotron CT beamline.

The use of a high resolution CT scanner can produce single slice image stacks and 3D volumetric images. The object under investigation is rotated 180° on an axis perpendicular to the radiation beam. Concurrently x-rays are fired linearly at the absorber, and the transmission signals produced are detected by a computer (Drangova *et al.*, 1993). The transmission signals are recorded as a function of rotation angle and the linear attenuation coefficient is then calculated using a suitable algorithm. Reconstruction of the object involves the use of the μ values for each voxel, thus recreating a 3D image of the sample (Carlsson, 1999).

1.8 Aims and Objectives

The fundamental aim of this project was to combine both physics and biology, via the use of a laboratory μ-CT scanner to investigate the anatomical components of the equine foot. With all biological processes inextricably linked to the laws of physics, it is only equitable that the connection between physics and anatomy is acknowledged. In particular any correlations found between the pathomorphological status and abnormalities in the equine feet. Consequently adding a novel dimension to the study and developing new methodologies for this research field.

Objectives:

- To mathematically model the different physical descriptors and their morphological state in the equine foot.
- Measure both the dorsal hoof wall and P3 curvatures.
- Extract the cortical bone thickness of P3 and its thickness in different regions.
- Analyse the degree of trabecular bone anisotropy of P3.
- To measure the volume of corium.
- Analyse the vasculature by extracting data of the branch lengths, the degree on bundling and the mean lumen diameter.

The cadaveric material used was sourced from a university-approved abattoir, howbeit the medical history and more importantly the history of lameness/laminitis was unknown at the time of slaughter. Prior to this study a correlation between P3 displacement and hoof curvature was observed, in accordance with this observation it was assured that hoof wall curvature could be implemented as the primary comparative physical descriptor.

2 Materials and Method

The collection of cadaveric material and perfusion of the limbs was carried out by Emily Paul, Dr Cyril Rauch and Ramzi-Al-Agele. The equine limbs were transported to the Hounsfield Facility, University of Nottingham, where Dr Craig Sturrock and Brian Atkinson scanned the equine feet and produced the micro CT images. The images were processed and orientated by Emily Paul. Both Emily Paul and the author carried out analysis on dorsal hoof wall curvature, bone curvature, bone thickness and trabecular bone anisotropy. The author executed the dorsal hoof wall thickness, vasculature and corium analysis.

2.1 Foot collection and preparation

2.1.1 Abattoir collection and preparation

Equine forelimb collection and preparation was carried out by Emily Paul, Dr Cyril Rauch and Ramzi Al-Agele. The forelimbs were collected from an abattoir at Tockenham Corner, Swindon. Prior to the collection, full ethical approval was given from the University of Nottingham ethical review committee. The forelimbs were perfused and fixed on site in order to preserve the anatomical features prior to CT scanning. To achieve fixation the arteries located on the lateral and medial palmar/plantar surface were cannulated at fetlock height. The equine limbs were flushed with 1X phosphate buffer solution (PBS) ensuring that blood exited from both the lateral and medial veins until the fluid being flushed was clear (free from blood), tissue was then fixed. Ligatures were then tied loosely around each artery/vein bundle and were pressurised and fixed with 4% paraformaldehyde (PFA), the ligatures were tightened and tied off whilst removing the catheters.

The forelimbs were transported to the School of Veterinary Medicine and Science, Sutton Bonington, through approved means. On arrival the limbs were refrigerated for 24 hours before the final preparation.

The final preparation involved: cleaning the external hoof capsule thoroughly, numbering/labelling the feet, removal of shoes, trimming any excess hair and disarticulation between P1 and P2. Until required for CT scanning the prepared feet were stored at -20°C.

2.2 CT scanning

2.2.1 Laboratory Micro-Tomography

The micro CT images were produced by Dr Craig Sturrock (co-director and manager of the Hounsfield Facility, University of Nottingham) and Brian Atkinson (research technician at the Hounsfield Facility), using a GE phoenix v|tome | x m (Figure 2.2), at the School of Bioscience's Hounsfield Facility. The machine was calibrated and the contrast and resolution were optimised through minor adjustments. The distance between the sample and x-ray gun was altered to optimise the resolution. For contrast the photon energy (voltage) and flux (current) were adjusted. Approximately 24 hours prior to scanning, the feet were removed from the freezer and each foot was packaged in a plastic storage container surrounded by polyethylene packing foam to immobilise the foot. Each box was labelled with the foot's individual identification number. Once removed from the freezer the feet were placed in a refrigerator for approximately 6 hours to allow them to thaw, before transporting them to the scanning facilities. For whole-foot scans, a voltage of 125keV and a current of 320μA were calibrated and selected ensuring that the full available spectrum of grey values was utilised. Each foot was scanned and the data was stored on the facilities system prior to Emily Paul manually processing them.



Figure 2.2: The GE phoenix v|tome|xm located at the Hounsfield facility. Photo courtesy of Emily Katy Paul.

2.3 CT image processing

2.3.1 Hoof Orientation and Planar Adjustments

Hoof orientation and planar adjustments were made by Emily Paul. The use of Volume Graphics (Heidelberg, Germany) software was required in order to make the volumetric image data from the laboratory usable. Prior to resaving the utilisable images, planar adjustments were made to the 3D images. Due to the packaging of the feet it was not possible to ensure that the feet were kept level and straight. The “transform” feature on the volume graphics software was used to make a visual assessment of XY (axial), XZ (coronal) and YZ (sagittal) planar sections. The images could also be re-orientated around the X, Y and Z axes respectively. After completion of the necessary adjustments the images were “sliced” and exported as TIFF image stacks.

2.3.2 Bone Segregation

Bone Segregation was carried out by Emily Paul. Using the surface determination function on Volume Graphics, the bone was segregated from the surrounding tissue. An area of the hoof capsule containing no

bone was selected as the background material, and an area at the base of the extensor process on P3 was selected as the foreground material. The maximum radius set to zero, tolerance level to 30,000, the mode to static and the command to ‘stay in ROI’ (region of interest), creating a ROI from the threshold bone. Images of P2, P3 and the navicular bone were then exported individually and collectively, saving the files as a TIFF image sequence. Fiji ImageJ was then used to import and binarise the image stacks using the built-in ‘default’ thresholding algorithm. The image stacks were then ready for analysis and 3D reconstruction work.

2.4 Physical descriptors

For each hoof the CT scans were used to obtain physical measurements such as dorsal curvature and dorsal wall thickness.

2.4.1 Dorsal curvature

2.4.1.1 CT scans

For each hoof, the dorsal wall curvature was calculated using the 2D images stacks in the YZ plane. The image was imported into Fiji ImageJ and rotated and/or flipped on the horizontal axis where needed. The ROI was selected using the rectangular selection tool, making sure the image was cropped so that the tip of the dorsal wall was in the bottom left corner and the periople in the top right. The scale was set and 18 equidistant vertical lines were drawn over the image slice using a grid overlay macro (Rasband, 2003) . Points were plotted from left to right where the vertical lines/boundaries intersected the dorsal wall and the Cartesian coordinates of these points were measured (Figure 2.3).

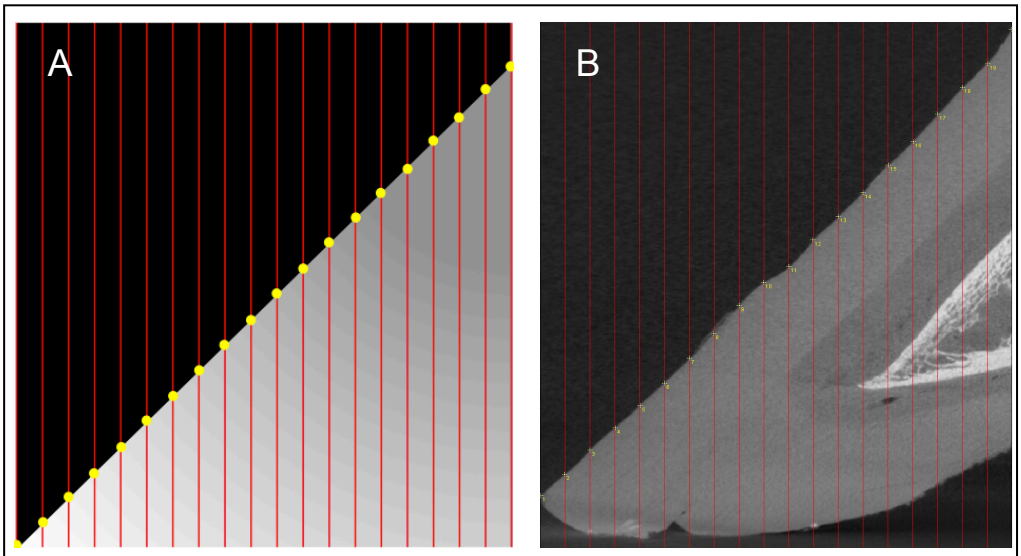


Figure 2.3: Calculating the dorsal curvature: (**A**) A schematic of a CT scan showing the background in black and the equine foot in grey. The intersection between each red vertical line and the dorsal wall were marked with a yellow marker and the co-ordinates of each marker were recorded. (**B**) A screenshot from the actual recording. Images copyright to the author.

The dorsal wall curvature, *C*, at each point measured on the dorsal wall surface was calculated using Microsoft Excel's polynomial curve fitting function, and a modified version of the differential calculus equation (eq. 2.1) (Paul, 2016).

$$C = \frac{y''}{(1+ y\prime^2)^{3/2}} \qquad (2.1)$$

Where y' and y" are the primary and secondary derivatives of y.

Both x and y were rescaled to avoid computational problems with the multiplication of very small and very large numbers. The new variables $\hat{x}$ and $\hat{y}$ are defined below (eq. 2.2 and 2.3)

$$\hat{x} = \frac{x}{[x]} \qquad (2.2)$$

$$\hat{y} = \frac{y}{[y]} \qquad (2.3)$$

Where [x] and [y] are the mean values of x and y. $\hat{y}$ ($\hat{x}$) were plotted and a polynomial curve was fitted to the order of 3, creating a $\hat{y}$ = f ($\hat{x}$) equation.

(2.4)

$$\hat{y} = a_3\hat{x}^3 + a_2\hat{x}^2 + a_1\hat{x} + a_0$$

$$\hat{y}' = 3a_3\hat{x}^2 + 2a_2\hat{x} + a_1 \quad (2.5)$$

$$\hat{y}'' = 6a_3\hat{x} + 2a_2 \quad (2.6)$$

Where $\hat{y}'$ is the first derivative and $\hat{y}''$ is the second derivative for the mean values of x and y, using a polynomial curve.

The R^2 value of the polynomial curve fitted was consistently ≥ 0.95. The curvature at each point was then calculated by the modified equation (eq. 2.7), following the chain rule method.

$$C = \frac{[y]\cdot\frac{\hat{y}''}{[x]^2}}{\left(1+\left([y]\cdot\frac{\hat{y}'}{[x]}\right)^2\right)^{3/2}} \quad (2.7)$$

The data points collected were not spaced completely equidistant along the x-axis, due to collection method limitations. To account for this, the integral $\int C\, d\hat{x}$ was calculated and used in the average curvature calculation (eq. 2.8). Approximate values were then calculated, treating the sections outlined by two equivalent pairs of *x* and *C* values as trapezia on a *C(x)* curve and calculating the sum of their areas.

$$\int C\, d\hat{x} = \sum_{i=1}^{20} \frac{(C_i + C_{i+1})(\hat{x}_{i+1} - \hat{x}_i)}{2} \quad (2.8)$$

The average curvature $\langle C \rangle$ was then calculated (eq. 2.9).

$$\langle C \rangle = \frac{\int C\, d\hat{x}}{\hat{x}_S - \hat{x}_L} = \frac{\int C\, dx}{x_S - x_L} \quad (2.9)$$

Where $\hat{x}_S$ is the smallest and $\hat{x}_L$ is the largest $\hat{x}$ value.

2.4.2 Dorsal wall thickness

The dorsal wall thickness was measured, using 2D image stacks in the YZ plane. Some feet could not be analysed due to the removal of coronary tissue prior to scanning, for immunohistochemistry analysis by Ramzi Al-Agele. Fiji ImageJ was used to import the image stacks and

rotate/flip the slices if required. The ROI was selected using the rectangular selection tool ensuring both the solar margin and coronet region were contained (Figure 2.6). The solar margin was located on the bottom left corner and the coronet in the top right. The scale was set and a grid overlay macro was used to plot 9 equidistant vertical lines. Using the straight line tool, a line perpendicular to the dorsal wall was then plotted. Starting from the intersection between the external dorsal wall and grid line to the hoof wall/laminae boundary. The line was then measured and recorded in Microsoft Excel. This was repeated 9 times going from right to left, meaning the last point would intersect the left border, not a grid line. For each hoof the 10 measurements recorded were used to calculate the mean average. The feet were split into two anatomical sections giving us the average thickness values for both the toe and quarters regions. The inner third slices were taken as the toe region and the outer two thirds as the quarters. 44 hooves were used for the quarters and 41 for the toe region.

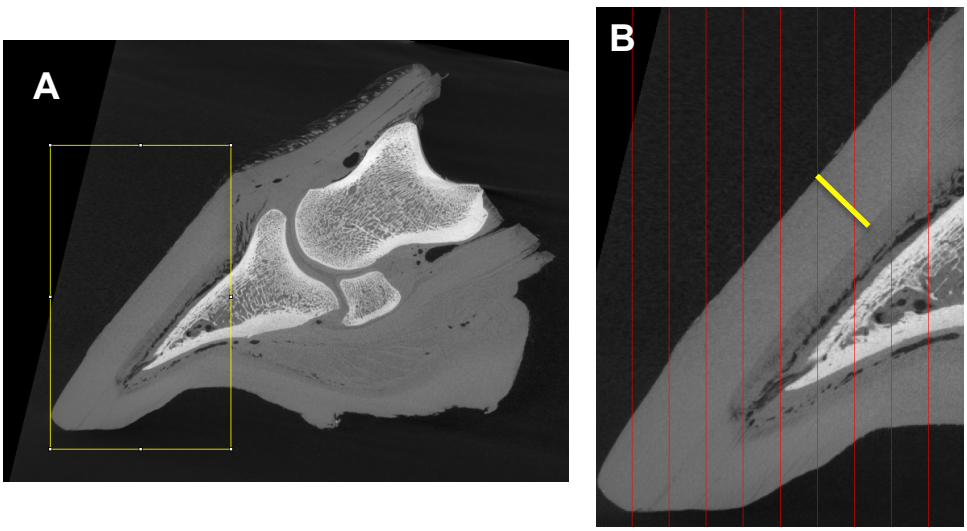


Figure 2.6: Dorsal hoof wall thickness analysis. (**A**) CT scan showing the rectangular selection tool highlighting the ROI. (**B**) The ROI with the grid overlay. The yellow line plotted over the image is an example of how the dorsal hoof wall thickness was measured for each intersection between the grid overlay and the dorsal hoof wall. Images copyright to the author.

2.5 Bone Analysis

Bound to the hoof capsule via the intermediary lamellae is P3, a bone of paramount importance in the equine foot and therefore is the subject of investigation. As indicators of its pathophysiological state, dorsal bone curvature, cortical bone thickness and the degree of trabecular anisotropy were measured.

2.5.1 Bone curvature

The bone curvature was calculated in a similar manner to the dorsal curvature of the hoof wall as described in section 2.4.1.1. A total of 43 hooves were analysed, 27 were analysed by Emily Paul and 16 by the author. The centre sagittal section was imported into Fiji ImageJ and flipped/rotated as required. The scale was set and the image was cropped so only the ROI was displayed. The ROI boundaries lie between the tip of P3 and the base of the extensor process. The image was orientated so the tip was in the bottom left corner and the extensor process in the top right. The vertical line overlay macro was used and points were plotted where the dorsal surface of P3 intersects the vertical line. Using the same calculation as stated in section 2.4.1.1 the curvature was calculated in Microsoft Excel after importation of the Cartesian coordinates.

2.5.2 Cortical bone thickness

A total of 44 hooves were imported to Fiji ImageJ for bone thickness measurements, 20 were processed by Emily Paul and 24 by the author. The binary bone image stacks were imported into Fiji and the scale was set. The polygon select tool and ROI manager was used to capture the anatomical ROI (Figure 2.7). The areas “dissected” included the upper and lower toe and quarters walls, the toe and quarter solar surface, the toe and quarter solar margins, the articular surface to P2, the articular surface to the navicular bone, the collateral ligament attachments, the

flexor surface and the extensor process. The sections were split into toe and quarter regions as mentioned in section 2.4.2, and the upper and lower halves were classified as the proximal and distal portions.

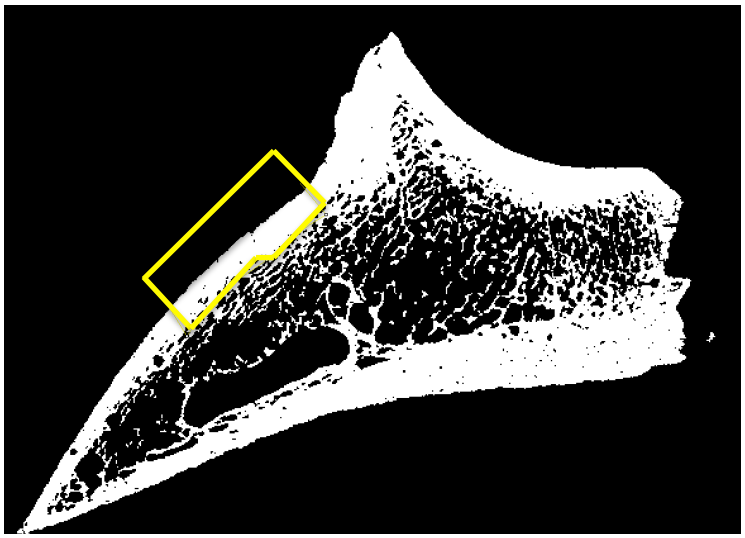


Figure 2.7: Binary image of P3. The polygon select tool was used to select the ROI for the calculation of the cortical thickness. Image copyright to the author.

The average 3D thickness for each region of interest was calculated using the ImageJ plugin, BoneJ (Doube *et al.*, 2010) and its thickness function. The data for each different cortical section was then imported into Microsoft Excel, calculating ROI thickness ratios to compare between the different regions. This would compensate for differences in scan setup which could affect the grey contrast values and thus thresholding. It would also account for differences in foot size.

2.5.3 Bone Anisotropy

44 whole foot 2D greyscale images were imported into Fiji ImageJ, 25 were completed by Emily Paul and 19 by the author. After importing the image stack belonging to the foot of interest, the scale was removed and set to pixels. The image was then flipped and/or rotated so that the dorsal lamellar surface of P3 was vertical. Focusing on the central sagittal slice, the rectangular selection tool was used to select the ROI.

The ROI included the tip of the trabecular bone to the base of the extensor process. The selected region was then divided by 10, using the overlay function and the rectangular selection tool. In the second most distal section, the overlay function was used to trace a square in the trabecular region excluding any cortical tissue (Figure 2.8). A duplicate of this section was then created, rendering the depth equal to that of both the height and width, creating a cube. The centre sagittal section was now the central slice of the cube. Using the default threshold function, the cube was binarised for analysis. The degree of anisotropy (DA) and the mean intersect lengths (MIL) were calculated using the ImageJ plugin, BoneJ and its anisotropy function (Doube et al. 2010, Ketcham & Ryan 2004). The Eigen values and the MILs were

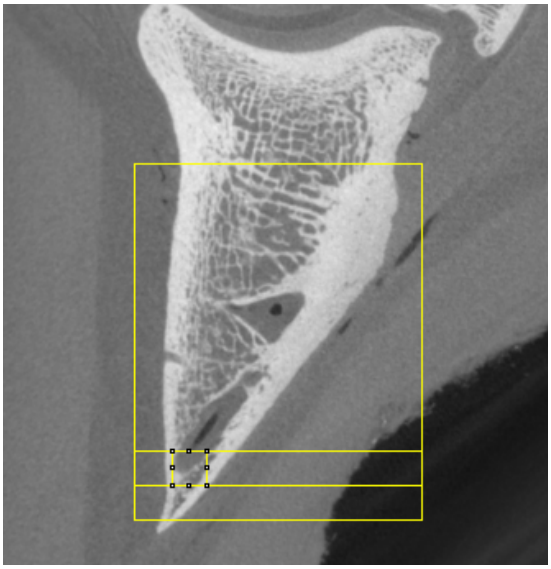


Figure 2.8: Trabecular bone selection. A cube selection of trabecular bone from the distal portion of P3. Image copyright to the author.

then recorded in Microsoft Excel.

The plugin calculates the MIL and DA by virtually placing a random point of origin in the ROI and a large number of longitudinal equal vectors. The boundary between the difference in attenuation (in this case white and black because it was binarised) of bone and the background periodically intercepts these longitudinal vectors, this is counted as a boundary hit. The number of boundary hits and the vector

lengths are then utilised by ImageJ to calculate the MIL (eq. 2.15) and DA (2.16).

$$MIL = \frac{\vec{L}}{n_{BH}} \tag{2.15}$$

Where n_{BH} is the number of boundary hits and $\vec{L}$ is the vector length.

In order to calculate the DA (eq. 2.16) the programme must use two of the three eigenvalues measured.

$$DA = 1 - D_1/D_3 \tag{2.16}$$

Where D1 is the lowest eigenvalue (short axis) and D3 is the highest (long axis), with the greatest distance between boundary hits.

By multiplying each vector with its MIL it allows the programme to create a point cloud (Figure 2.9). The point cloud illustrates both the degree of anisotropy and the predominant direction of anisotropy by visualisation of the axes and its ellipsoidal shape. The lengths of the ellipsoids axis is represented by the eigenvalues and the direction/orientation is represented by the eigenvectors.

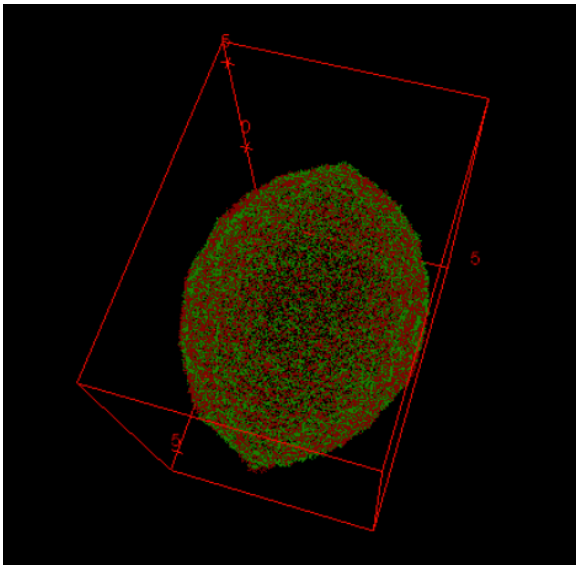


Figure 2.9: Mean intercept length vector cloud. BoneJ plugins anisotropy function permits the illustration of the axes of anisotropy shown above in the 3D graphic result of the MIL vector cloud. Image courtesy of Emily Katy Paul.

2.6 Vasculature Analysis

To investigate changes in the vasculature among different horse feet, the lumen diameter, total branch length of the blood vessels and the volume of the laminae were all measured. For the lumen diameter calculations the hoof was split into different sections, similar to that in section 2.4.2 and 2.5.2. A total of 28 hooves were used for the very distal toe region (toe tip), and a total of 16 hooves were used for the toe and quarters at both the coronet and heel.

2.6.1 Mean lumen diameter

A vasculature macro was used with Fiji ImageJ to isolate the vasculature from micro CT images, using a script written in ijm format. The file names, image numbers and document pathways could be changed for each hoof image stack. The macro worked by using the isodata autothreshold algorithm, setting the scale, binarising and duplicating the image sequence. One duplicate image sequence was inverted and used as a mask. The two duplicate images were then multiplied together resulting in a 2D image stack displaying only the vasculature (in white).

After running the macro the rectangular selection tool was used to select the ROI. The ROI was then duplicated and the rectangular selection tool was used to select any artefacts on the image slices. Artefacts were highlighted using the selection tool and added to ROI manager. After searching through the entire image stack, the ROIs were interpolated and the areas were filled removing all artefacts. The thickness function of the BoneJ plugin was then used to calculate the lumen diameters. Once calculated the mean, standard deviation and maximum measurements were all imported into Microsoft Excel.

2.6.2 Total branch length

A total of 28 hooves were analysed for the vasculature branch lengths in the distal toe region. The vasculature macro, rectangular selection tool and the removal of artefacts were processed in the same way as stated in section 2.6.1. The image stack was then skeletonised, using the skeletonise (2D/3D) function of the skeleton plugin. By skeletonising the image, a thin shape that is equidistant to its boundaries was created. This emphasises properties such as length, direction and connectivity. To analyse the image, the analyse skeleton function of the skeleton plugin was used, this works by tagging all pixels/voxels in a skeleton image. The number of junctions, quadruple/triple points and branches was then counted. The maximum and average lengths were also measured. The voxels were classified into 3 categories depending on their 26 neighbours; End-point voxels were classified as having less than 2 neighbours, junction voxels as having greater than 2 and slab voxels having exactly 2.

The analysis of the skeleton gave the skeleton ID, number of branches, number of each voxel type, number of triple/quadruple points and the average and maximum branch lengths. The detailed information was selected and this gave the calibrated branch length, skeleton ID, 3D coordinates of the extremes of the branch and the Euclidean distance. To avoid analysing data caused by noise interference, skeletons with 20 branches or less were removed. Data for the remaining branches were imported into Microsoft excel, this included the branch lengths, the Euclidean distance and the 3D coordinates of the extremes of the branches.

2.6.2.1 Stretched and bundled vasculature

The vasculature branch lengths were categorised using the Euclidean distance to calculate the vasculature conformation (*VC*) within the dorsal toe region.

(2.17)

$$VC = L \div E$$

where *VC* is the vasculature conformation value, *L* is the vasculature branch length and *E* is the Euclidean distance.

The vasculature conformation value was used to conditionally select the vasculature branches that were stretched or bundled (eq. 2.18 and 2.19).

$$IF\ VC > 1 = \text{Bundled vasculature} \quad (2.18)$$

$$IF\ VC = 1 = \text{Stretched vasculatured} \quad (2.19)$$

The total sum of stretched branches and the total sum of bundled branches was calculated for each equine foot. The percentage of stretched to bundled vasculature was then calculated (eq. 2.20).

$$\%\, Stretched/Bundled\, Vasculature = \frac{no° Stretched}{no°\ Bundled}\ x\ 100 \quad (2.20)$$

where the percentage of stretched to bundled vessels was used as another physical descriptor to compare the different equine feet.

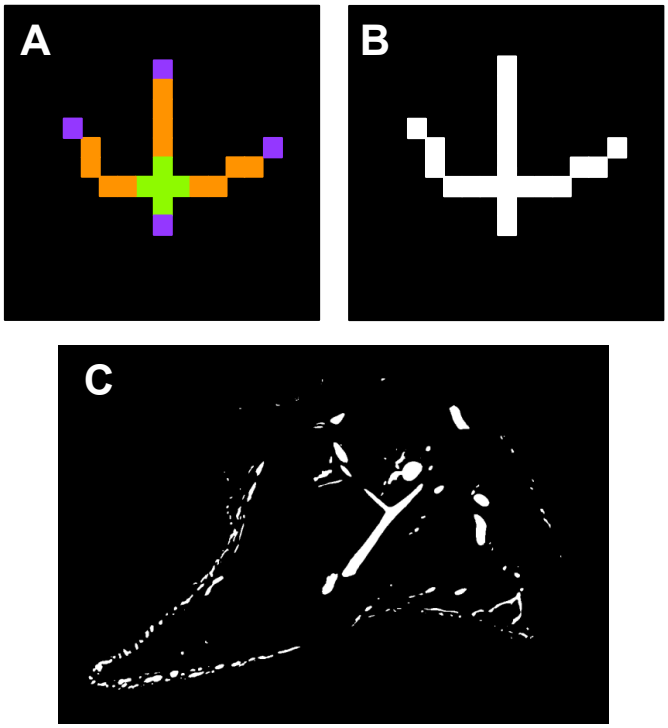


Figure 2.10: A schematic of voxel categories and image of the skeleton format. (A) Skeleton with voxel types highlighted; End voxels (purple), junction voxels (orange) and slab voxels (green). **(B)** Schematic of a skeletonised image. **(C)** A CT image slice of the equine foot using the skeletonise function of the skeleton plugin, highlighting only the vasculature. Images copyright to the author.

2.6.3 Volume of corium

The volume of corium was calculated using Fiji ImageJ and Microsoft Excel, for a total of 44 hooves. Each image sequence was imported into ImageJ in the XY plane (axial). For those in the YZ/XZ plane the image was re-sliced, resulting in an axial view of the image stack. Using the rectangular selection tool, the most dorsal third of the toe region was selected and duplicated. The scale was set and the first image slice was selected. The first image slice was defined as the slice where both the upper left and right corners of the selection border intersected with the dorsal surface of P3. The vertical line overlay macro was used to plot 18 vertical lines over the image. Using the multi-point selection tool, points were plotted where the dorsal surface of P3 intersected a vertical line. 20 points were plotted, 18 from the vertical line and P3 intersections and 2 from the boundary border and P3 intersections. The

x and y co-ordinates where then imported into Excel. For the same image slice, points were plotted along the palmar/plantar surface of the hoof wall and recorded. This was repeated in intervals of 20 slices until the ROI could no longer be identified.

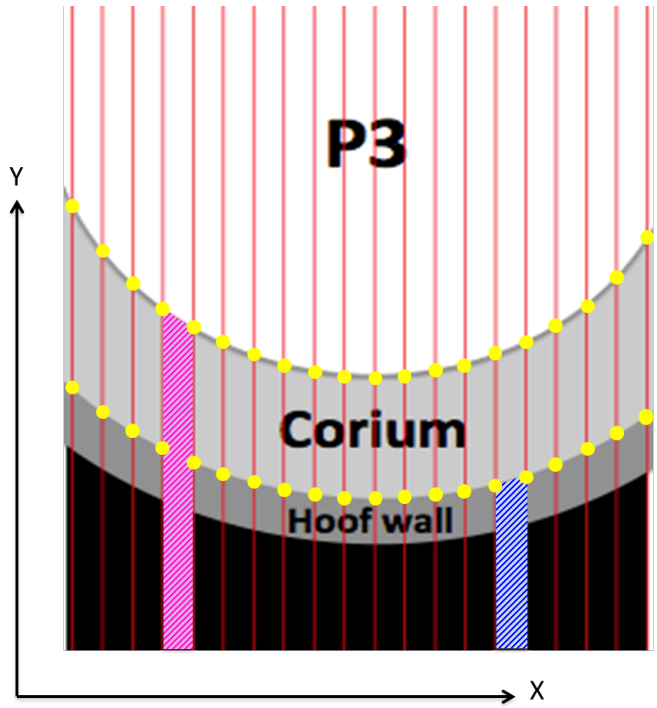


Figure 2.11: A diagram of an axial CT image of the equine hoof used for corium volume analysis. The pink shaded region highlights the area under the pedal bone curve. This was calculated for each interval to give the total area. The blue shaded region is the area under the dorsal corium surface. This again was repeated for each interval to give the total area. Diagram copyright to the author.

The volume of corium, *V,* was calculated using the x and y co-ordinates measured. This was completed in a series of steps before being able to calculate the total volume.

$$I_{pb} = \left(x_{pb(n+1)} - x_{pb(n)}\right) \times \left(y_{pb(n)} + \frac{\left|\left(y_{pb(n+1)} - y_{pb(n)}\right|}{2}\right) \quad (2.21)$$

$$I_{hw} = \left(x_{hw(n+1)} - x_{hw(n)}\right) \times \left(y_{hw(n)} + \frac{\left|y_{hw(n+1)} - y_{hw(n)}\right|}{2}\right) \quad (2.22)$$

Where I_{pb} is the integral for the pedal bone lamellar surface and I_{hw} is the integral for the lamellar surface of the hoof wall between 2 consecutive x and y co-ordinates. The x and y co-ordinates also have a subscript of pb or hw denoting which boundary surface the co-ordinate relates to. The first x and y co-ordinate from each image is given by the symbol *n,* where *n+1* is the next consecutive value. This was repeated using all 20 co-ordinates. The sum of these values was then calculated using the equation below.

$$I_{corium} = I_{pb} - I_{hw} \quad (2.23)$$

$$V = \sum_i \frac{I_{corium}(z_{i+1}) + I_{corium}(z_i)}{2} \; x \; e \quad (2.24)$$

Where I_{corium} is the intergral for the corium, e is the distance in mm between each interval, z is a slice selected for analysis and i is the number for each selected slice at the different intervals.

2.7 Anatomical Image Rendering

Depending on the tissue-type, a number of threshold algorithms were used to convert the images to binary image stacks (see section 2.3 on CT image processing for thresholding specifics). The structures of interest on the binary image stacks were represented in white and had a grey-level value of 255, whilst the surroundings have a value of 0 resulting in black. The volumetrically rendered images were then viable to use with the 3D viewer plugin.

3 Results

3.2 Physical Descriptors

3.2.1 Categorising Data

The data was categorised using the positive (convex) and negative (concave) curvatures of both the dorsal hoof wall and dorsal surface of the P3 as presented in Figure 3.1. Four possible combinations were formed, as both physical characteristics could either be convex (positive) or concave (negative).

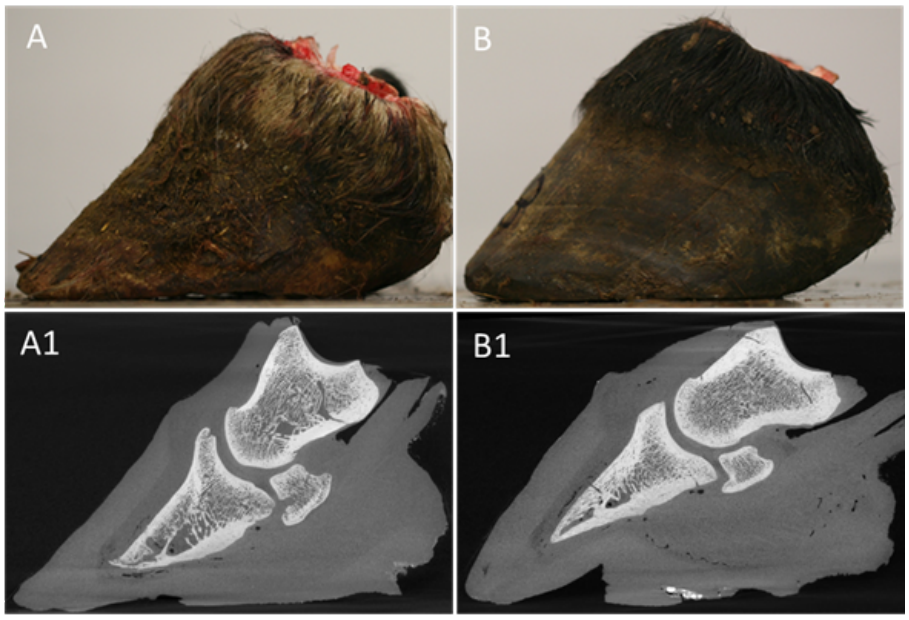


Figure 3.1: Photos and CT scans displaying concave and convex curvatures of both the dorsal wall and third phalanx. (A) Photo of hoof with a concave dorsal wall curvature. **(A1)** CT scan of hoof A showing a concave third phalanx. **(B)** Photo of hoof with a convex dorsal wall curvature. **(B1)** CT scan of hoof B showing a convex third phalanx. (Photo courtesy of Ramzi Al-Agele).

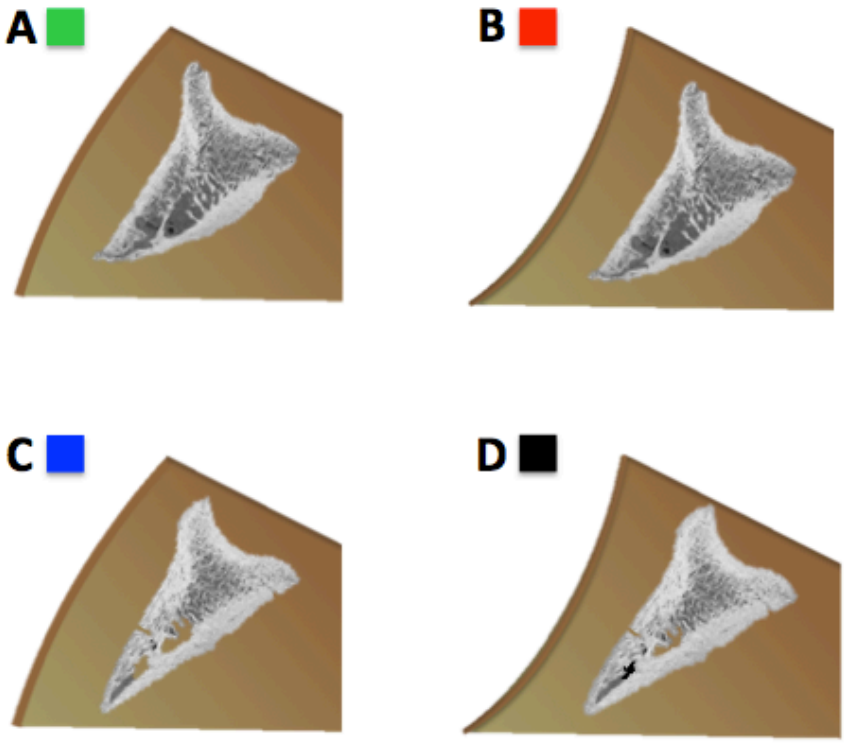


Figure 3.2: A schematic of the colour coded categories. (A) Green = Negative dorsal wall curvature and positive third phalanx curvature. **(B) Red** = Positive dorsal wall curvature and positive third phalanx curvature. **(C) Blue** = Negative dorsal wall curvature and negative third phalanx curvature. **(D) Black** = Positive dorsal wall curvature and negative third phalanx curvature. Diagram copyright to the author.

The four possible combinations were colour coded as presented in Fig 3.2: -

Green = positive P3 and negative dorsal hoof wall

Red = positive P3 and positive dorsal hoof wall

Blue = negative P3 and negative dorsal hoof wall

Black = negative P3 and positive dorsal hoof wall as

Categorisation of the equine feet was used in analysis in order to make a comparison between hoof and P3 shape against other physical descriptors.

3.2.2 Dorsal wall curvature and thickness

The curvature and thickness of the dorsal hoof wall were investigated, using the coronet band and solar margin as limits. The dorsal hoof wall thickness in the toe region was presented as a function of the dorsal hoof wall curvature, as presented in Fig 3.3A and in the quarters region in Fig 3.3B. Their respective linear regression analyses are displayed in Table 3.1.

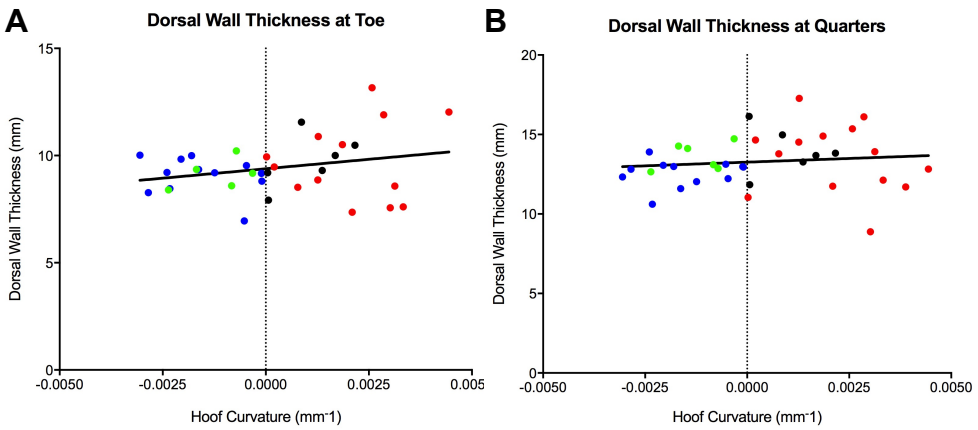


Figure 3.3: The relationship between dorsal wall curvature and thickness. (A) Shows the dorsal wall thickness at the quarters as a function of the dorsal hoof wall curvature. **(B)** Shows the dorsal wall thickness at the toe as a function of the dorsal hoof wall curvature. For the quarters ***n***=38. For the toe ***n***=36.

	Goodness of Fit (R^2)	**Deviation From Zero (P)**
A – Dorsal wall thickness as a function of hoof curvature (Toe region)	0.06541	0.1322
B – Dorsal wall thickness as a function of hoof curvature (Quarters region)	0.01322	0.4919

Table 3.1: Linear regression models for the relationship between dorsal wall curvature and thickness. For each graph plotted in Fig3.3 this table provides the goodness of fit (R^2) and the deviation from zero (P) values of the plot's linear trendlines.

No significant correlation was found in the toe region between dorsal wall thickness and hoof curvature (R^2= 0.06541 and *P*= 0.1322 in Table 3.1) or in the quarters (R^2= 0.01322 and *P*= 0.4919). Nor does there appear to be a significant correlation between hoof categorisation and dorsal wall thickness as a function of hoof curvature as presented in Fig 3.3.

3.2.3 Corium Volume

As the lamellae are an indicative physical characteristic in chronic laminitics, the volume of the corium was compared to the dorsal wall hoof curvature and the lamellar surface curvature of P3, presented in Fig 3.4. The corium volume was plotted as a function of both hoof and bone curvature using colour coding to categorise the data as shown in Fig 3.2.

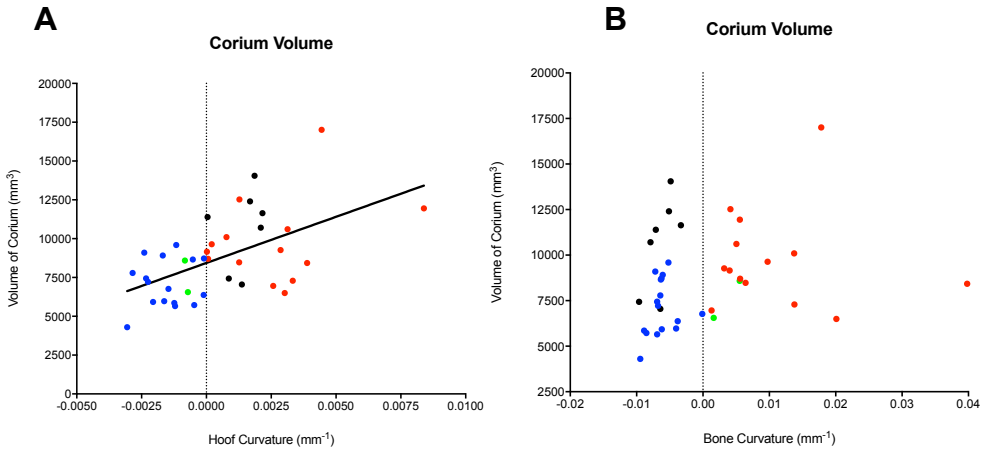


Figure 3.4: Corium volume as a function of dorsal wall and third phalanx curvature. **(A)** Corium volume as a function of dorsal hoof wall curvature with categorised data**. (B)** Corium volume as a function of third phalanx curvature with categorised data. ***n***=39.

The corium volume with respect to the dorsal hoof wall curvature showed some correlation, suggesting the corium volume is greater as the hoof curvature increases, shown in Fig 3.4A. With respect to the curvature of the pedal bone dorsal surface, the corium volume showed minimal variation, presented in Fig 3.4B. The categorisation of the data

points also supports the evidence that feet with a more positively curved dorsal hoof wall show greater remodelling of the corium.

	Goodness of Fit (R^2)	**Deviation From Zero (P)**
Corium volume as a function of hoof curvature	0.2929	0.0004

Table 3.2: The linear regression model for the relationship between corium volume and dorsal wall curvature. For the graph plotted in Fig. 3.4 this table provides the goodness of fit (R^2) and the deviation from zero (P) values of the plot's linear trendline.

The volume of corium as a function of dorsal hoof wall curvature has an R^2 value of 0.2929 and a P-value of 0.004 displaying a poor trend (R^2= 0.2929) but with a significant deviation from zero (P= 0.0004).

3.3 Bone

3.3.1 Bone Rendered μ-CT Images

To visibly analyse the bones of the equine foot, the binary CT images were segregated using a threshold value and entered into the Fiji ImageJ plugin, Volume Viewer. Volume viewer allows 3D reconstruction of the bones from the volumetrically rendered images.

The three bones of the equine foot were reconstructed in 3D, together and individually. The bones and their respective positions to one another were evident and the cortical bone surface could be viewed in fine detail (Fig 3.5). The reconstruction of the individual bones allowed the surface of P2 (Fig 3.6), P3 (Fig 3.7) and the navicular bone (Fig 3.8) to be viewed from different angles by rotating the 3D reconstructed image. Cross sections of ROI's were also constructed showing sections and the porosity of both cortical and trabecular bone. With a resolution of 120μm, a section of bone from P3 showing trabecular bone was produced from a laboratory μ-CT (Fig 3.9).

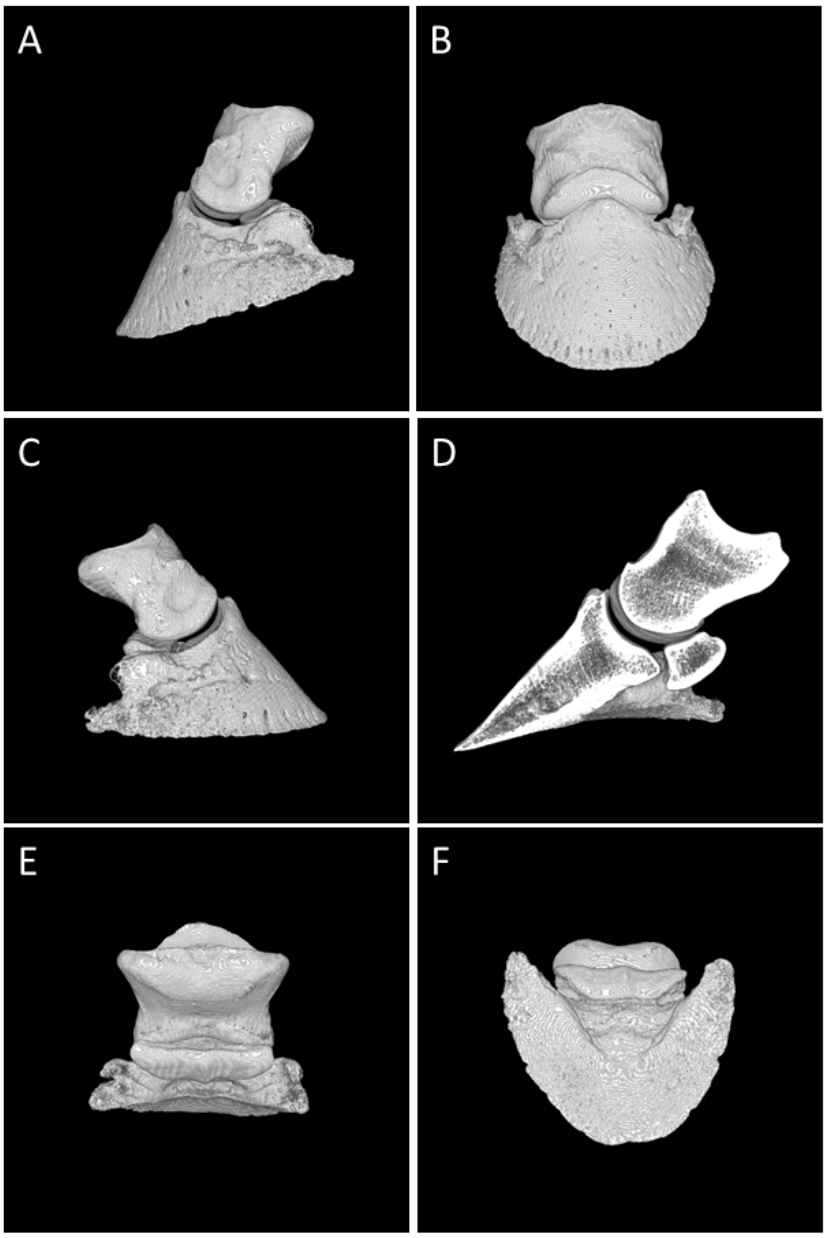


Figure 3.5: Bones of the equine foot. A 3D reconstruction of the μ-CT images showing the three bones of the equine foot. **(A)** Latero-medial, **(B)** cranial, **(C)** medio-lateral, **(D)** sagittal section, **(E)** caudal and **(F)** ventral. Resolution = 120μm (images courtesy of Emily Katy Paul).

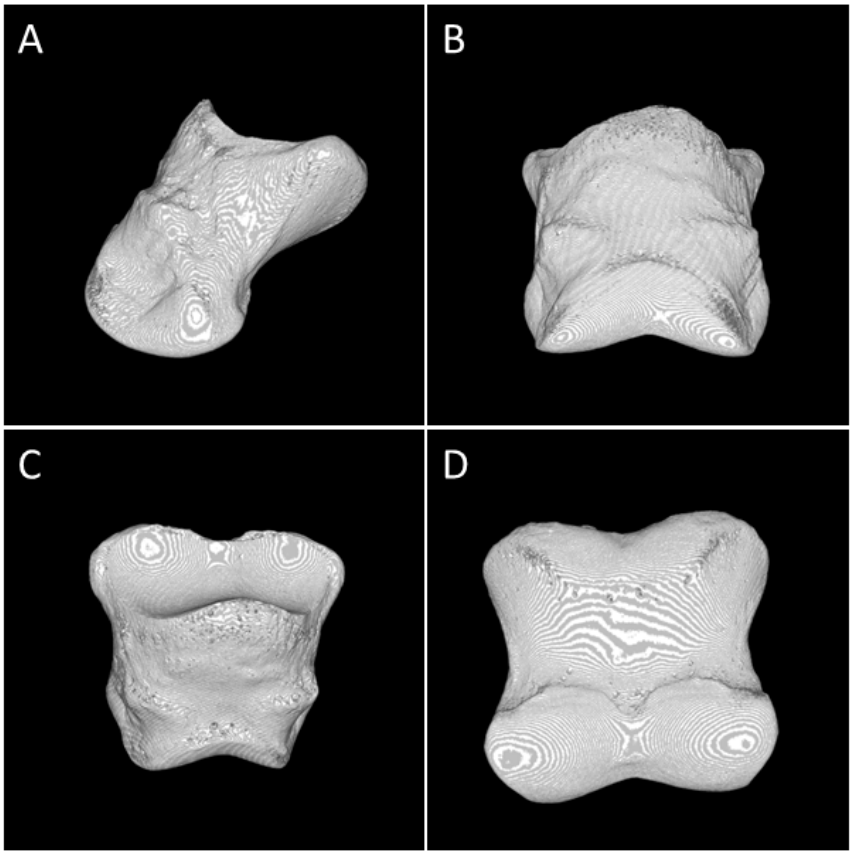


Figure 3.6: Second phalanx of the equine foot. µ-CT images reconstructed to show a 3D view of P2. (A) Latero-medial, (B) cranial (C) dorso-cranial and (D) caudal. Resolution= 120µm (images courtesy of Emily Katy Paul).

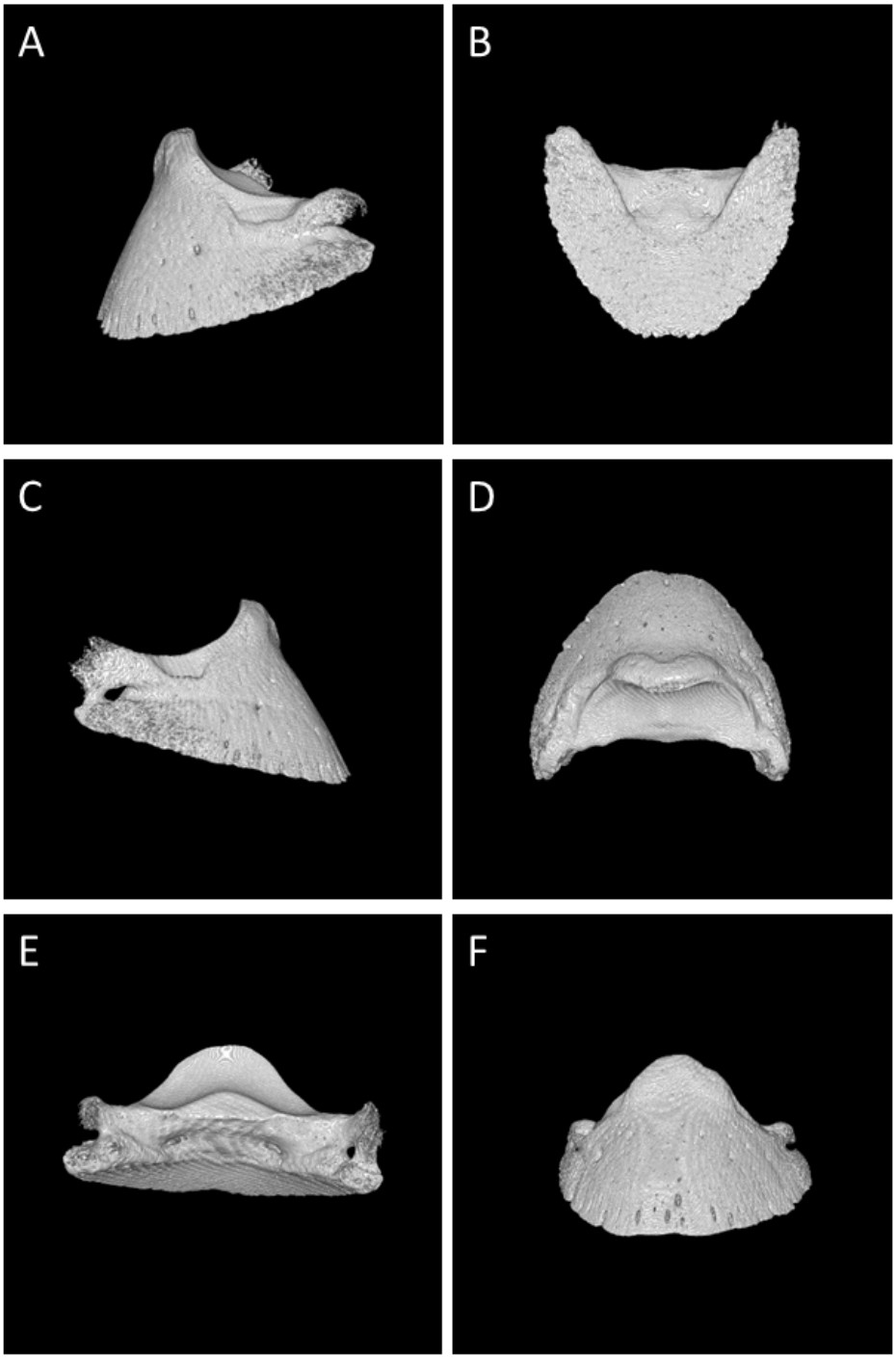


Figure 3.7: Third phalanx of the equine foot. µ-CT images reconstructed to show a 3D view of P3. **(A)** Latero-medial, **(B)** ventral, **(C)** medio-lateral, **(D)** dorsal, **(E)** caudal and **(F)** cranial. Resolution= 120µm (images courtesy of Emily Katy Paul).

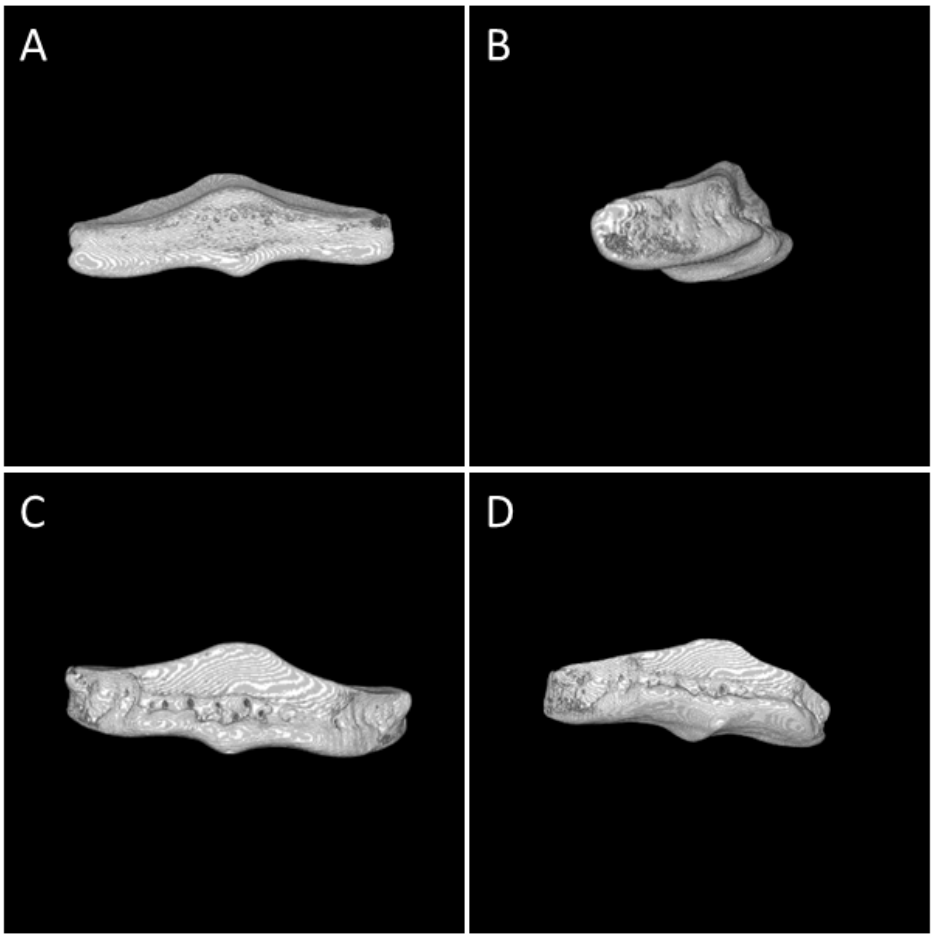


Figure 3.8: Navicular bone of the equine foot. µ-CT images reconstructed to show a 3D view of the navicular bone. **(A)** Caudal, **(B)** latero-medial, **(C)** cranial and **(D)** disto-caudal. Resolution= 120 µm (images courtesy of Emily Katy Paul).

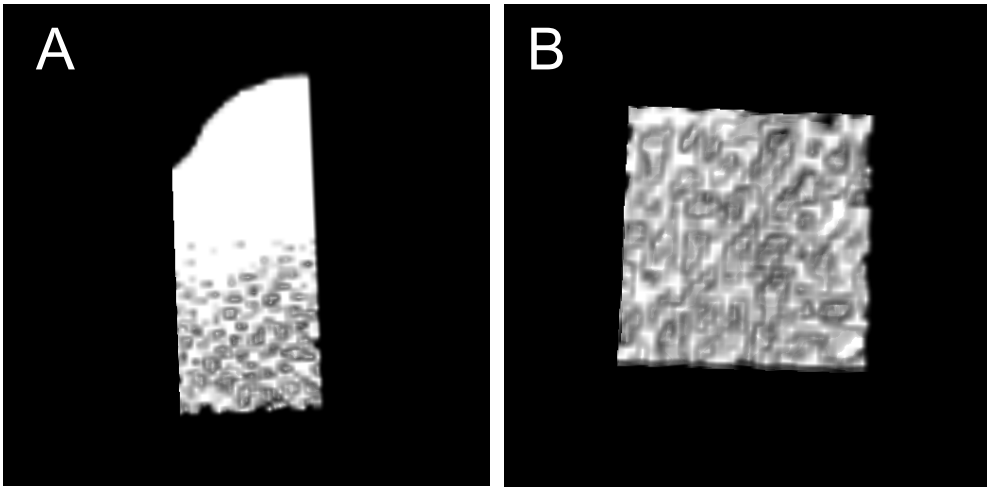


Figure 3.9: Trabecular bone section from the third phalanx of the equine foot. (A) A section of P3 showing cortical and trabecular bone. **(B)** A section of trabecular bone. Laboratory μ-CT images. Resolution= 120μm. Images copyright to the author.

3.3.2 Bone Curvature

The curvature of the dorsal aspects of P3 and the dorsal surface of the hoof wall show a positive linear correlation, as presented in Fig 3.10. The colour coding shows the distribution of the different categories of equine feet.

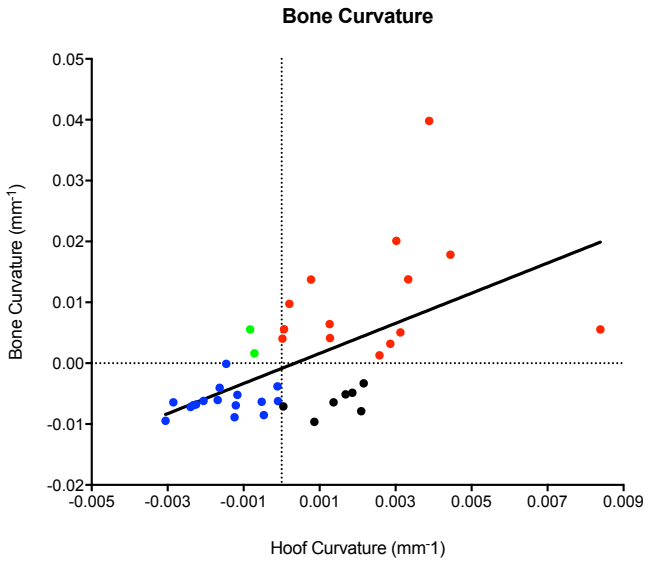


Figure 3.10: Bone curvature as a function of dorsal hoof wall curvature. The data has been categorised using the same method as in figure 3.2. *n*=39.

Bone curvature as a function of hoof curvature displayed a poor correlation (R^2= 0.3293) but a significant deviation from zero (P= 0.0001),

	Goodness of Fit (R^2)	**Deviation From Zero (*P*)**
Pedal bone curvature as a function of dorsal hoof wall curvature	0.3293	0.0001

Table 3.3: The linear regression model for pedal bone curvature as a function of dorsal hoof wall curvature. The table provides the goodness of fit (R^2) and the deviation from zero (*P*) values of the graph in Figure 3.10.

3.3.3 Cortical Bone Thickness

The relative cortical bone thickness at different ROIs were measured and related to the dorsal hoof wall curvature. The relevant graphical categorised results are displayed in Fig 3.11 and Fig 3.12 and the linear progression analyses are presented in Table 3.3. The ROIs were selected to highlight any significant differences between the different regions, dorsally and ventrally (Fig 3.11A, B and H), distally and proximally (Fig 3.11C and D) and against the whole bone thickness of P3 (Fig 3.11E, F and G).

Figure 3.12 shows the same data as in Figure 3.11 but the cortical thickness was plotted as a function of the hoof and bone curvature categories. This showed the distribution of cortical thickness amongst the four different categories allowing further comparison of the data.

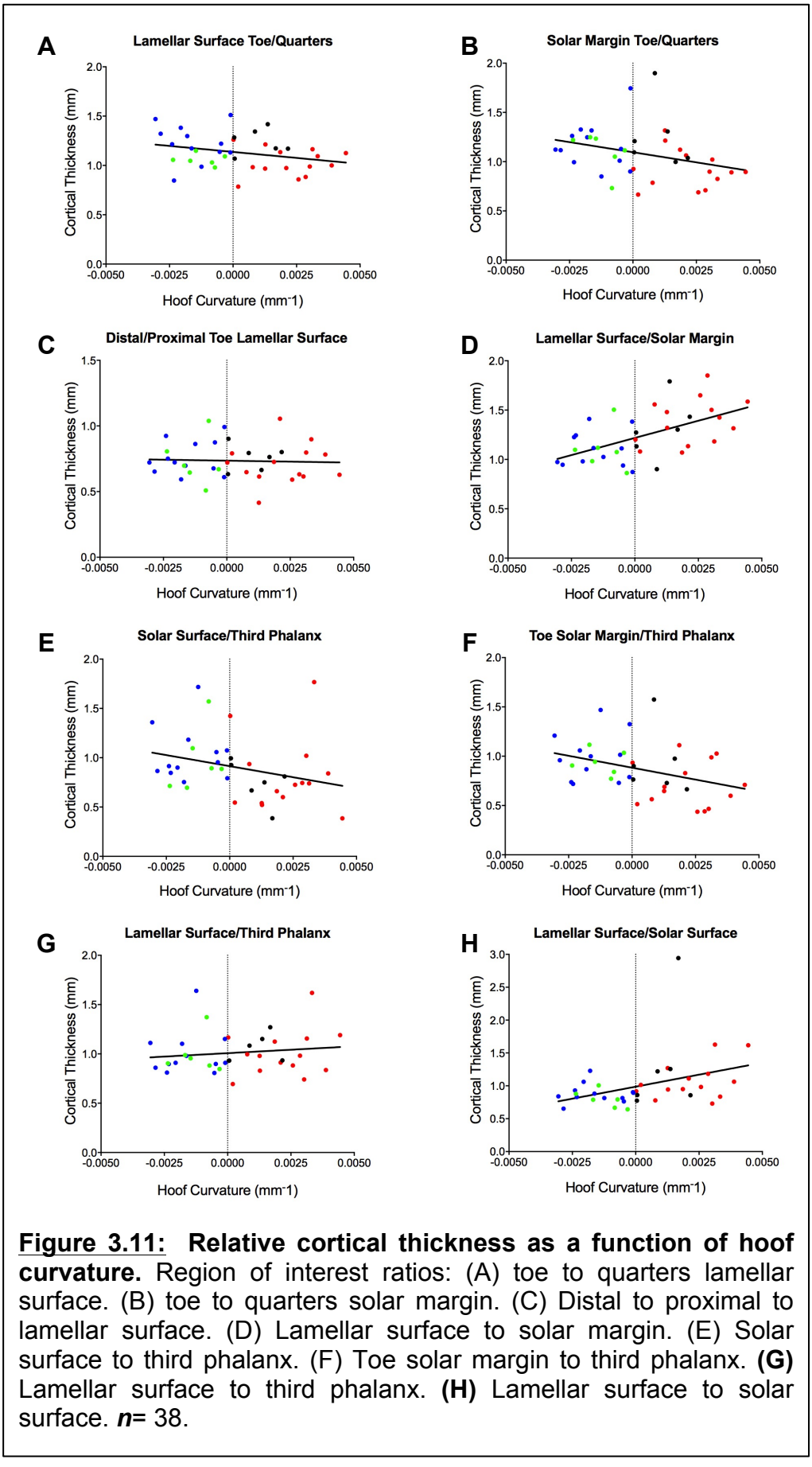


Figure 3.11: Relative cortical thickness as a function of hoof curvature. Region of interest ratios: (A) toe to quarters lamellar surface. (B) toe to quarters solar margin. (C) Distal to proximal to lamellar surface. (D) Lamellar surface to solar margin. (E) Solar surface to third phalanx. (F) Toe solar margin to third phalanx. **(G)** Lamellar surface to third phalanx. **(H)** Lamellar surface to solar surface. ***n*= 38.**

	Goodness of Fit (R^2)	Deviation From Zero (P)
A – Lamellar surface toe/quarters cortical thickness ratio as a function of hoof curvature	0.08079	0.0837
B – Solar margin toe/quarters cortical thickness ratio as a function of hoof curvature	0.1026	0.0499
C – Distal/proximal toe lamellar surface cortical thickness ratio as a function of hoof curvature	0.001827	0.7989
D – Lamellar surface/solar margin cortical thickness ratio as a function of hoof curvature	0.3052	0.0003
E – Solar surface/third phalanx cortical thickness ratio as a function of hoof curvature	0.07768	0.0902

F – Toe solar margin/third phalanx cortical thickness ratio as a function of hoof curvature	0.1376	0.0218
G – Lamellar surface/third phalanx cortical thickness ratio as a function of hoof curvature	0.01811	0.4206
H –Lamellar surface/solar surface cortical thickness ratio as a function of hoof curvature	0.1394	0.0210

Table 3.4: The linear regression models for relative cortical thickness as a function of dorsal hoof curvature. For each graph plotted in Fig 3.11 this table provides the goodness of fit (R^2) and the deviation from zero (P) values of the plot's linear trendlines.

The cortical thickness ratio between the toe and quarters of the lamellar surface was plotted (shown in Fig 3.11A) as a function of dorsal hoof wall curvature. Although the cortical thickness may appear to decrease slightly with respect to the quarters, as the dorsal hoof wall curvature increases, the trend is poor (R^2= 0.08079) with insignificant deviation from zero (P= 0.0837).

Figure 3.11B displays the ratio between the cortical thickness of the solar margin at the toe and quarters as a function of dorsal hoof wall curvature. The slight decrease in gradient of the trendline has a poor trend (R^2=0.1026) with an insignificant deviation from zero (0.0499).

The distal to proximal toe lamellar surface cortical thickness ratio was shown in Figure 3.11C. The decrease in distal toe lamellar surface thickness was very small and the gradient of the trendline was almost equal to zero. The trend was poor (R^2= 0.001827) and the deviation from zero was insignificant (*P*= 0.7989).

Figure 3.11D examines the cortical thickness ratio of the lamellar surface and the solar margin. The correlation (R^2= 0.3052) between dorsal hoof wall curvature and the cortical thickness ratio between the lamellar surface and solar margin was found to increase and deviate from zero significantly (*P*= 0.0003).

As demonstrated by Figure 3.11E, the cortical thickness ratio between the solar surface and the third phalanx was plotted. There was a decline in the solar surface thickness as the dorsal hoof wall curvature increases, however the correlation was poor (R^2= 0.07768) and the deviation from zero was also insignificant (*P*= 0.0902).

A poor trend (R^2= 0.1376) and a significant deviation from zero (*P*=0.0218) were shown in Figure 3.11F where the cortical thickness ratio between the solar margin and third phalanx was plotted as a function of dorsal hoof wall curvature.

The ratio of lamellar surface to the third phalanx cortical thickness as a function of dorsal hoof curvature was presented in Figure 3.11G. Both the correlation and deviation from zero were weak and insignificant (R^2= 0.01811 and *P*= 0.4206).

The lamellar surface was also compared as a ratio to the solar surface as shown in Figure 3.11H. The correlation was weak (R^2= 0.1394) and the deviation from zero was significant (*P*= 0.0210). There was a slight increase in lamellar surface thickness compared to the solar surface as the dorsal hoof wall curvature increases.

Bone thickness can be displayed visually by creating a bone thickness map from the relevant binary image stacks. The bone thickness of the individual feet in Figures 3.11 and 3.12 were reconstructed using the bone thickness function, where the bone thickness was mapped by tone of colour (see Figure 3.13 and 3.14).

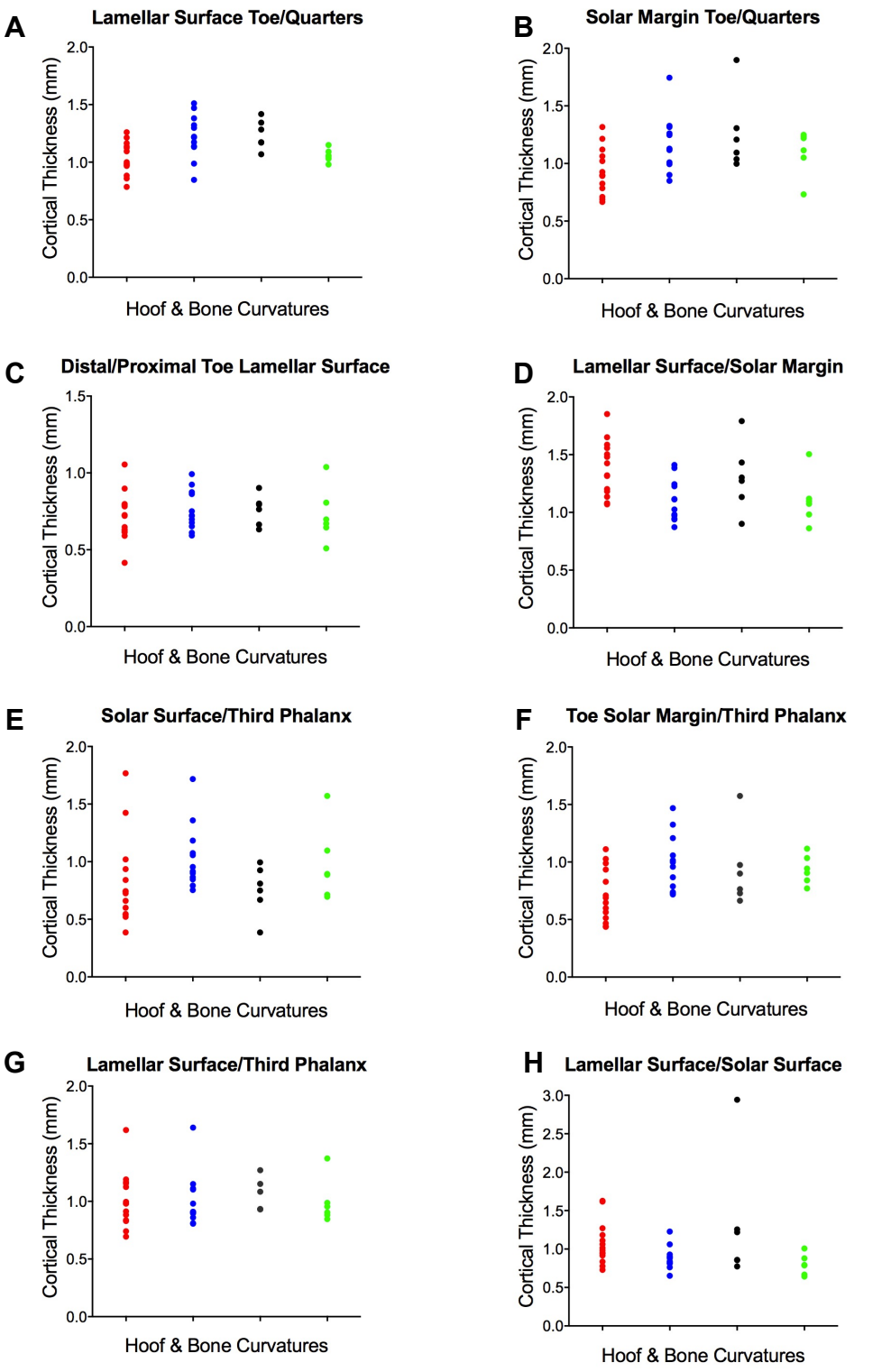


Figure 3.12: Relative cortical thickness of the third phalanx categorised using hoof and bone curvatures. Region of interest ratios: **(A)** toe quarters lamellae surface. **(B)** toe to quarters solar margin. **(C)** Distal to proximal to lamellar surface. **(D)** Lamellar surface to solar margin. **(E)** Solar surface to third phalanx. **(F)** Toe solar margin to third phalanx. **(G)** Lamellar surface to third phalanx. **(H)** Lamellar surface to solar surface. ***n***= 38**. Red (*n*)** = 14, **Blue *(n)*** = 12, **Black *(n)*** = 6 and **Green *(n)*** = 6.

In Figure 3.12A the equine feet that have a both positive dorsal hoof walls and P3 curvatures (red), and negative dorsal hoof walls and positive P3 curvatures (green) showed a distribution of data with smaller cortical thickness values. Suggesting the lamellar surface at the quarters is thicker in comparison to the other categories.

The distribution of data between the different categories in Figure 3.12B, C, G and H were fairly even, showing little variation and therefore no significant differences between them.

In comparison to the other categories, the equine feet with positive dorsal hoof walls and positive P3 curvatures (red) in Figure 3.12D have a greater distribution of points showing greater cortical thickness values. This suggests that the equine feet in this category have a thicker lamellar surface.

In Figure 3.12E the category of equine feet with positive dorsal hoof walls and a negative P3 curvatures (black) showed a distribution of data points with small cortical thickness values. The feet in this category therefore had a thicker P3 in comparison to the other categories. The equine feet with positive dorsal hoof walls and P3 curvatures (red) showed a similar distribution with the exception of two outliers. Those with negative dorsal hoof walls and positive P3 curvatures showed a large and varied distribution of points.

The toe solar margin was shown to have a greater corium thickness in the equine feet with negative dorsal hoof walls and negative P3 curvatures (blue), shown in Figure 3.12F. The other categories had a fairly even distribution to one another with the exception of an outlier in the category showing hoofs with positive dorsal walls and negative P3 curvatures (black).

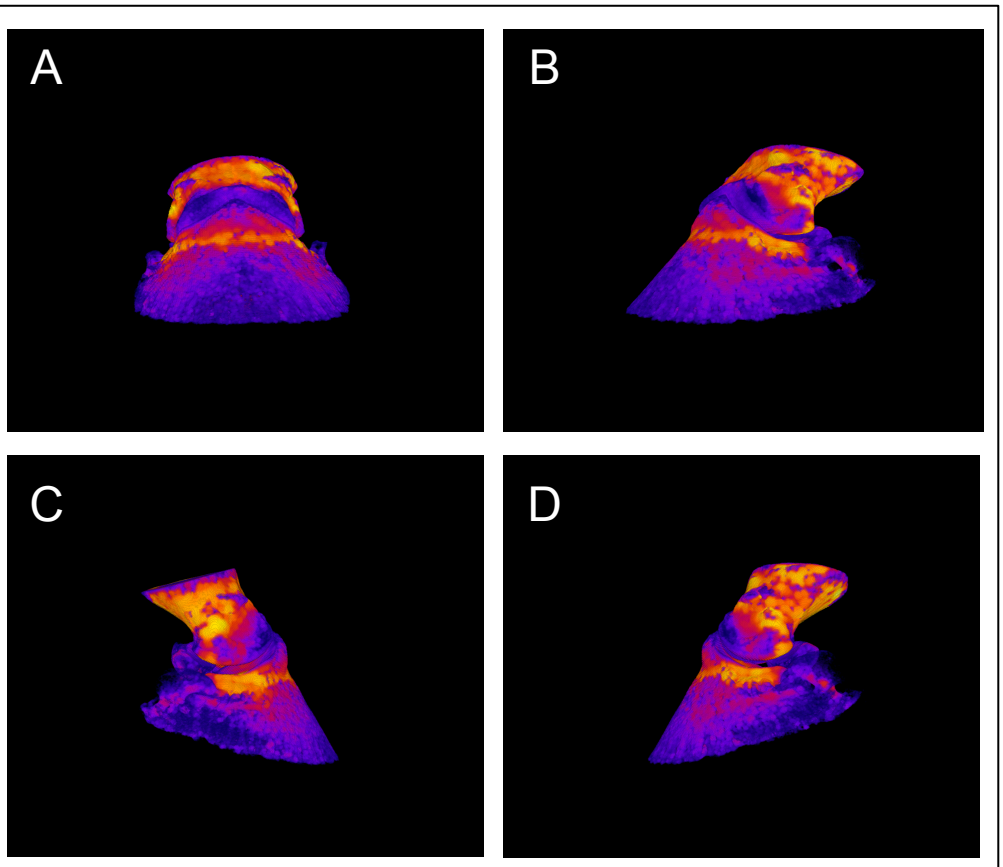


Figure 3.13: Bone thickness maps of the equine foot. 3D reconstruction of the equine foot using the thickness function of the BoneJ plugin. The bone thickness is mapped by the tone of colour, the brighter the colour the thicker the bone. **(A)** Cranial, **(B)** Oblique latero-medial, **(C)** medio-lateral and **(D)** latero-medial. Images copyright to the author.

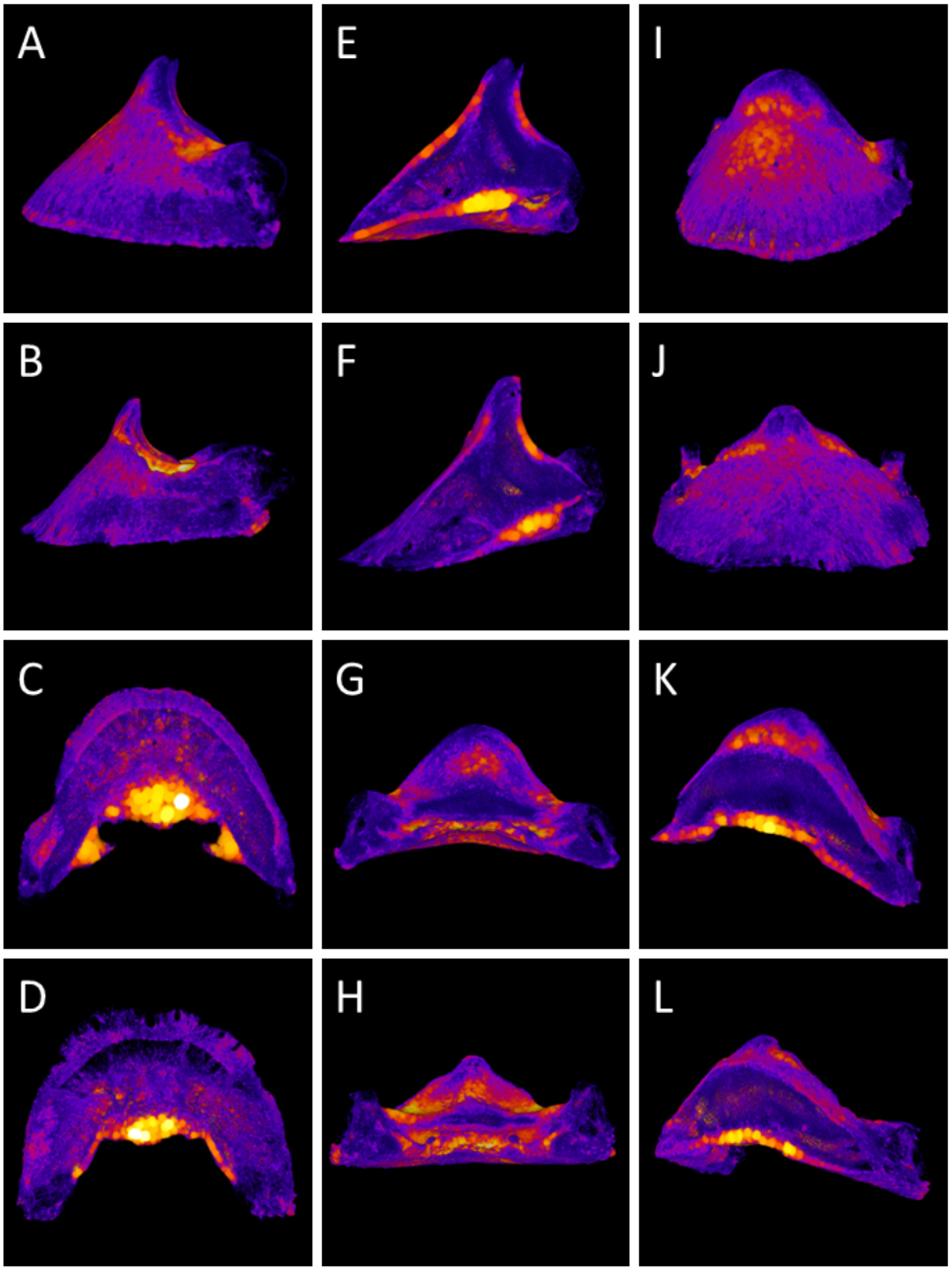


Figure 3.14: Bone thickness maps of the third phalanges. 3D reconstruction of the third phalanx using the BoneJ plugin thickness function. The function was applied to both a convex (negative) and concave (positive) curved third phalanx, allowing comparison between the two. **(A)** and **(B)** medio-lateral view, **(C)** and **(D)** distal/proximal section from the solar surface, **(E)** and **(F)** central saggittal sections, **(G)** and **(H)** caudo-cranial, **(I)** and **(J)** cranio-caudal and **(K)** and **(L)** oblique coronal sections passing through the flexor surface and up through the extensor process (images courtesy of Emily Katy Paul).

3.3.4 Trabecular Bone Anisotropy

Trabecular bone anisotropy was used to quantify the degree and volume of trabecular bone distortion in the third phalanx. The DA and VA were derived from the MIL. The VA was plotted as a function of hoof wall curvature (Fig 3.15A) and as a function of hoof and bone curvature (Fig 3.15B).

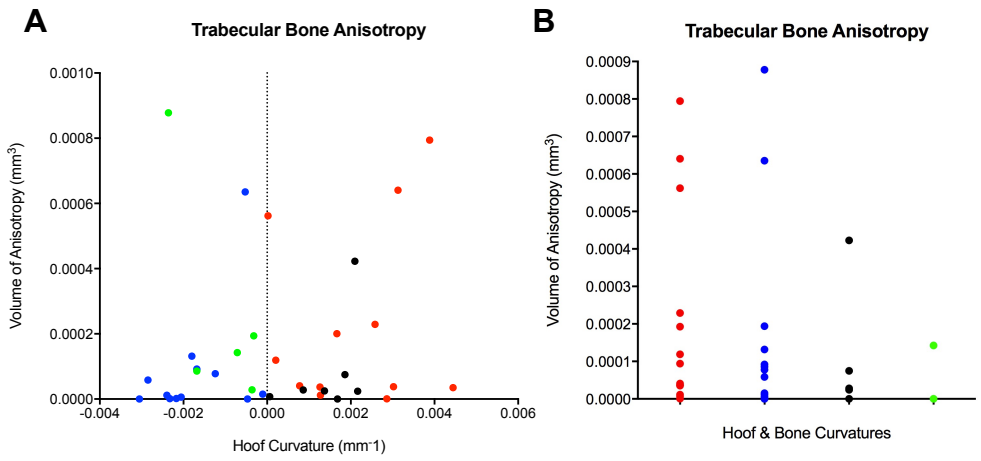


Figure 3.15: Trabecular bone anisotropy as a function of hoof curvature and categorised using hoof and bone curvatures. (A) Volume of trabecular bone anisotropy as a function of hoof curvature. **(B)** Hoof and bone curvature categories plotted against the volume of trabecular bone anisotropy. ***n***= 36. **Red (*n*)** = 14, **Blue (*n*)** = 14, **Black (*n*)** = 6 and **Green (*n*)** = 2.

In Figure 3.15A the VA was plotted as a function of dorsal hoof wall curvature. No correlation was identified between the volume of anisotropy and hoof curvature. The cloud plot graph in Figure 3.15B displays the VA as a function of hoof and bone curvatures (Fig 3.2). The distribution of VA between the different categories was relatively similar. It is difficult to make a valid comparison due to the variation in *n* numbers for each category.

3.4 Vasculature

3.4.1 Vasculature rendered μ-CT scan images

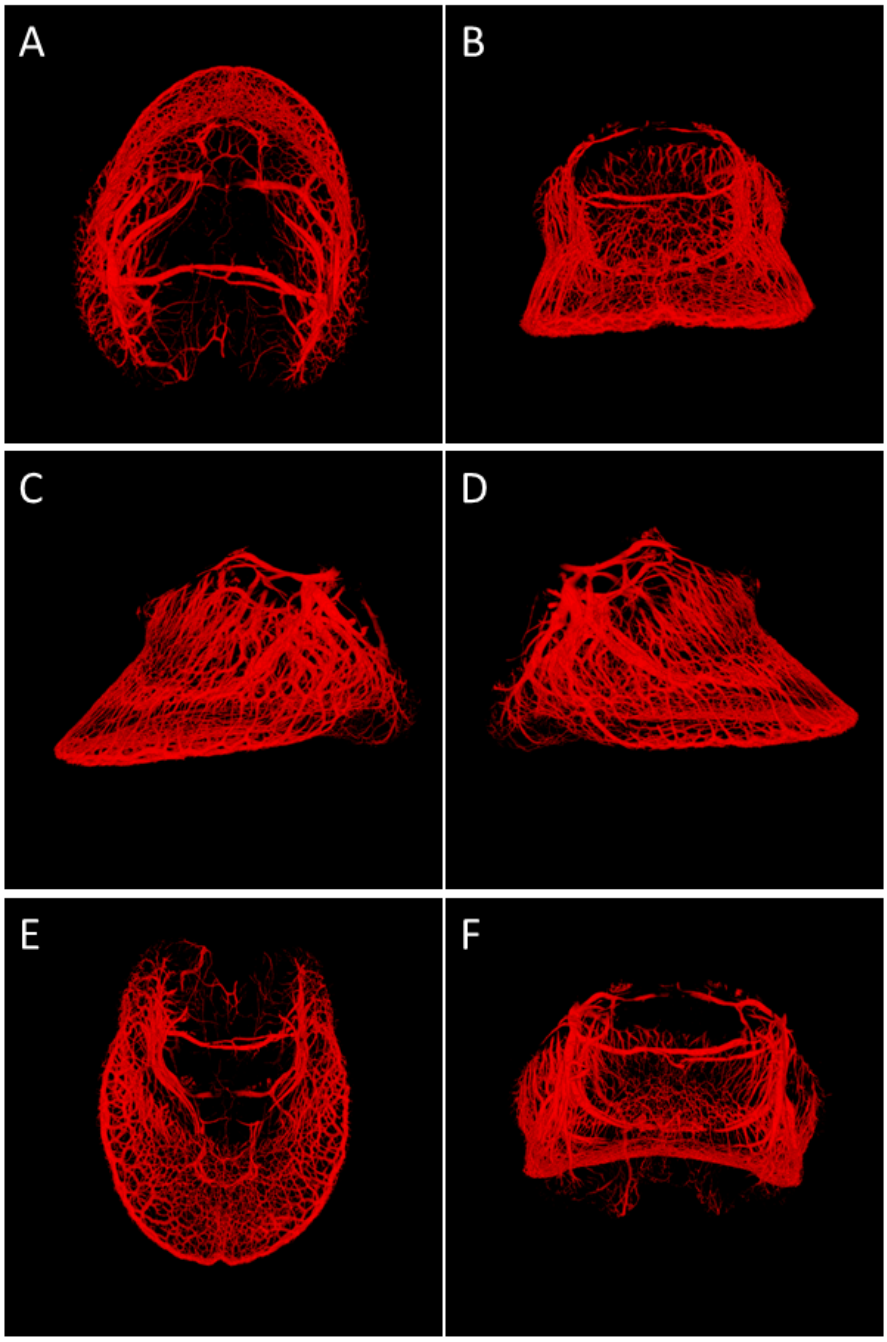


Figure 3.16: Vasculature of the equine foot. Volumetric 3D reconstructions of the vasculature of the equine foot. **(A)** Dorsal, **(B)** cranial, **(C)** lateral/medial, **(D)** medial/lateral, **(E)** ventral and **(F)** caudal. (Images courtesy of Emily Katy Paul).

The equine feet used for CT scanning were flushed and fixed with PFA (section 2.1). As the PFA diffused into the surrounding tissues the vasculature was left empty and air filled. The difference in attenuation of air within the vasculature in comparison to the surrounding tissues makes it the perfect contrast medium for vasculature analysis.

A 3D volumetric reconstruction of the vasculature was permitted as a result of the difference in attenuation, allowing the vasculature to be distinguishable (Fig 3.16). The full extent of the vasculature in the equine foot is shown, giving a good representation of the anatomical locations of the important blood vessels. For instance the medial/lateral digital arteries and veins, the solar circumflex vessels, sub-lamellar plexus, coronary circumflex vessels and the abundant heel vasculature are all visible. The resolution of the μ-CT images only permits the blood vessels equal to or greater than 120μm to be visible. As a result of the resolution, the microvasculature of the equine foot is not visible.

3.4.2 Vasculature Branches

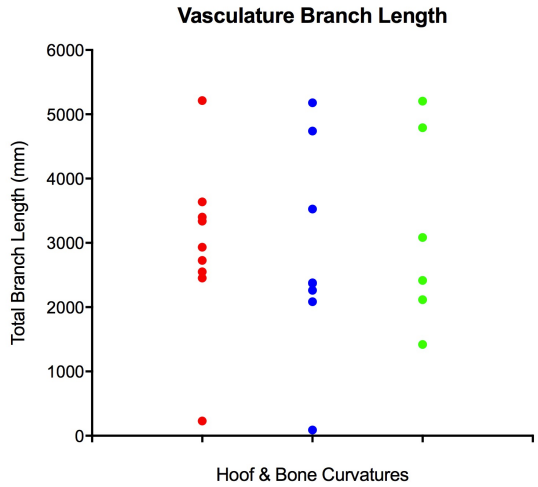


Figure 3.16: Total toe tip branch length categorised using hoof & pedal bone curvatures. Total branch length was plotted using the dorsal hoof wall and third phalanx curvatures to display the distribution of total vasculature branch lengths in the toe tip region for each hoof. ***n***= 23. **Red (*n*)**= 9, **Blue (*n*)**= 8, **Black (*n*)**= 0 and **Green (*n*)** = 6.

Vasculature branch length as a function of dorsal hoof wall and P3 curvature was plotted shown in Figure 3.16. Each category was plotted as a cloud graph to show the variation in total branch length. There were no equine feet with a positive dorsal hoof wall and negative P3 curvature (Fig 3.2 black) for vasculature analysis, due to poor perfusion of the vasculature in these feet. The variation in data between the categories was similar, suggesting that there are little differences in total vasculature branch length.

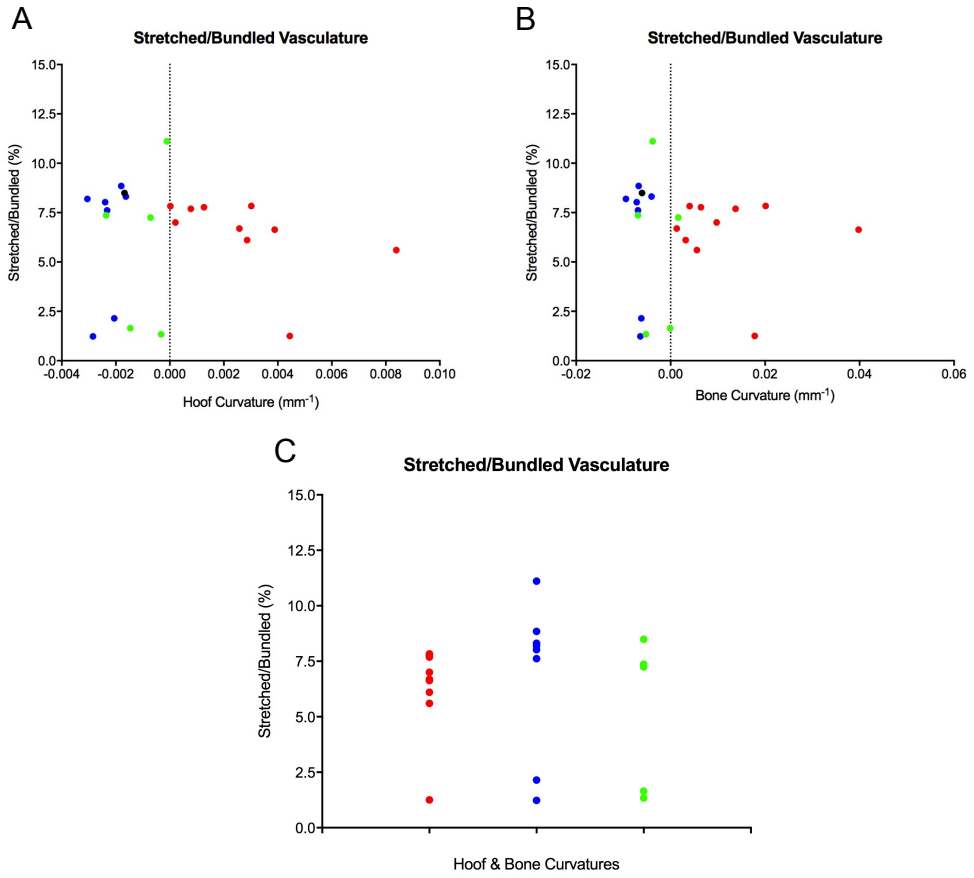


Figure 3.17: The percentage of stretched/bundled vessels. (A) Stretched/bundled vasculature percentage as a function of dorsal hoof wall curvature. **(B)** Stretched/bundled vasculature percentage as a function of third phalanx curvature. **(C)** Stretched/bundled vasculature percentage categorised using dorsal hoof wall and third phalanx curvatures. ***n***= 22. **Red (*n*)**= 10, **Blue (*n*)**= 8, **Black (*n*)**= 0 and **Green (*n*)**= 5.

Figures 3.17A and B show the percentage of stretched/bundled vessels as a function of dorsal hoof wall curvature and P3 curvature. The percentage of stretched/bundled vessels was calculated using the total branch length and the Euclidean distance. There was no significant correlation in the graphs plotted in Figure 3.17A and B, as a result a cloud graph was plotted showing the data in individual categories with the exception of equine feet with a positive hoof curvature and negative P3 curvature (Fig 3.2 black). In equine feet with a negative hoof wall and P3 curvature there was a greater number of stretched vessels.

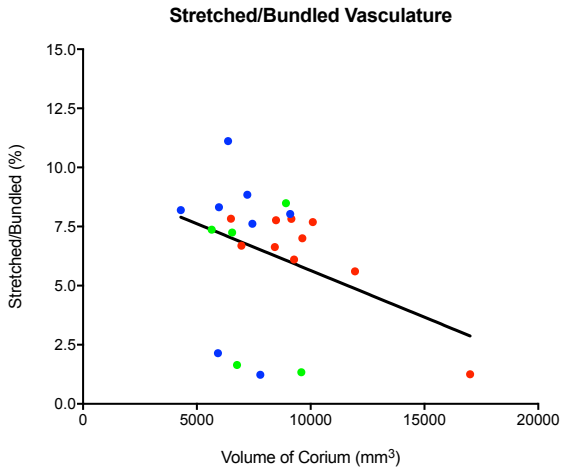


Figure 3.18: The percentage of stretched/bundled vasculature as a function of corium volume. The vasculature percentage of stretch/bundled branches was plotted as a function of the corium volume. ***n***= 23. **Red (*n*)**= 10, **Blue (*n*)**= 8, **Black (*n*)**= 0 and **Green (*n*)**= 5.

	Goodness of Fit (R^2)	**Deviation From Zero (*P*)**
The percentage of stretched/bundled vessels as a function of corium volume	0.134	0.0859

Table 3.5: The linear regression models for the percentage of stretched/bundled vessels as a function of the corium volume. For the graph plotted in figure 3.18 the goodness of fit (R^2) and deviation from zero (*P*) has been calculated.

A weak correlation for the percentage of stretched/bundled vessels as a function of corium volume was shown in Figure 3.18 and Table 3.5 (R^2= 0.134) and the deviation from zero was insignificant (P= 0.0859). This suggests that the corium volume and the conformation of the vasculature showed no correlation or trend as a function of one another.

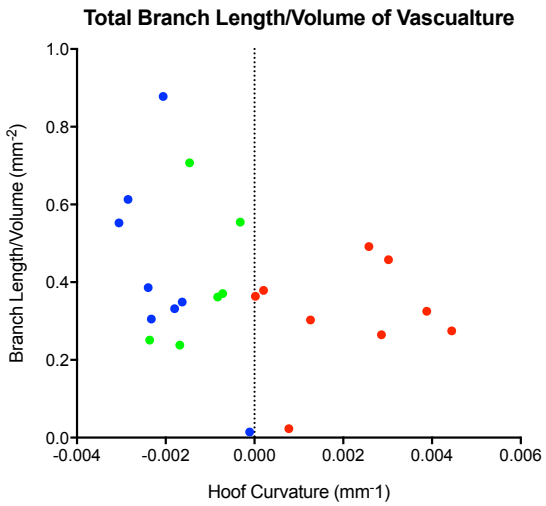


Figure 3. 19: Total branch length/volume of vasculature as a function of hoof curvature. The total branch length was divided by the volume of the vasculature as a function of the hoof curvature. The points were categorised using dorsal hoof wall and third phalanx curvatures. ***n***= 23. **Red (*n*)**= 9, **Blue (*n*)**= 8, **Black (*n*)**= 0 and **Green (*n*)**= 6.

The graph in Figure 3.19 was plotted to show the relationship between branch length and vasculature volume with respect to the dorsal hoof wall curvature. Each equine foot was colour coded to represent the different categories of the equine feet with respect to the curvatures of both the dorsal hoof wall and P3 (Fig. 3.2). Those with a more negatively curved dorsal hoof wall showed an increase in the distribution of data and the vasculature branch length compared to the vasculature volume respectively.

3.4.3 Lumen Diameter

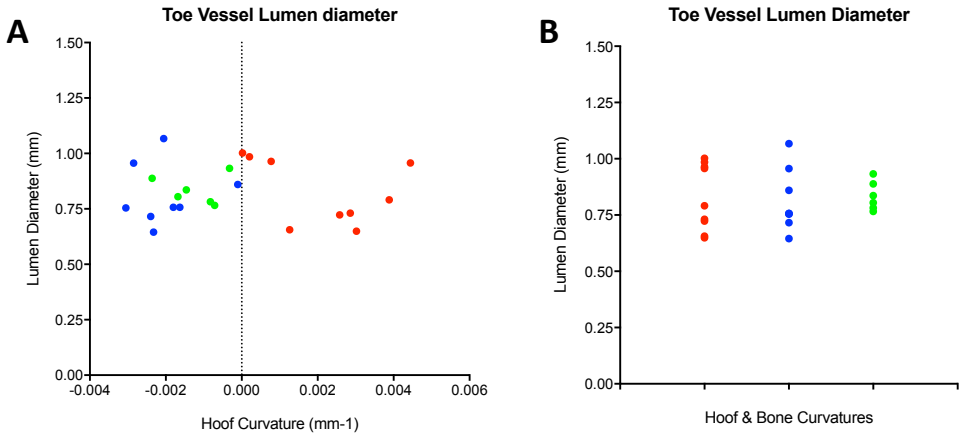


Figure 3.20: The lumen diameter of blood vessels as a function of hoof and third phalanx curvatures. **(A)** The mean lumen diameter of blood vessels in the toe tip region as a function of dorsal hoof wall curvature. **(B)** The mean lumen diameter of blood vessels in the toe tip region categorised using the hoof and third phalanx curvatures. ***n***= 23. **Red (n)**= 9, **Blue (n)**= 8 and **Green (n)**= 6.

The toe vessel lumen diameter is an indicator of vasodilation and blood circulation to the distal end of the hoof capsule. In Figure 3.20A the lumen diameter was plotted as a function of dorsal hoof wall curvature. Figure 3.20B shows the lumen diameter of the blood vessels as a function of hoof and bone curvatures. All of the data points are colour coded with reference to Figure 3.2. Figure 3.20A showed no correlation between the data. The cloud plot graph in Figure 3.20B displays the distribution of data points in three of the four categories. Equine feet with a convex hoof wall and a concave P3 showed a tighter grouping and therefore less varied data points. However among the three sets of data there was little variation among the groupings.

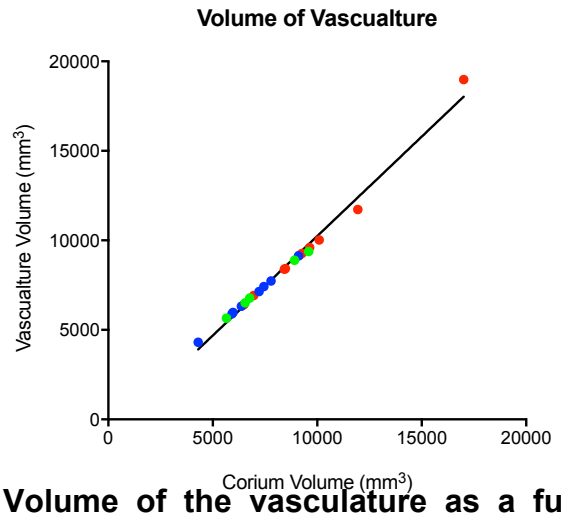


Figure 3.21: Volume of the vasculature as a function of the corium volume at the toe tip. The volume of the vasculature at the toe tip was plotted against the dorsal toe corium volume. The data was categorised using the dorsal hoof wall and third phalanx curvatures. ***n***= 23. **Red (*n*)**= 10, **Blue (*n*)**= 8 and **Green (*n*)**= 5.

	Goodness of Fit (R^2)	**Deviation From Zero (*P*)**
The volume of vasculature branches as a function of the corium volume	0.9884	<0.0001

Table 3.6: Models of linear regression for the vasculature volume as a function of the corium volume. The goodness of fit (R^2) and the deviation from zero (*P*) has been calculated for the linear trendline plotted in Figure 3.21.

The vasculature volume and corium volume in the dorsal toe region were plotted as a function of one another (Figure 3.21) to compare the density of the vasculature within the corium and dorsal toe region. The linear regression models in Table 3.6 showed a strong correlation (R^2= 0.9884) and a significant deviation from zero (P= <0.001).

3.4.4 Software Development For Vasculature Isolation

A macro for vasculature isolation was adapted and used for each equine foot μ-CT scan. Figure 3.21 shows the script written in ijm format for use with Fiji ImageJ. The file names, image numbers and document pathways were all adapted and changed as required.

```
run("Image Sequence...", "open=[G:\\CT-SCAN IMAGES 2014\\M0867 -2\\2_aligned\\YZ\\2-a-YZ_0000.tif] number=855 starting=450 sort");
run("Rotate... ", "angle=180 grid=1 interpolation=Bilinear stack");
run("Properties...", "channels=1 slices=855 frames=1 unit=1 pixel_width=1 pixel_height=1 voxel_depth=1"); // re scale in pixel dim
n=nSlices;
setSlice(n/2);
setOption("BlackBackground", true);
run("Convert to Mask", "method=IJ_IsoData background=Dark black");
run("Duplicate...", "title=Hoof_2-1 duplicate range=1-855");
run("Fill Holes", "stack");
run("Remove Outliers...", "radius=10 threshold=50 which=Bright stack");
run("Remove Outliers...", "radius=2 threshold=50 which=Dark stack");
run("Erode", "stack");
run("Erode", "stack");
run("Erode", "stack");
run("Erode", "stack");
selectWindow("YZ");
run("Invert", "stack");
run("Remove Outliers...", "radius=2 threshold=50 which=Dark stack");
imageCalculator("Multiply create stack", "YZ","Hoof_2-1");
run("Remove Outliers...", "radius=0.5 threshold=50 which=Bright stack");
run("Image Sequence... ", "format=TIFF name=H2_YZ_V save=[G:\\CT-SCAN IMAGES 2014\\M0867 -2\\Blood_Vessels\\Full\\H2_YZ_V0000.tif]");
run("Close");
run("Close");
run("Close");
```

Figure 3.22: Macro for vasculature isolation. The macro used for Fiji Image J for the creation of blood vessel isolation from tomograms using binary image stacks. (Software developed by Emily Paul. Software used and altered by author for each image stack).

4 Discussion

Foot lameness in equids is highly prevalent and the most common cause of equine euthanasia, having great economic and welfare impacts (Ireland *et al.*, 2011). Foot pathologies associated with the lamellae, commonly known as 'laminitis' are of particular concern. In order to gain a sufficient understanding of the equine foot and its pathological adaptations associated with laminitis, a sufficient understanding of its anatomical structures in a normal state must be investigated. Thus a novel technique was employed with the utilisation of micro-computer tomography, with the aim of developing new methodologies for this research field.

4.2 Pathomorphological Features

The chronically laminitic foot has a number of pathomorphological features exhibited both externally and internally that can be investigated.

4.2.1 External Features

The external surface of the hoof capsule can display visual signs of pathomorphology, these include dorsal hoof wall concavity (positive dorsal hoof wall curvature) and solar flattening/increased thickness (Hunt and Wharton, 2010). Externally, cadaveric equine feet were studied to identify their morphological state. Dorsal hoof wall curvature was chosen as the primary physical descriptor due to its validity, accuracy and lack of subjectivity. Furthermore within the literature a dished equine foot is a renowned feature of a laminitic foot thus dorsal hoof wall curvature (Grosenbaugh & Morgan 1999; Parks & O'Grady 2003; Eustace 2010; Hunt & Wharton 2010; O'Grady 2010). Therefore justifying the use of hoof curvature as the comparative physical descriptor and observing its correlation with the remaining variables.

4.2.2 Internal Features

Within the hoof capsule the physical descriptors of importance are P3, blood vessels, the hoof wall and the corium. In the chronic laminitic a diagnostic pathological feature is the sinking/rotation of the third phalanx with respect to the hoof capsule and the other phalanges, in particular P2 (Parks and O'Grady, 2003). The rotation/sinking of P3 is unveiled radiographically; diagnosis of this involves calculating the angle of rotation of P3 with respect to the surrounding anatomical features. The angle between the dorsal hoof wall and the dorsal surface of P3 and that between the solar surface of P3 and the ground are examples of this, however this has been calculated previously so isn't discussed further in this study (Floyd and Mansmann, 2007).

Externally the dorsal hoof wall curvature was calculated using the mid-sagittal slice, as aforementioned the curvature of the dorsal surface was used as the primary comparative physical descriptor. The relationship between the dorsal curvature and hoof wall thickness at the toe and quarters was not significant. The average thickness at the quarters was thicker than at the toe contrary to the literature, where the quarters region was thinner an described as being more flexible (Douglas *et al.*, 1996). This is probably a result of differences in experimental design. In this study the thickness was calculated by measuring along the entire dorsal surface at both the toe and quarters, taking an average of the measurements at the different intersections. Secondly samples were not taken from one location, the entire surface was measured and the orientation at which the thickness was measured may have also differed. The extent of thickening could have been dampened from heel trimming, as a measure to manage laminitics and correct P3 displacement in feet with a laminitic history (O'Grady, 2010). Unfortunately the history of the feet was unknown so this could not be assessed or taken into account. Data of sole thickness was not included in the study but should be investigated in feet with a known clinical history. According to the literature the sole surface concavity is

reduced in chronic laminitics, flattening the solar surface and consequentially weakening and thinning the sole, yet if the hoof becomes overgrown the sole can become grossly thickened (Parks and O'Grady, 2003; Hunt and Wharton, 2010).

The corium volume was calculated using all slices containing both the corium and P3 in the toe region. No significance between corium volume and dorsal hoof curvature was identified. This was a novel calculation and should be further investigated in feet with a known clinical history. Furthermore angiography has been used in the literature to assess the corium vasculature. It was found that the corium of laminitics had an irregular vascular pattern and in some locations was avascular (Ackerman *et al.*, 1975). Perhaps with further investigation the corium volume would differ between normal and laminitic feet.

4.3 Bone Remodelling

As bone is a physiologically dynamic and highly adaptive tissue to its environment it can enable the pathophysiological status of the bone and surrounding tissues to be studied (Clarke, 2008). While a number of different factors/mechanisms control and initiate the bone remodelling process, the main focus of this study was to analyse the adaptability of osteoid tissue in terms of bone morphology; shape, cortical thickness and trabecular anisotropy, with respect to the surrounding anatomical elements of the hoof capsule. This will provide insight into biomechanical force imbalances and pathomorphological features of P3 within the equine foot.

From examining the data in section 3.3.2 it is clear that the majority of feet have a dorsal hoof wall curvature to which P3 adheres, with the odd exception. Applying this to the tissues of the equine foot it could be inferred that the distortion of one could lead to the application of sufficient mechanical forces being exerted on the surrounding

anatomical features causing their deformation. Therefore applying the principals of Wolff's law to the equine foot (Pearson and Lieberman, 2004; Nyary and Scammell, 2015). The graphical display of bone curvature as a function of hoof curvature is shown in Figure 3.10. There is a distinct lack of variation in the negative curvature values of P3 regardless of the dorsal hoof wall curvature, of which most are encapsulated in a hoof capsule with a negative dorsal wall. The presence of a convex P3 in a hoof with a concave dorsal wall is largely greater than that of a hoof with a convex dorsal wall and a concave P3. This could suggest that the convexity of P3 is in fact the norm. Feet with a concave P3 dorsal surface show a greater variability, in particular those encapsulated in a concave hoof. It could be implied that feet showing both a concave dorsal hoof wall and P3 dorsal surface is a result of mechanical strain and consequentially the remodelling of bone has occurred. The biomechanical force imbalances applied may have resulted in a concave dorsal hoof wall and therefore distortion of P3 or vice versa if the concavity of P3 is in fact the norm.

As aforementioned, biomechanical strains exerted on the hoof could lead to the distortion of an anatomical feature resulting in the deformation or remodelling of another (Bowker, 2003). As the corium lies directly between the hoof wall and pedal bone, it was of paramount importance to investigate any changes in corium volume as function of bone curvature. Interestingly equine feet with a negative hoof capsule, despite the curvature of P3 were shown to have a smaller corium volume and vice versa for feet with a positive hoof capsule. However the data for equine feet with a positive hoof wall and P3 dorsal surface was greatly varied, implying that perhaps once the mechanical strain limit had been exceeded there was detachment/unzipping of the corium, consequently the corium volume would be smaller as the mechanical strain has ceased and therefore remodelling of the tissue would be terminated (Pollitt, 2004b; Carter *et al.*, 2011). It would not be unreasonable to suggest that this could be the same for all feet with a positive hoof capsule due to the dynamic changes of the hoof wall

resulting in being pulled away from P3, causing sufficient strain to be exerted on both P3 and the corium. Hoofs with a concave hoof capsule and convex P3 may equally display the same results, as some variation is shown in corium volume, however samples of both normal and laminitic feet would be required to analyse this further. The feet showing a smaller corium volume were those with a negative hoof capsule, perhaps inferring that convex hoof capsules apply less strain and have a reduced volume between P3 and the dorsal hoof wall resulting in a smaller corium volume. To back this up further, the anomaly group consisting of equine feet with a convex hoof wall and concave P3, have a relatively straight dorsal hoof wall and subsequently there is a reduction in the biomechanical forces exerted. This needs to be investigated further with samples of feet with a known clinical history in order to fully understand the biomechanics.

In the normal state, bone remodelling should be balanced as a consequence of physiological and biomechanical equilibrium, where osteolysis and osteogenesis both occur at the same rate (Feng and McDonald, 2011). Depressed biomechanical stress can lead to bone resorption via osteoclastic osteolysis, reducing bone thickness. Conversely, elevated biomechanical stress can lead to osteoblastic osteogenesis that often coincides with osteoclastic suppression and hence an increase in bone thickness (Pearson and Lieberman, 2004). Accordingly the correlation in curvature of the dorsal surfaces of the hoof capsule and P3 could suggest the existence of inseparable biomechanical forces between them (Floyd and Mansmann, 2007). To back this up further cortical bone thickness in the different anatomical regions was plotted as a function of dorsal hoof wall curvature, to help in the identification of regions under mechanical strain or bone remodelling (Fig 3.14) (Pearson and Lieberman, 2004).

The cortical thickness ratios between the lamellar surface at the toe and quarters (Fig 3.11A), the solar margin at the toe and quarters (Fig 3.11B), the distal and proximal toe lamellar surfaces (Fig 3.11C), the

solar surface and third phalanx (Fig 3.11E) and the lamellar surface and third phalanx (Fig 3.11G) were insignificant.

The ratio between lamellar surface and solar margin as a function of hoof curvature exhibited a strong correlation and was significant (Fig 3.11D). The observations made from Figures 3.11D and 3.12D demonstrated that the cortical thickness of the lamellar surface increases in relation to that of the solar margin as the dorsal hoof wall curvature increases. The observation made could mean that the current belief of failing epidermal/dermal lamellar bonds is in fact misunderstood and requires further exploration. The results found in this study could propose that the brunt biomechanical forces are exerted on the parietal surface and not the solar margin. However due to the lack of clinical data it is hard to establish the exact pathological changes.

The toe solar margin and third phalanx ratio was also significant showing that as the dorsal hoof curvature increased the toe solar margin thickness decreased (Fig 3.11F and Fig 3.12F). As the toe solar margin sits on the toe-tip of the hoof capsule you would expect it to be thickened in feet with a negative hoof wall as a consequence of the increased contact with the ground in comparison to the dished hoof.

Lastly the lamellar surface was plotted as a ratio with the solar surface (Fig 3.11H and Fig 3.12H). The increase in convexity of the hoof capsule resulted in a thicker lamellar surface and a relatively thinner solar surface. As the hoof curvatures convexity increased the mechanical strain applied to the lamellar surface must be intensified, and lessened on the solar surface unless flattening of the sole has occurred. Unsurprisingly the solar margin thickness decreased in feet with a positive hoof capsule despite the narrow distribution in data. In chronic laminitics it is reported that visible fractures and thinning of the bone is seen (Morrison, 2010). In a recent study of osteopathology in laminitics, histopathology and μ-CT were used in the findings of

osteoclastic resorption and thinning of the distal phalanx in laminitics (Engiles *et al.*, 2015). The findings from the lamellar surface are interesting, as they appeared almost horizontal in nature, depicting that the cortical thickness remained fairly constant and unaffected in the differing feet.

Besides the changes in cortical bone thickness, gross shape and parietal curvature, trabecular bone may have also been affected by osseous remodelling. In this study trabecular bone anisotropy was used to quantify the degree and volume of trabecular bone distortion in the distal phalanx. As a function of hoof curvature, the VA was not significant. In a study on the volumetric decomposition of trabeculae and the morphologic corrections in human trabecular bone, samples were obtained from the femoral neck, proximal tibia and lumbar vertebral body (Liu *et al.*, 2007). It was found that the microarchitecture of all three sites differed dramatically, the presence of longitudinal plates was greater in the tibia and the presence of transverse rods was more abundant in the lumbar vertebral body. The observations are consistent with the expectation that the majority of trabecular plates would be orientated predominantly in the direction of loading. An example of this was trabecular rods in the lumbar vertebral body aligning with the transverse plane. Furthermore the pathophysiology of osteoporosis is known to cause thinning and weakening of osseous tissue as well as attributing an increased susceptibility to fractures, it has been reported that trabecular morphology dramatically changes from plate to rod-like trabeculae as a result of aging and osteoporosis (Liu *et al.*, 2007). With features of osteoporotic bone being a physiological trait in laminitic hoofs, it was of interest to this study to assess the volume of anisotropy in the toe tip region of the distal phalanx, with the assumption of this being the primary remodelling site.

The lack of anisotropy makes it difficult to identify the specific areas subject to mechanical strain, although alterations in cortical thickness helps to pinpoint the localised regions under sufficient strain resulting in

the pathomorphology of the distal phalanx. The trabecular analysis of the regions surrounding the toe-tip may be more indicative of the impact mechanical strain has on the trabeculae regarding distortion. From the results of cortical thickness, the areas of interest would be the solar margin, solar surface and the lamellar surface. Both the solar margin and solar surface underwent thinning as the concavity of the hoof capsule increased, however the solar surface did so to a lesser extent proposing that the locality of increased mechanical strain is implausible. The lamellar surface remained fairly consistent among the equine feet with differing hoof curvatures, and increased significantly with the increase in concavity of the dorsal hoof walls when compared to the solar margin, indicating that both the lamellar surface and solar margin could be regions subject to increase mechanical strain and therefore elevated trabecular distortion.

As the resilience of trabecular bone to tensile forces is lesser to that of compressive forces, as shown in bovine tibial bones, it would suggest that the observation of increased cortical bone thickness and trabecular pore size could be a result of the increase in tensile forces exerted from the lamellar surface within the hoof capsule (Keaveny *et al.*, 1994). Therefore the relative isotropic results shown would be consequentially plausible as the lamellae extend over the entire parietal surface of P3. Albeit the thickness of the lamellar surface remained unchanged as a ratio of the whole cortical thickness of P3 with augmenting dorsal concavity, this could be explained by the metabolic activity of cortical osteoid being significantly less than that of trabecular osteoid (Hadjidakis and Androulakis, 2006). Hence it could explain why a greater change was seen in trabecular bone than cortical bone.

4.4 Vascular remodelling

Laminitis has commonly been associated with vascular disturbances and is therefore one of the focal points in this study (Heymering, 2010).

Venography is a technique that has commonly been used to provide vasculature information in order to treat and monitor the progress of vasculature abnormalities (Rucker, 2010a). In this study μ-CT has been utilised to give higher levels of quantitative data which venography cannot provide, allowing the visualisation of the vasculature network in discrete regions and not being reliant on the rate of perfusion as result of the attenuation of a contrast medium.

A number of vascular properties were analysed these included vasculature branch length, the presence of stretched or bundled vessels, vasculature volume and lumen diameter. Vasculature branch length at the toe tip was plotted in the different hoof categories (Fig 3.16, method for categorisation shown in Section 3.2.1), however no equine feet with a positive dorsal hoof wall and negative dorsal P3 curvature were plotted due the poor perfusion of these feet. Therefore only 3 categories of equine feet were used for vasculature analysis. The variation between the differing categories with regards to branch length were minimal, showing similar distribution in data, suggesting that branch length remains unchanged with regards to the pathomorphological effects. The variability within each category is likely to be a reflection of hoof size and morphology. With respect to an increase in metabolic need for a greater vasculature supply, it would be expected that the remodelling of blood vessels would take place at a microvasculature level and consequently no changes to the macrovasculature could be seen which complies with the results found.

The total branch length and Euclidean distance were both used to categorise the vessels as being bundled or stretched at the toe tip. It was found that as the convexity of the dorsal hoof wall increased, the percentage of stretched vessels decreased and bundled vessels increased. Equally the same result was displayed for bone curvature. Both graphs show two distinct groups due to extremes of variability in the data, which can be clearly seen in the graph plotted as a function of

the categories (Fig 3.17C). For further clarification of these results, the percentage ratio of stretched to bundled vessels was plotted as a function of corium volume (Fig 3.18). The weak trend and an insignificant deviation from zero found could concur with the corium volume variability stated in Section 4.2.2 where an increase in dorsal hoof wall concavity could cause detachment of the corium and as a result shows a high level of variability. Furthermore the corium volume does appear to have a slight trend visually, indicating that there is a greater presence of bundled vessels where the corium volume is greater and consequently this would be in accordance with those plotted against hoof and P3 curvature. Thus implying that as the corium volume, dorsal P3 curvature and dorsal hoof wall curvature increases so does the percentage of bundled vessels, this could be explained as a consequence of vasculature remodelling at the microvasculature level. As the abundance of microvessels increase, the pressure exerted from the new vasculature will impact the surrounding tissues consequently causing the vasculature to bundle. This is shown more so in hoofs with both a concave dorsal hoof wall and P3 which is indicative of laminitis (Grosenbaugh and Morgan, 1999; Parks and O'Grady, 2003; Eustace, 2010; Hunt and Wharton, 2010). Perhaps these results could be strengthened if data from equine feet with a positive dorsal hoof wall and negative P3 curvature were included. In the literature there is very little about the morphology and vascular remodelling in laminitics, the main areas of study have been limited to vasoconstriction, vasodilation, perfusion and anastomoses (Peroni *et al.*, 2006; Heymering, 2010).

Total branch length was plotted as a ratio of vasculature volume, as a function of dorsal hoof curvature (Fig 3.19), equine feet with a negative dorsal hoof wall regardless of P3 curvature, displayed an increase in the distribution of data and the vasculature branch length compared to the volume respectively. Indicative that equine feet with a concave dorsal hoof wall and P3, have an increased vasculature volume, particularly with the outcome of total branch length being fairly

uniform/stable. Furthermore vasculature volume was plotted against corium volume, where each data point was colour coded to represent each category (Fig 3.21). The linear regression models presented a very strong correlation and a highly significant deviation from zero, reinforcing that the corium and vasculature volume, increase almost linearly with respect to one another. A greater proportion of equine feet with a concave dorsal hoof wall and P3 had both a greater corium and vasculature volume respectively. Thus suggesting that there are increased numbers of vasculature branches that may anastomose within the concave equine feet, as a result the lumen diameter and branch lengths may not adapt/adjust just to an increase in the vasculature/microvasculature.

Lumen diameter is symptomatic of extreme vasodilation or vasoconstriction, thus toe vessel lumen diameter was recorded and plotted as a function of the primary physical descriptor, hoof curvature and as a function of P3 and hoof wall curvature. On the subject of hoof curvature, toe vessel lumen diameter exhibits no significant correlation (Fig 3.20A), equally the data plotted with respect to both hoof and bone curvatures (Fig 3.20B), accentuates the lack of correlation and variation of toe vessel lumen diameter among the morphologically different equine feet.

The limitations met when analysing the vasculature included the lack of perfused feet with a positive dorsal hoof wall and negative P3 curvature and the resolution of the μ–CT scanner. 120μm was the resolution of the scanner used and consequently the microvasculature was not detectable and could therefore not be analysed for vasculature remodelling.

4.5 Methodology

Throughout the progression of the study some limitations were met. The absence of clinical history or data for each foot made it difficult to

interpret the pathological changes. Whilst the feet were presumed to be ‘normal’ when sourced from the abattoir, the lack of information such as if they were trimmed, shod, barefoot or their clinical history, strongly limited the ability to interpret the findings. Whilst analysis and data could be extracted from these feet, the amount of detail from vasculature and trabecular pore analysis was lacking. The microvasculature could not be seen on the CT scans and therefore could not be assessed for vascular remodelling at this level and consequently limited the vasculature data. In addition to this a smaller number of equine feet were used for vasculature analysis due to poor perfusion. While the aim of this project was to utilise μ-CT, it would have been complementary to have digital photographs in addition. Photographic images could have been used to analyse the external hoof wall features such as the presence of divergent growth rings, divergent horn tubules and coronary band depression (Hunt and Wharton, 2010; Dyson *et al.*, 2011).

As previously stated the dorsal hoof wall curvature was selected as the primary physical descriptor. Within the literature hoof morphology is often an indicator of underlying pathological issues within the equine hoof. In a recent study the external characteristics of the lateral aspect of the hoof were analysed in both non-lame and lame horses. Photographs of 300 horses with foot pain and 25 non-lame horses were investigated. The hoof wall, heel and coronary band angles, hoof wall length, hoof wall height, coronary band length and coronary band height were all analysed. In lame horses the mean hoof wall, heel and coronary band angles were larger. In summary it was hypothesised that hoof shape influences the biomechanical forces acting upon the foots anatomical structures thus having an impact both internally and externally (Dyson *et al.*, 2011). Mathematical studies of the dorsal hoof shape, in particular its curvature lack. However as the external hoof wall shape has been shown to be indicative of underlying abnormalities it further supports the use of dorsal hoof wall curvature as the main physical descriptor.

A literature review on farriery and biomechanics of the equine foot suggests that farriery manipulations, particularly in the sagittal plane can alter the pathophysiological changes seen in many foot ailments. By trimming, applying a wedge or special shoe, the hoof can be manipulated pathomorphologically (Eliashar, 2012). In addition to this the coronary peel and dorsodistal hoof wall fenestration technique has been theorised to treat pathologic changes after acute laminitis. Thus facilitating the restoration of the anatomical components to a normal state, improving the equids prognosis (Eustace, 2010).

4.6 Future Research

The aim of this study was to further enhance the application of μ-CT in an investigation of equine feet and contributing to the field of laminitis research. This novel technique has shown how it can be applied to a broader and more diverse range of analyses. In particular the application in cadaveric equine feet where live tissue analysis may be a future progression in this field of research.

4.6.1 Laboratory μ-CT

4.6.1.1 Volumetric Decomposition of Trabeculae

Research of trabecular anisotropy could be further enhanced to investigate the more explicit segments of trabeculae, plates and rods. Looking at the trabecular microstructure may be more indicative of anisotropy in the distal phalanx. Regions other than the toe tip of P3 should be investigated for anisotropy as a comparison, developing the understanding of the different anatomical regions of P3 and their impact on the surrounding encapsulated structures (Liu *et al.*, 2007). The vectors of anisotropy could also be utilised to identify the directional orientation of the trabeculae, thus would be indicative of the

biomechanical forces exerted on the hoof, giving rise to the source of exertion and the pathomorphological effects.

4.6.1.2 Microvasculature Analysis

With evidence supporting the contribution of vascular pathologies to the pathomorphological effects in chronic laminitics, it is of principal importance to study and assess the microvasculature (Grosenbaugh and Morgan, 1999). Enhanced angiogenic changes and suggestions of remodelling may be more commonly seen at the microvasculature level. With the utilisation of a synchrotron scanner, the microvessels could be detected and analysis could be implemented without a further need for histological experimentation.

4.6.1.2 Dynamic Imaging in Living Tissue

With the use of a synchrotron μ-CT scanner it could allow the experimentation of pathogenic mechanisms involved in hoof deformation and laminitis by providing dynamic imaging in living tissue. The whole foot model could be investigated this way, allowing identification of visible changes in cell size/shape, proliferative rates of epidermal progenitor cells surrounding the coronary dermal papillae, the impact of compressive forces, the effects of inducing laminitis and identifying locations of particular abnormal physical descriptors. The horse limb would need to be artificially maintained in order to encompass normal metabolic activity, concurrently numerous physical and chemical stressors would be applied, analysing their effects and response of the distal limb in real time, thus rendering a model as close to in vivo as possible. A synchrotron scanner at the Diamond Light Source facility can generate images with a voxel resolution just beyond a micron, for micro-imaging and an even smaller voxel resolution for nano-imaging (Diamond Light Source, 2017). The high flux and elevated photon intensity of the synchrotron scanner permits high signal images to be rapidly recorded, hence greater image frequencies

would be achievable in comparison to other x-ray imaging modalities. Consequently this would allow dynamic changes to be frequently monitored. Another advantage of using a synchrotron beamline is the amount of laboratory space it offers. This would render it possible to set up an artificial maintained equine limb, unlike the minimal accessible space of a laboratory μ-CT scanner.

Furthermore the pathogenic pathway of the disease, pathogenic changes as a consequence of chemical triggers and the impact of compressive forces on the equine foot in a partially in vivo model could all be investigated in real-time without the need for live animals. Ethically this would enable intensive studies to be conducted without causing suffering to live animals, as equine bi-product material would be sourced from university-approved abattoirs.

4.6.2 Conformation and Weight Bearing

As aforementioned overloading of the equine limb has been identified as a root cause of laminitis, with this in mind it would not be absurd to suggest investigating and analysing the impact of conformation and weight bearing in equine hoof development/growth. This could be implemented with the visual assessment of equine conformation such as pastern, hoof, knee, metacarpal, forelimb and hindlimb conformation as well as other variables like hoof-pastern angle. These could be both qualitatively and quantitatively assessed with the use of photographic images and measurements, such as angles to assess the degree/presence of conformational faults. Additionally quantitative assessment of equine feet, via the application of a pressure plate, could be effective in measuring the varying pressure load and the locality on increased pressure. Inevitably this would be a non-invasive process and would require minimal contact, thus causing very little distress to the animal in question, whilst providing information on the loading effects and the impact this has on the equine foot.

5 Conclusions

The aim of this study was to develop the understanding of the anatomical components of the equine foot via the utilisation of a novel technique, μ-CT. The imaging modality of choice produced images uncovering the anatomical characteristics of the equine foot and thus any morphological changes/adaptations successfully. Scanning of the feet provided data and enabled analysis of the distal phalanx, vasculature, and corium whilst enabling the 3D reconstruction of the feet in question. Propounding that further investigation, particularly with the use of a higher resolution scanner and samples of both laminitic and normal feet with a known clinical history. The application of a higher resolution scanner such as the synchrotron beamline and the use of dynamic hoof imaging, would compliment these findings. Additionally it would further the understanding of the pathomorphological effects and their origin.

The flushing, pressurising and fixing methodologies implemented were important in the study of blood vessels, particularly as the contrast was so high on the CT slices, enabling differences in branch length, mean lumen thickness, stretch/bundling and vasculature volume to be observed. Conjointly enhancing the need for further research in microvasculature analysis with the use of a higher resolution μ-CT scanner, such as the synchrotron beamline. The imaging and analytical techniques employed in this study could merit the use of this methodology in future research on assessing cell proliferation, microvasculature, chemical triggers/imbalances and the effects of compressive forces on the equine foot in a dynamic artificial living model as well as studying the physical descriptors aforementioned in this study, perhaps in more depth.

With the dorsal hoof wall being a fundamental physical descriptor of the foot's pathological status and thus chronic laminitis, it was used as the sole anatomical variable with which to compare most of the other

measurements. Bone remodelling and morphological status was variable with some observations suggesting that brunt forces are exerted on the parietal surface of P3, especially in concave hoofs. The lack of anisotropic findings in the toe tip region of the distal phalanx warrants the need for further trabecular anisotropy research, analysing the different anatomical regions of P3 and the direction of distortion thus pin-pointing the locality of mechanical strain. Although trabecular bone is less effected by tensile forces than compressive forces. Therefore concurrently, experimentation of compressive forces applied to the distal limb in an artificial living model could be observed and used comparatively. Furthermore the variability in corium volume with respect to P3 curvature is perhaps a consequence of detachment, as result of exceeding the lamellae's elasticity. Suggesting that elevated tensile strain from the lamellae with increasing dorsal hoof concavity, further accentuates that lamellar damage may be an effect, rather that the origin of laminitis. However equine feet with a known laminitic clinical status would need to be assessed alongside clinically normal feet to support this.

Vascular morphology showed minimal variation among the equine feet with respect to dorsal hoof curvature, however in those with a concave dorsal hoof wall and P3 curvature there was a greater incidence of bundled vessels, indicating that vascular remodelling may occur in those showing concave traits. As other blood vessel descriptors showed weak correlation, it would propose that the vascular remodelling takes place at a microvasculature level, beyond the scope of detectability of the laboratory CT scanner. Subsequently an increase in microvasculature may increase the number of arterial/venous shunts hence why vascular branch length remains unchanged but a heightened presence of bundled vessels is observed.

This study has provided an appreciation for the utilisation of μ-CT and the interdisciplinary of Biology and Physics in the investigation of equine hoof anatomy, and on a larger scale, the field of Veterinary

Science. The observations made in this study highlight the importance of conformation, bone morphology, blood vessels, hoof wall shape and other soft tissue structures encapsulated in the equine hoof and their effects in correspondence with one another. Further investigation is required in trabecular bone distortion, microvasculature network, cell proliferation, conformation and weight bearing of the equine hoof capsule. For that reason other studies on hoof deformation, growth, conformation, weight bearing and development in conditions such as laminitis, would benefit from the use of the imaging modality used in this study. Moreover the use of a beamline CT scanner, such as the synchrotron beamline, would augment a greater insight into the microstructures and increase the detectability of morphological and pathological adaptations.

References

Ackerman, N., Garner, H. E., Coffman, J. R. and Clement, J. W. (1975) 'Angiographic appearance of the normal equine foot and alterations in chronic laminitis.', *Journal of the American Veterinary Medical Association*, 166(1), pp. 58–62. Available at: http://www.ncbi.nlm.nih.gov/pubmed/1110201 (Accessed: 18 December 2017).

Allen, M. R., Hock, J. M. and Burr, D. B. (2004) 'Periosteum: biology, regulation, and response to osteoporosis therapies', 35, pp. 1003–1012. doi: 10.1016/j.bone.2004.07.014.

Arnett, T. (2003) 'Regulation of bone cell function by acid-base balance', *Proceedings of the Nutrition Society*. Elsevier, 62(2), pp. 511–520. doi: 10.1002/jbmr.5650060508.

Arnett, T. R. (2010) 'Acidosis, hypoxia and bone', *Archives of Biochemistry and Biophysics*, 503, pp. 103–109. doi: 10.1016/j.abb.2010.07.021.

Ascenzi, M.-G., Gill, J. and Lomovtsev, A. (2008) 'Orientation of collagen at the osteocyte lacunae in human secondary osteons', *Journal of Biomechanics*, 41(16), pp. 3426–3435. doi: 10.1016/j.jbiomech.2008.09.010.

Atkins, G. J. and Findlay, D. M. (2012) 'Osteocyte regulation of bone mineral: a little give and take', *Osteoporosis International*. Springer-Verlag, 23(8), pp. 2067–2079. doi: 10.1007/s00198-012-1915-z.

Baldwin, G. I. (2010) 'Progression of Venographic Changes After Experimentally Induced Laminitis', *Veterinary Clinics of North America: Equine Practice*, 26(1), pp. 135–140. doi: 10.1016/j.cveq.2009.12.005.

Barker, Z. E., Leach, K. A., Whay, H. R., Bell, N. J. and Main, D. C. J. (2010) 'Assessment of lameness prevalence and associated risk factors in dairy herds in England and Wales', *Journal of Dairy Science*, 93(3), pp. 932–941. doi: 10.3168/jds.2009-2309.

Baxter, G. M. (2011) *Manual of equine lameness*. Wiley-Blackwell.

Bayliss, L., Mahoney, D. J. and Monk, P. (2012) 'Normal bone physiology, remodelling and its hormonal regulation', *Surgery (Oxford)*, 30(2), pp. 47–53. doi: 10.1016/j.mpsur.2011.12.009.

Bell, N. (2015) 'Lameness Control in Dairy Herds Part 1 -Practical Foot Trimming (Dutch 5 Step Method)'.

Bentley, V. A., Sample, S. J., Livesey, M. A., Scollay, M. C., Radtke, C. L., Frank, J. D., Kalscheur, V. L. and Muir, P. (2007) 'Morphologic changes associated with functional adaptation of the navicular bone of horses', *Journal of Anatomy*. Blackwell Publishing Ltd, 211(5), pp. 662–672. doi: 10.1111/j.1469-7580.2007.00800.x.

Bonewald, L. F. (2007) 'Osteocytes as dynamic multifunctional cells.', *Annals of the New York Academy of Sciences*, 1116, pp. 281–90. doi: 10.1196/annals.1402.018.

Bowker, R. M. (2003) 'Contrasting Structural Morphologies of "Good" and "Bad" Footed Horses', in *AAEP Proceedings*, pp. 186–209.

Bragulla, H., Ernsberger, S. and Budras, K.-D. (2001) 'On the Development of the Papillary Body in the Feline Claw', *Anatomia, Histologia, Embryologia: Journal of Veterinary Medicine Series C*. Blackwell Science Ltd., 30(4), pp. 211–217. doi: 10.1046/j.1439-0264.2001.00319.x.

Bragulla, H. H. and Homberger, D. G. (2009) 'Structure and functions of keratin proteins in simple, stratified, keratinized and cornified epithelia', *Journal of Anatomy*. Blackwell Publishing Ltd, 214(4), pp. 516–559. doi: 10.1111/j.1469-7580.2009.01066.x.

Budras, K., Sack, W. O., Rck, S. and Horowitz, A. (2009) 'Anatomy of the

horse, Fifth, revised edition'. Manson Publishing.
Canalis, E., McCarthy, T. L. and Centrella, M. (1991) 'Growth Factors and Cytokines in Bone Cell Metabolism', *Annual Review of Medicine*. Annual Reviews 4139 El Camino Way, P.O. Box 10139, Palo Alto, CA 94303-0139, USA, 42(1), pp. 17–24. doi: 10.1146/annurev.me.42.020191.000313.
Carlsson, C. A. (1999) 'Imaging modalities in x-ray computerized tomography and in selected volume tomography', *Physics in Medicine and Biology*. IOP Publishing, 44(3), pp. R23–R56. doi: 10.1088/0031-9155/44/3/011.
Carter, R. A., Engiles, J. B., Megee, S. O., Senoo, M. and Galantino-Homer, H. L. (2011) 'Decreased expression of p63, a regulator of epidermal stem cells, in the chronic laminitic equine hoof', *Equine Veterinary Journal*. Blackwell Publishing Ltd, 43(5), pp. 543–551. doi: 10.1111/j.2042-3306.2010.00325.x.
Chen, J.-H., Liu, C., You, L. and Simmons, C. A. (2010) 'Boning up on Wolff's Law: Mechanical regulation of the cells that make and maintain bone', *Journal of Biomechanics*, 43(1), pp. 108–118. doi: 10.1016/j.jbiomech.2009.09.016.
Clarke, B. (2008) 'Normal bone anatomy and physiology.', *Clinical journal of the American Society of Nephrology : CJASN*. American Society of Nephrology, 3 Suppl 3(Suppl 3), pp. S131-9. doi: 10.2215/CJN.04151206.
Colville, T. P. and Bassert, J. M. (2009) *Clinical anatomy and physiology laboratory manual for veterinary technicians*. Mosby Elsevier.
Daradka, M. and Pollitt, C. C. (2004) 'Epidermal cell proliferation in the equine hoof wall', *Equine Veterinary Journal*, 36(3), pp. 236–241. doi: 10.2746/0425164044877198.
Denoix, J.-M. (1999) 'Functional Anatomy of the Equine Interphalangeal Joints', in *Annual Convention of the AAEP*, pp. 174–177.
Diamond Light Source (2017) *Diamond Manchester Imaging Branchline (I13-2) - Materials - Diamond Light Source*. Available at: http://www.diamond.ac.uk/Beamlines/Materials/I13/Diamond-Manchester_Imaging_Branchline.html (Accessed: 19 May 2017).
Doube, Mi., Kłosowski, Mi. M., Arganda-Carreras, I., Cordelières, F. P., Dougherty, R. P., Jackson, J. S., Schmid, B., Hutchinson, J. R. and Shefelbine, S. J. (2010) 'BoneJ: Free and extensible bone image analysis in ImageJ.', *Bone*. Europe PMC Funders, 47(6), pp. 1076–9. doi: 10.1016/j.bone.2010.08.023.
Douglas, J. E., Mittal, C., Thomason, J. J. and Jofriet, J. C. (1996) 'The modulus of elasticity of equine hoof wall: implications for the mechanical function of the hoof.', *Journal of Experimental Biology*, 199(8).
Drangova, M., Holdsworth, D. W., Boyd, C. J., Dunmore, P. J., Roach, M. R. and Fenster, A. (1993) 'Elasticity and geometry measurements of vascular specimens using a high-resolution laboratory CT scanner.', *Physiological measurement*, 14(3), pp. 277–90.
Dyce, K. M. (Keith M. ., Sack, W. O. (Wolfgang O. . and Wensing, C. J. G. (Cornelis J. G. (2010) *Textbook of veterinary anatomy*. Saunders/Elsevier.
Dyson, S. J., Tranquille, C. A., Collins, S. N., Parkin, T. D. H. and Murray, R. C. (2011) 'External characteristics of the lateral aspect of the hoof differ between non-lame and lame horses.', *Veterinary journal (London, England : 1997)*, 190(3), pp. 364–71. doi: 10.1016/j.tvjl.2010.11.015.
Dyson, S. and Nagy, A. (2011) 'Injuries associated with the cartilages of the foot', *Equine Veterinary Education*, 23(11), pp. 581–593. doi: 10.1111/j.2042-3292.2011.00260.x.
Eliashar, E. (2012) 'The Biomechanics of the Equine Foot as it Pertains to Farriery', *Veterinary Clinics of North America: Equine Practice*. Elsevier, 28(2), pp. 283–291. doi: 10.1016/J.CVEQ.2012.06.001.
Engiles, J. B., Galantino-Homer, H. L., Boston, R., McDonald, D., Dishowitz,

M. and Hankenson, K. D. (2015) 'Osteopathology in the Equine Distal Phalanx Associated With the Development and Progression of Laminitis', *Veterinary Pathology*. SAGE PublicationsSage CA: Los Angeles, CA, 52(5), pp. 928–944. doi: 10.1177/0300985815588604.
Eustace, R. A. (2010) 'Clinical Presentation, Diagnosis, and Prognosis of Chronic Laminitis in Europe', *Veterinary Clinics of North America: Equine Practice*, 26(2), pp. 391–405. doi: 10.1016/j.cveq.2010.06.005.
Fan, T. D., Jagger, R. and Bicknell, R. (1995) 'Controlling the vasculature: Angiogenesis, anti-angiogenesis and vascular targeting of gene therapy', *Trends in Pharmacological Sciences*, 16(2), pp. 57–66. doi: 10.1016/S0165-6147(00)88979-8.
Feng, X. and McDonald, J. M. (2011) 'Disorders of bone remodeling.', *Annual review of pathology*. NIH Public Access, 6, pp. 121–45. doi: 10.1146/annurev-pathol-011110-130203.
Floyd, A. and Mansmann, R. (2007) *Equine Podiatry*. Elsevier Health Sciences.
Folkman, J. and Shing, Y. (1992) 'Angiogenesis', *THE JOURNAL OF BIOLOGICAL CHEMISTRY*, 267(16), pp. 10931–10934.
Goulet, C., Olive, J., Rossier, Y. and Beauchamp, G. (2015) 'RADIOGRAPHIC AND ANATOMIC CHARACTERISTICS OF DORSAL HOOF WALL LAYERS IN NONIAMINITIC HORSES', *Veterinary Radiology & Ultrasound*, 56(6), pp. 589–594. doi: 10.1111/vru.12280.
Green, J. and Kleeman, C. R. (1991) 'Role of bone in regulation of systemic acid-base balance', *Kidney International*, 39(1), pp. 9–26. doi: 10.1038/ki.1991.2.
Grosenbaugh, D. A. and Morgan, S. J. (1999) 'The Digital Pathologies of Chronic Laminitis', *Veterinary Clinics of North America: Equine Practice*, 15(2), pp. 419–436. doi: 10.1016/S0749-0739(17)30153-0.
Hadjidakis, D. J. and Androulakis, I. I. (2006) 'Bone Remodeling', *Annals of the New York Academy of Sciences*. Blackwell Publishing Inc, 1092(1), pp. 385–396. doi: 10.1196/annals.1365.035.
Heymering, H. W. (2010) '80 Causes, Predispositions, and Pathways of Laminitis', *Veterinary Clinics of North America: Equine Practice*, 26(1), pp. 13–19. doi: 10.1016/j.cveq.2009.12.003.
Hinchcliff, K. W. (Kenneth W., Kaneps, A. J. and Geor, R. J. (2008) *Equine exercise physiology : the science of exercise in the athletic horse*. Saunders/Elsevier.
Hood, D. M. (1999) 'Laminitis in the Horse', *Veterinary Clinics of North America: Equine Practice*, 15(2), pp. 287–294. doi: 10.1016/S0749-0739(17)30145-1.
Hunt, R. and Wharton, R. E. (2010) 'Clinical Presentation, Diagnosis, and Prognosis of Chronic Laminitis in North America', *Veterinary Clinics of North America: Equine Practice*, 26(1), pp. 141–153. doi: 10.1016/j.cveq.2009.12.006.
Ireland, J. L., Clegg, P. D., McGowan, C. M., Platt, L. and Pinchbeck, G. L. (2011) 'Factors associated with mortality of geriatric horses in the United Kingdom', *Preventive Veterinary Medicine*. Elsevier, 101(3–4), pp. 204–218. doi: 10.1016/J.PREVETMED.2011.06.002.
Keaveny, T. M., Watchel, E. F., Ford, C. M. and Hayes, W. C. (1994) 'Differences between the tensile and compressive strengths of bovine tibial trabecular bone depend on modulus', *Journal of Biomechanics*, 27(9), pp. 1137–1146. doi: 10.1016/0021-9290(94)90054-X.
Ketcham, R. A. and Ryan, T. M. (2004) 'Quantification and visualization of anisotropy in trabecular bone', *Journal of Microscopy*. Blackwell Science Ltd, 213(2), pp. 158–171. doi: 10.1111/j.1365-2818.2004.01277.x.

Kim, J.-N., Lee, J.-Y., Shin, K.-J., Gil, Y.-C., Koh, K.-S. and Song, W.-C. (2015) 'Haversian system of compact bone and comparison between endosteal and periosteal sides using three-dimensional reconstruction in rat.', *Anatomy & cell biology*. Korean Association of Anatomists, 48(4), pp. 258–61. doi: 10.5115/acb.2015.48.4.258.
Kinahan, P. E., Hasegawa, B. H. and Thomas, B. (2003) 'X-ray-based attenuation correction for positron emission tomography/computed tomography scanners', *Seminars in Nuclear Medicine*, 33(3), pp. 166–179. doi: 10.1053/snuc.2003.127307.
Kobayashi, Y., Miyamoto, M., Sugibayashi, K. and Morimoto, Y. (1999) 'Drug Permeation through the Three Layers of the Human Nail Plate', *Journal of Pharmacy and Pharmacology*. Blackwell Publishing Ltd, 51(3), pp. 271–278. doi: 10.1211/0022357991772448.
Kochová, P., Witter, K., Cimrman, R., Mezerová, J. and Tonar, Z. (2013) 'A preliminary study into the correlation of stiffness of the laminar junction of the equine hoof with the length density of its secondary lamellae', *Equine Veterinary Journal*. Blackwell Publishing Ltd, 45(2), pp. 170–175. doi: 10.1111/j.2042-3306.2012.00632.x.
Komosa, M. (2013) 'ChangessinnNaviculaRrBonee(osssesamoideummdistale))ShapeeinnHorses assaaResulttoffPathologicallAlterations', *Folia Biologica (Kraków)*, 61, pp. 1–2. doi: 10.3409/fb61_1-2.01.
König, H. E., Liebich, H.-G. and Bragulla, H. (Hermann). (2007) *Veterinary anatomy of domestic mammals : textbook and colour atlas*. Schattauer.
Korf-Klingebiel, M., Kempf, T., Sauer, T., Brinkmann, E., Fischer, P., Meyer, G. P., Ganser, A., Drexler, H. and Wollert, K. C. (2008) 'Bone marrow cells are a rich source of growth factors and cytokines: implications for cell therapy trials after myocardial infarction', *European Heart Journal*. Oxford University Press, 29(23), pp. 2851–2858. doi: 10.1093/eurheartj/ehn456.
Kraus, S. (2014) *Hoof Cracks Need Immediate Attention | Horse Journal*, *Horse Journal*. Available at: http://horse-journal.com/article/hoof-cracks-attention-11014 (Accessed: 28 April 2016).
Kurbel, S., Radić, R., Kotromanović, Ž., Pušeljić, Ž. and Kratofil, B. (2003) 'A calcium homeostasis model: orchestration of fast acting PTH and calcitonin with slow calcitriol', *Medical Hypotheses*, 61(3), pp. 346–350. doi: 10.1016/S0306-9877(03)00107-5.
Landers, T. A. (2006) *Professional Care of the Racehorse: A Guide to Grooming, Feeding, and Handling the Equine Athlete*. Eclipse Press.
Lawlor, K. T. and Kaur, P. (2015) 'Dermal Contributions to Human Interfollicular Epidermal Architecture and Self-Renewal.', *International journal of molecular sciences*. Multidisciplinary Digital Publishing Institute (MDPI), 16(12), pp. 28098–107. doi: 10.3390/ijms161226078.
Lawson, S. E. M., Chateau, H., Denoix, J.-M. and Crevier-Denoix, N. (2006) 'Equine digital collateral ligaments', *Journal of Biomechanics*. Elsevier, 39, p. S498. doi: 10.1016/S0021-9290(06)85040-2.
Liao, X., Lu, S., Zhuo, Y., Winter, C., Xu, W., Li, B. and Wang, Y. (2011) 'Bone Physiology, Biomaterial and the Effect of Mechanical/Physical Microenvironment on Mesenchymal Stem Cell Osteogenesis', *Cellular and Molecular Bioengineering*, 4(4), pp. 579–590. doi: 10.1007/s12195-011-0204-9.
Lieben, L. and Caemeliet, G. (2013) 'Vitamin D signaling in osteocytes: Effects on bone and mineral homeostasis', *Bone*, 54(2), pp. 237–243. doi: 10.1016/j.bone.2012.10.007.
Liu, X. S., Sajda, P., Saha, P. K., Wehrli, F. W., Bevill, G., Keaveny, T. M. and Guo, X. E. (2007) 'Complete Volumetric Decomposition of Individual

Trabecular Plates and Rods and Its Morphological Correlations With Anisotropic Elastic Moduli in Human Trabecular Bone', *Journal of Bone and Mineral Research*. John Wiley and Sons and The American Society for Bone and Mineral Research (ASBMR), 23(2), pp. 223–235. doi: 10.1359/jbmr.071009.
Marenzana, M. and Arnett, T. R. (2013) 'The Key Role of the Blood Supply to Bone', *Bone Research*. Nature Publishing Group, 1(3), pp. 203–215. doi: 10.4248/BR201303001.
McClure, R. C. (Robert C. (1993) 'Functional Anatomy of the Horse Foot'. University of Missouri Extension.
Mckittrick, J., Chen, P.-Y., Bodde, S. G., Yang, W., Novitskaya, E. E. and Meyers, M. A. (2012) 'The Structure, Functions, and Mechanical Properties of Keratin', *JOM*. Springer US, 64(4), pp. 449–468. doi: 10.1007/s11837-012-0302-8.
Menzies-Gow, N. (2006) 'Equine acute pasture-associated laminitis Part I', *Companion Animal*, 11(4), pp. 10–12. doi: 10.1111/j.2044-3862.2006.tb00042.x.
Menzies-Gow, N. J., Stevens, K., Barr, A., Camm, I., Pfeiffer, D. and Marr, C. M. (2010) 'Severity and outcome of equine pasture-associated laminitis managed in first opinion practice in the UK', *Veterinary Record*, 167(10), p. 364 LP-369.
Mercuri, E. G. F., Daniel, A. L., Hecke, M. B. and Carvalho, L. (2016) 'Influence of different mechanical stimuli in a multi-scale mechanobiological isotropic model for bone remodelling', *Medical Engineering & Physics*, 38(9), pp. 904–910. doi: 10.1016/j.medengphy.2016.04.018.
Mishra, P. C. and Leach, D. H. (1983) 'Extrinsic and intrinsic veins of the equine hoof wall.', *Journal of anatomy*. Wiley-Blackwell, 136(Pt 3), pp. 543–60.
Mizutani, R. and Suzuki, Y. (2012) 'X-ray microtomography in biology', *Micron*, 43(2), pp. 104–115. doi: 10.1016/j.micron.2011.10.002.
Morris, A. (2015) 'The Effects of Three Shoeing Methods on Hoof Growth and Health in Horses'.
Morrison, S. (2010) 'Chronic Laminitis: Foot Management', *Veterinary Clinics of North America: Equine Practice*, 26(2), pp. 425–446. doi: 10.1016/j.cveq.2010.06.003.
Mueller, R. S. (1999) 'Diagnosis and management of canine claw diseases', *Veterinary Clinics of North America: Small Animal Practice*, 29, pp. 1357–1371. doi: 10.1016/S0195-5616(99)50132-0.
Nakahama, K. (2010) 'Cellular communications in bone homeostasis and repair', *Cell and Molecular Life Sciences*, 67, pp. 4001–4009. doi: 10.1007/s00018-010-0479-3.
Nakamura, I., Takahashi, N., Jimi, E., Udagawa, N. and Suda, T. (2012) 'Regulation of osteoclast function.', *Modern rheumatology / the Japan Rheumatism Association*, 22(2), pp. 167–77. doi: 10.1007/s10165-011-0530-8.
Neues, F., Goerlich, R., Renn, J., Beckmann, F. and Epple, M. (2007) 'Skeletal deformations in medaka (Oryzias latipes) visualized by synchrotron radiation micro-computer tomography (SRμCT)', *Journal of Structural Biology*, 160(2), pp. 236–240. doi: 10.1016/j.jsb.2007.08.010.
Nyary, T. and Scammell, B. E. (2015) 'Principles of bone and joint injuries and their healing', *Surgery*, 33, pp. 7–14. doi: 10.1016/j.mpsur.2014.10.011.
O'Grady, S. E. (2010) 'Farriery for Chronic Laminitis', *Veterinary Clinics of North America: Equine Practice*, 26(2), pp. 407–423. doi: 10.1016/j.cveq.2010.04.008.
O'Grady, S. E. (2013) *Equine Podiatry | Dr. Stephen O'Grady, veterinarians,*

farriers, books, articles, *AAEP Convention Proceedings*. Available at: http://www.equipodiatry.com/podiatry.html (Accessed: 27 April 2016).
Parks, A. (2003) 'Form and function of the equine digit', *Veterinary Clinics of North America: Equine Practice*, 19(2), pp. 285–307. doi: 10.1016/S0749-0739(03)00018-X.
Parks, A. and O'Grady, S. E. (2003) 'Chronic laminitis: current treatment strategies', *Veterinary Clinics of North America: Equine Practice*, 19(2), pp. 393–416. doi: 10.1016/S0749-0739(03)00019-1.
Paul, E. K. (2016) 'The utilisation of μ-computed tomography for the investigation of equine papilla/lamella-associated foot lameness'.
Peacock, M. (2010) 'Calcium Metabolism in Health and Disease', *Clinical Journal of the American Society of Nephrology*. American Society of Nephrology, 5(Supplement 1), pp. S23–S30. doi: 10.2215/CJN.05910809.
Pearson, O. M. and Lieberman, D. E. (2004) 'The aging of Wolff's "law": Ontogeny and responses to mechanical loading in cortical bone', *American Journal of Physical Anthropology*, 125(S39), pp. 63–99. doi: 10.1002/ajpa.20155.
Peroni, J. F., Moore, J. N., Noschka, E., Grafton, M. E., Aceves-Avila, M., Lewis, S. J. and Robertson, T. P. (2006) 'Predisposition for venoconstriction in the equine laminar dermis: implications in equine laminitis', *Journal of Applied Physiology*, 100(3).
Pleasant, R. S. and McKinlay, I. (2012) 'Farriery for Hoof Wall Defects: Quarter Cracks and Toe Cracks', *Veterinary Clinics of North America: Equine Practice*, 28(2), pp. 393–406. doi: 10.1016/j.cveq.2012.06.005.
Pollitt, C. C. (1994) 'The basement membrane at the equine hoof dermal epidermal junction', *Equine Veterinary Journal*, 26(5), pp. 399–407. doi: 10.1111/j.2042-3306.1994.tb04410.x.
Pollitt, C. C. (1998) 'The anatomy and physiology of the hoof wall', *Equine Veterinary Education*. Blackwell Publishing Ltd, 10(6), pp. 318–325. doi: 10.1111/j.2042-3292.1998.tb00902.x.
Pollitt, C. C. (1999) 'Equine Laminitis: A Revised Pathophysiology', in *AAEP Convention Proceedings*, pp. 188–192.
Pollitt, C. C. (2004a) 'Anatomy and physiology of the inner hoof wall', *Clinical Techniques in Equine Practice*, 3(1), pp. 3–21. doi: 10.1053/j.ctep.2004.07.001.
Pollitt, C. C. (2004b) 'Equine laminitis', *Clinical Techniques in Equine Practice*, 3(1), pp. 34–44. doi: 10.1053/j.ctep.2004.07.003.
Pollitt, C. C. (2010) 'The Anatomy and Physiology of the Suspensory Apparatus of the Distal Phalanx', *Veterinary Clinics of North America: Equine Practice*, 26(1), pp. 29–49. doi: 10.1016/j.cveq.2010.01.005.
Porter, R. S. and Kaplan, J. L. (2013) *The merck manual go-to home guide for symptoms*. Simon and Schuster.
Puchalski, S. M. (2012) 'Advances in Equine Computed Tomography and Use of Contrast Media', *Veterinary Clinics of North America: Equine Practice*, 28(3), pp. 563–581. doi: 10.1016/j.cveq.2012.08.002.
Ranjbar, S., Rabiee, A. R., Gunn, A. and House, J. K. (2016) 'Identifying risk factors associated with lameness in pasture-based dairy herds', *Journal of Dairy Science*, 99(9), pp. 7495–7505. doi: 10.3168/jds.2016-11142.
Rasband, W. (2003) *Grid Overlay Macro*, *National Institutes of Health*. Available at: https://imagej.nih.gov/ij/macros/examples/Grid_Overlay.txt (Accessed: 17 August 2016).
Rauch, C. and Cherkaoui-Rbati, M. (2014) 'Physics of nail conditions: why do ingrown nails always happen in the big toes?', *Physical Biology*. IOP Publishing, 11(6), p. 66004. doi: 10.1088/1478-3975/11/6/066004.
Rosenburg, N., Rosenburg, O. and Soudry, M. (2012) 'Rambam Maimonides

Medical Journal Osteoblasts in Bone Physiology—Mini Review', *RMMJ*, 3(2), pp. 13–0. doi: 10.5041/RMMJ.10080.
Rucker, A. (2010a) 'Clinical Applications of Digital Venography', *Journal of Equine Veterinary Science*, 30(9), pp. 491–503. doi: 10.1016/j.jevs.2010.07.016.
Rucker, A. (2010b) 'Equine Venography and Its Clinical Application in North America', *Veterinary Clinics of North America: Equine Practice*, 26(1), pp. 167–177. doi: 10.1016/j.cveq.2009.12.008.
Schramme, M. C. (2011) 'Deep digital flexor tendonopathy in the foot', *Equine Veterinary Education*, 23(8), pp. 403–415. doi: 10.1111/j.2042-3292.2011.00235.x.
Slater, J. (2016) *The Blue Cross*, *National Equine Health Survey (NEHS)*.
Smith, E. M., Gilbert, A., Russell, C. L., PURDY, K. J., MEDLEY, G. F., MUZAFAR, M., Grogono-THOMAS, R. and GREEN, L. E. (2017) 'Within-Flock Population Dynamics of Dichelobacter nodosus.', *Frontiers in veterinary science*. Frontiers Media SA, 4, p. 58. doi: 10.3389/fvets.2017.00058.
Spurgeon, T. L., Kainer, R. A. and McCracken, T. O. (2013) *Spurgeon's Color Atlas of Large Animal Anatomy*. 1st edn. Wiley.
Stapor, P., Wang, X., Goveia, J., Moens, S. and Carmeliet, P. (2014) 'Angiogenesis revisited – role and therapeutic potential of targeting endothelial metabolism', *Journal of Cell Science*, 127(20).
Stashak, T. S. (2013) *Practical Guide to Lameness in Horses*. 4th edn. Wiley.
Steiner, C. C. and Ryder, O. A. (2011) 'Molecular phylogeny and evolution of the Perissodactyla', *Zoological Journal of the Linnean Society*, 163(4), pp. 1289–1303. doi: 10.1111/j.1096-3642.2011.00752.x.
Stocum, D. L. (2012) *Regenerative biology and medicine*. Elsevier/Academic Press.
Taylor, P. C. (2008) 'The angiogenic drive in chronic inflammation: Hypoxia and the cytokine milieu', in *Angiogenesis in Inflammation: Mechanisms and Clinical Correlates*. Basel: Birkhäuser Basel, pp. 15–28. doi: 10.1007/978-3-7643-7650-5_2.
Tsubota, K. and Adachi, T. (2005) 'Spatial and temporal regulation of cancellous bone structure: characterization of a rate equation of trabecular surface remodeling', *Medical Engineering & Physics*, 27(4), pp. 305–311. doi: 10.1016/j.medengphy.2004.09.013.
Waguespack, R. W. and Hanson, D. R. R. (2010) 'Navicular Syndrome in Equine Patients: Anatomy, Causes, and Diagnosis*'.
Walsh, J. S. (2015) 'Normal bone physiology, remodelling and its hormonal regulation', *Surgery*, 33(1), pp. 1–6. doi: 10.1016/j.mpsur.2014.10.010.
Warren, S. (2013) 'Claw disease in dogs: Part 1 – anatomy and diagnostic approach', *Companion Animal*. Blackwell Publishing Ltd, 18(4), pp. 165–170. doi: 10.12968/coan.2013.18.4.165.
Winter, A. C. (2008) 'Lameness in sheep', *Small Ruminant Research*, 76(1), pp. 149–153. doi: 10.1016/j.smallrumres.2007.12.008.
Wyant, A. R., Capasso, P. and Wolbarst, A. B. (2013) *Medical Imaging: Esentials for Physicians*. 1st edn. Wiley.
Zuo, Y., Xiao, W., Chen, X., Tang, Y., Luo, H. and Fan, H. (2012) 'Bottom-up approach to build osteon-like structure by cell-laden photocrosslinkable hydrogelw', *Chem. Commun. Chem. Commun*, 48(48), pp. 3170–3172. doi: 10.1039/c2cc16744a.